

University of Central Florida

STARS

Electronic Theses and Dissertations

2014

Optical and Magnetic properties of nanostructures

Neha Nayyar

University of Central Florida



Part of the [Physics Commons](#)

Find similar works at: <https://stars.library.ucf.edu/etd>

University of Central Florida Libraries <http://library.ucf.edu>

This Doctoral Dissertation (Open Access) is brought to you for free and open access by STARS. It has been accepted for inclusion in Electronic Theses and Dissertations by an authorized administrator of STARS. For more information, please contact STARS@ucf.edu.

STARS Citation

Nayyar, Neha, "Optical and Magnetic properties of nanostructures" (2014). *Electronic Theses and Dissertations*. 4794.

<https://stars.library.ucf.edu/etd/4794>

OPTICAL AND MAGNETIC PROPERTIES OF NANOSTRUCTURES

by

NEHA NAYYAR

B.Sc. University of Delhi, 2006

M.Sc. University of Delhi, 2008

A dissertation submitted in partial fulfillment of the requirements
for the degree of Doctor of Philosophy
in the Department of Physics
in the College of Science
at the University of Central Florida
Orlando, Florida

Spring Term
2014

Major Professor: Talat S. Rahman

© 2014 Neha Nayyar

ABSTRACT

In this thesis, Density Functional Theory and Time-Dependent Density-Functional Theory approaches are applied to study the optical and magnetic properties of several types of nanostructures. In studies of the optical properties we mainly focused on the plasmonic and excitonic effects in pure and transition metal-doped noble metal nanochains and their conglomerates. In the case of pure noble metal chains, it was found that the (collective) plasmon mode is pronounceable when the number of atoms in the chain is larger than 5. The plasmon energy decreases with further with increasing number of atoms (N) and is almost N -independent when N is larger than 20. In the case of coupled pure chains it was found that the plasmon energy grows as square root of the number of chains, and reaches the visible light energy 1.8eV for the case of three parallel chains. Doping of pure Au chains with transition-metal atoms leads in many cases to formation of additional plasmon peaks close in energy to the undoped chain peak. This peak comes from the local charge oscillations around the potential minima created by the impurity atom. The effect is especially pronounced for Ni-doped chains. In the multiple-chain case, we find an unusual hybridization of the two different (local and collective) plasmon modes. Changing the chain size and chemical composition in the array can be used to tune the absorption properties of nanochains. The case of coupled finite (plasmonic) and infinite (semiconductor, excitonic) chains was also analyzed. We find that one can get significant exciton-plasmon coupling, including hybridized modes and energy transfer between these excitations, in the case of doped

chains. The impurity atoms are found to work as attraction centers for excitons. This can be used to transform the exciton energy into local plasmon oscillations with consequent emission at desired point (at which the impurity is located). In a related study the optical properties of single layer MoS₂ was analyzed with a focus on the possibility of ultrafast emission, In particular, it was found that the system can emit in femto-second regime under ultrafast laser pulse excitations. Finally, we have studied the magnetic properties of FeRh nanostructures to probe whether there is an antiferromagnetic to ferromagnetic transition as a function of the ratio of Fe and Rh atoms, as in the bulk alloy.. Surprisingly, the ferromagnetic phase is found to be much more stable for these nanostructures as compared to the bulk, which suggests that band-type effects may be responsible for this transition in the bulk, i.e. the transition cannot be described in terms of modification of the Heisenberg model parameters.

ACKNOWLEDGMENTS

First and Foremost I would like to thank my advisor Dr. Talat Rahman, without her support and guidance this work would not have been possible. I appreciate all her contributions personal and professional which have helped me to work better during my Ph.D. Her scientific advice and knowledge, and her critical approaches to the problems always helped me to learn and perform better.

I am most grateful to the members of my committee, Dr. Sergei Stolbov, Dr. Florencio Eloy Hernández and Dr. Masahiro Ishigami for their time, and expertise throughout this study.

I am very grateful to Dr. Volodymyr Turkowski for his support in all the projects I have worked on, for his generosity, helpful scientific discussions and efforts to make things simple and transparent for me to understand in several projects during my PhD study. I would also like to thank Dr. Duy Le who has always patiently answered all my queries and helped learning many computational techniques. Thanks to all the group members, students and post-docs, A. Kabir, T. Rawal, G. Shafai Erfani, Dr. M. Aminpour, Dr. S. I. Shah, Z. Hooshmand, S. Acharya, Dr. M. A. Ortigoza, Dr. S. Hong, Dr. A. Ramirez for their support and fruitful discussions

I sincerely want to thank Dr. Lyman Baker for his invaluable comments and discussions on all my publications and projects.

Lastly, I would like to thank my family for all their immense love and support. My deepest gratitude is for my parents, who have always given me immense strength and encouragement in every phase of life. I would also like to thank my new family who have welcomed me and loved me like their daughter. It's their love and sacrifices that made it possible to finish what I had started.

And most of all, for my loving, supportive, encouraging, and patient husband Dr. Lalit Shokeen without whose support nothing would have ever been possible and my precious little angel Netanya who was born during my PhD. It is her unconditional love and hope in her eyes that have always kept me going through even the toughest times.

TABLE OF CONTENTS

LIST OF FIGURES.....	x
LIST OF TABLES.....	xvi
CHAPTER 1 INTRODUCTION.....	1
CHAPTER 2 THEORETICAL METHODS	7
2.1 Density Functional Theory	7
2.1.1 Exchange-Correlation Functional	13
2.1.2 Spin-Density Functional Theory	18
2.1.3 DFT+U	19
2.2 Combined DFT and Many-Body Approaches	22
2.2.1 Green's Function and GW Approximation	22
2.2.2 DFT+DMFT	23
2.3 Time-Dependent Density-Functional Theory	26
2.3.1 Adiabatic Approximation.....	29
2.3.2 Linear Response Theory	30
2.3.3 Casida Equations	36
CHAPTER 3 OPTICAL PROPERTIES OF NANOCHAINS	39

3.1 Plasmonic Effects	39
3.1.1 Plasmons	39
3.1.2 Single pure and doped Au chains	43
3.1.3 Multiple Chains.....	67
3.2 Effects of Exciton Plasmon Interaction in Coupled Chains	87
3.2.1 Excitons.....	87
3.2.2 Exciton Plasmon Energy Transfer.....	93
CHAPTER 4 ULTRAFAST EMISSION IN SINGLE LAYER MoS ₂	103
4.1 Computational Details.....	105
4.2 Results.....	108
4.3 Conclusions	120
CHAPTER 5 MAGNETIC PROPERTIES OF NANOPARTICLES	121
5.1 AFM-FM Transition in Bulk Fe-Rh	121
5.2 Magnetism in FeRh Nanoparticles.....	123
5.2.1 Computational Details	124
5.2.2 Results	125
5.2.3 Conclusions.....	134
CHAPTER 6 SUMMARY	136

APPENDIX: ORBITAL DENSITY IN DOUBLE CHAINS.....	137
REFERENCES.....	146

LIST OF FIGURES

Figure 1. Electron gas model to describe the charge oscillation.	39
Figure 2. Schematic representation of plasmons in chains.	42
Figure 3 The optical absorption spectrum of the Au_n ($n=4-24$) from bottom to top.	46
Figure 4 The optical absorption spectrum for $Au_{n-1}Ni$ ($n=8-24$). The local plasmon peak emerges at the left of the main peak at $n=12$ and changes its relative position at $n>20$	47
Figure 5 The optical absorption spectrum of Au_{20} , Au_{19} , $Au_{19}Ni$, $Au_{19}Rh$, $Au_{19-hole}$	49
Figure 6 The optical absorption spectrum of the $Au_{24-n}Nin$ ($n = 1, 2, 3, 4, 5$) chains. ...	50
Figure 7 Dipole strength function of a quasi-one dimensional electron gas with 10 atoms	55
Figure 8 Real part of induced charge densities for a 10-atom chain.	55
Figure 9. Imaginary part of induced charge densities for a 10-atom chain.....	56
Figure 10. The Mulliken atomic charge distribution in the case of $Au_{19}X$ ($X = Au; Ni; Rh$) chains. The impurity atom is put at the site 10 from the left.	56
Figure 11. Schematic form of the positive charge background potential for the Au_{16} (a) and $Au_{15}X$ (c) chains. In the case of Au_{16} , the plasmon excitation corresponds to the charge oscillation along all the chain (b). In the case of $Au_{15}X$ chains, there are possible two kinds of plasmonic oscillations: collective plasmon excitations in each half of the chain (d) and local plasmon oscillations on both sides of the impurity atom potential wall (e).....	58
Figure 12. Absorption spectra of 20 atom pure Au chain by using <i>norbital</i> = 2.	61

Figure 13. Absorption spectra of 20 atom pure Au chain by using <i>norbital</i> = 4.	62
Figure 14 Absorption spectra of pure Au chains using tight binding approach.....	62
Figure 15. Comparison of absorption spectrum of Au ₂₀ and Au ₁₉ Ni chains.....	63
Figure 16. Atoms contributions to the local peak in Au ₁₉ Ni chain (Ni in the middle).	64
Figure 17 Analysis of the additional mode of Au ₁₉ Ni chain (black squares represent orbital 1 and red circles represents orbital 2).	65
Figure 18 Optical absorption spectra of the n-atom double Au chains, n=2-14.....	69
Figure 19 Absorption spectra of arrays of pure Au chains of 10 atoms each.	69
Figure 20 Absorption spectra of pure Au chains with different geometries -- square, zigzag (with different vertical distances between chains) and double zigzag.	71
Figure 21 Optical absorption spectra of single and double Au ₁₁ Ni chains.....	72
Figure 22 Optical absorption spectra of Au ₂₈ , Au ₂₆ Ni ₂ (Ni in the middle) and Au ₂₆ Ni ₂ (Ni at the end) chains.....	72
Figure 23 Optical absorption spectra of Au ₂₈ , Au ₂₆ Ni ₂ (Ni at the end) and Au ₂₆ Pd ₂ (Pd at the end) chains.....	73
Figure 24 Optical absorption spectra of Au ₂₈ , Au ₂₆ Pd ₂ (Pd at ends and in the middle) and Au ₂₇ Pd (Pd at the end and in the middle) chains.....	73
Figure 25 Coupled M ₁₄ N ₁₄ chains absorption spectra (a) Au ₁₄ Au ₁₄ , Ag ₁₄ Ag ₁₄ , Cu ₁₄ Cu ₁₄ , Au ₁₄ Ag ₁₄ , Au ₁₄ Cu ₁₄ , Ag ₁₄ Cu ₁₄ chains.	74
Figure 26 Coupled M ₁₄ N ₁₄ chains absorption spectra, Au ₁₄ Au ₁₄ , Au ₁₄ Ni ₁₄ , Au ₁₄ Pt ₁₄ , Au ₁₄ Pd ₁₄ , Au ₁₄ Fe ₁₄ chains.	75

Figure 27. The electron charge density in the case of two Au ₁₄ chains doped in the middle by Rh(top) and Ni (bottom) atoms.....	78
Figure 28. Mulliken atomic charge for the pure Au chains illustrated in Fig. 19 with different array sizes.	79
Figure 29. Mulliken atomic charge distribution for the pure Au chains with different geometries presented in Fig.20	80
Figure 30. Mulliken atomic charge distribution for the Ni-doped Au chains illustrated in Fig. 21 (the second chain atoms in the double chain correspond to Atoms 13-24).	80
Figure 31. Mulliken atomic charge for double Au chains – one pure, one doped with Ni in the middle, one doped with Ni at the end.	81
Figure 32. Mulliken atomic charge for the Au chains illustrated in Fig. 4: pure, end-doped with Ni and end-doped with Pd with 1 and 2 Pd atoms at different positions. ...	81
Figure 33. Mulliken atomic charge for the Au chains with 1 and 2 Pd atoms doped at different positions.	82
Figure 34. Mulliken atomic charge for coupled the M ₁₄ N ₁₄ chains illustrated in Fig. 5: Au ₂₈ , Ag ₂₈ , Cu ₂₈ , Au ₁₄ Ag ₁₄ , Au ₁₄ Cu ₁₄ , Ag ₁₄ Cu ₁₄ (b) Au ₂₈ , Au ₁₄ Ni ₁₄ , Au ₁₄ Pt ₁₄ , Au ₁₄ Pd ₁₄ , Au ₁₄ Fe ₁₄	82
Figure 35. Mulliken atomic charge for coupled the M ₁₄ N ₁₄ chains: Au ₂₈ , Au ₁₄ Ni ₁₄ , Au ₁₄ Pt ₁₄ , Au ₁₄ Pd ₁₄ , Au ₁₄ Fe ₁₄	83
Figure 36. HOMO (top) and LUMO (bottom) of two Au ₁₄ chains each doped in the middle by one Ni atom (red and blue indicate an extra and missing charge, respectively).	84

Figure 37. The same chains as in Fig. 29 but doped (also in the middle) with Pd atoms.	85
Figure 38. Schematic representation of the collective and local plasmon oscillations in double chains.	86
Figure 39 Schematic representation of an exciton.	88
Figure 40 Schematic representation of Frenkel exciton.	89
Figure 41 Schematic representation of a Wannier exciton.	90
Figure 42 Schematic of the Infinite zig-zag chain.	90
Figure 43. Band structure for infinite zig-zag chain	91
Figure 44. Absorption Spectra of pure Au chains of 14 atoms.	98
Figure 45 Absorption Spectra of Au_{13}Ni chain.	98
Figure 46 Absorption Spectra of Au_{13}Fe chain.	99
Figure 47. Absorption Spectra of Au_{13}Rh chain.	99
Figure 48. . Schematic of the Infinite zig-zag chain with finite Au_{14} chain.	100
Figure 49. Mulliken Atomic charge of Au_{14} , Au_{13}Ni , Au_{13}Fe , Au_{13}Rh	101
Figure 50 Schematic representation of graphane	109
Figure 51. Density of states of pure graphane.	110
Figure 52 Schematic diagram of monolayer MoS_2	111
Figure 53 Density of states for single layer MoS_2	112
Figure 54 (a) Phonon dispersion curve for single layer MoS_2 . (b) Schematic representation of the optical modes.	112
Figure 55 The Real and Imaginary part of the electron self-energy	115

Figure 56 The spectral function of monolayer MoS ₂	116
Figure 57 Absorption Spectrum of monolayer MoS ₂	116
Figure 58 The photoluminescence spectrum of monolayer MoS ₂ for different values of λ	117
Figure 59 Time dependence of electron temperature in doped MoS ₂	118
Figure 60 The Spectral fluence in doped MoS ₂	119
Figure 61. AFM –FM transition in bulk Fe-Rh. Transition takes place at $a=3.08\text{\AA}$	123
Figure 62. Optimized structures of Fe _x Rh _{26-x} : (a) FM Fe ₂₄ Rh ₂ , (b) AFM Fe ₂₄ Rh ₂ , (c) FM Fe ₁₄ Rh ₁₂ , (d) AFM Fe ₁₄ Rh ₁₂ , (e) FM Fe ₁₀ Rh ₁₆ , (f) AFM Fe ₁₀ Rh ₁₆ (g) FM Fe ₂ Rh ₂₄ , (h) AFM Fe ₂ Rh ₂₄	126
Figure 63 Bond length distribution of the structures shown above in Fig.62.	128
Figure 64. Magnetization/atom and coordination number for the clusters in fig.62.	129
Figure 65 FM Fe ₁₀ Rh ₁₆ (two figures are just different angles to show Fe and Rh atoms clearly).....	131
Figure 66 Partial DOS of d-orbital of Fe atoms shown in Fig.65 (a) atom number 2 (b) atom number 13	132
Figure 67 Partial DOS of d-orbital of Rh atoms shown in Fig.65 (a) atom number 22 (b) atom number 1	133
Figure 68 Highest Occupied Molecular Orbital (HOMO) of square Au ₁₀ Au ₁₀ chain.....	138
Figure 69 Highest Occupied Molecular Orbital (HOMO) of zig-zag Au ₁₀ Au ₁₀ chain	138
Figure 70 (a)HOMO and (b) LUMO of Au ₂₆ Ni ₂ chains with 2 Ni atoms in the middle of each 14 atom chain.	139

Figure 71 HOMO of (a) $\text{Au}_{26}\text{Pd}_2$ (2 Pd atoms at the end) (b) $\text{Au}_{26}\text{Pd}_1$ (1 Pd atom at the end).....	140
Figure 72 Molecular orbitals for the mixed chains (from left to right) Au-Fe , Au-Ni, Au-Pd, Au-Pt.....	141
Figure 73 (a)HOMO and (b) LUMO of $\text{Au}_{14}\text{Fe}_{14}$ chains.....	142
Figure 74 (a)HOMO and (b) LUMO of $\text{Au}_{14}\text{Ni}_{14}$ chains.....	143
Figure 75 (a)HOMO and (b) LUMO of $\text{Au}_{14}\text{Pd}_{14}$ chains.....	144
Figure 76 (a)HOMO and (b) LUMO of $\text{Au}_{14}\text{Pt}_{14}$ chains.....	145

LIST OF TABLES

Table 1. Exciton binding energy for infinite zig-zag chain with different TDDFT potentials.	92
Table 2. The dielectric constant and rate of energy transfer (equation 131) for zig-zag chain and pure, doped chains of Au.	100
Table 3 Lattice parameter and bondlength for graphene obtained by different approaches.	109
Table 4. Electron-phonon coupling constant in graphene as a function of doping.	110
Table 5 Lattice parameters for monolayer MoS ₂	111
Table 6 Electron-phonon coupling constant for different doping in monolayer MoS ₂ . .	114
Table 7. Total Energy and total Magnetization of FM and AFM Fe _x Rh _{26-x} nanoparticles.	127

CHAPTER 1 INTRODUCTION

Nanostructures form a new class of materials that possess unique properties which are neither molecular nor bulk-like and because of these novel properties, nanoparticles have become the focus of considerable research in many fields such as catalysis¹, optical communications², nanoelectronics³, biomedicine^{4, 5}. The under coordinated surface atoms play a significant role in the unique properties of nanoparticles as does its large surface to volume ratio, so that there are large numbers of surface atoms. The properties of the systems can thus be tuned by changing the particle size, i.e. changing the surface to bulk atoms ratio. The properties of nanoparticles also depends strongly on their shape and composition⁶. Many experimental and theoretical works are being dedicated to understand the above dependencies and eventually trying to control and manipulate the properties of nanoparticles by varying size, shape, composition, as well as some other parameters, such as the environment, substrate, external fields, etc. Theoretical calculations play a central role in better understanding the complex physics of nanoparticles. Not only do they provide interpretations for many experimental observations, but also predict the most suitable systems for different applications. In this work, we focus on computational studies of the optical and magnetic properties of several types of nanostructures: chains, particles and infinite monolayer. As the size of the system decreases, quantum effects come into the picture, which need to be taken into account. Therefore, in order to understand the optical and magnetic properties of

the systems we will use quantum mechanical approaches, in particular, Density Functional Theory (DFT), Time-Dependent Density-Functional Theory (TDDFT) and the many-body Green's function approach.

In the case of *the optical response*, we focus on plasmonic and excitonic properties, as well as on the interaction between plasmons and excitons. Noble metal nanostructures have attracted considerable attention in the field of optical spectroscopy, since silver and gold exhibit strong absorption in the visible region of the spectrum with different colors, such as yellowish for silver and burgundy for gold spherical particles⁷. The origin of this absorption is attributed to collective electron charge density oscillation in response to external electromagnetic radiation. These collective excitations of electrons are called plasmons. Plasmonics is one of important branches of optics. Plasmons have the ability to concentrate light at nano-scale and also to enhance the local electromagnetic field. While bulk and surface plasmons have been studied in many systems in great detail, plasmons in sub-nanometer structures is a relatively new field. The plasmon absorption band strongly depends on the shape of the nanostructures. In the case of gold and silver structures, one can tune in principle the position of plasmon peaks to any frequency in the visible range, i.e. to any possible color, by controlling the shape or the structure of the nanomaterial⁸⁻¹⁰. For practical applications, it is essential to be able to tune the plasmon resonance to a desired frequency. In particular, it can be used in solar cell technologies, sensor devices, etc. Greater versatility in the tuning of properties may be achieved by using structures that consist of several different

elements, in particular the dielectric core - metallic shell particles with different types of fundamental excitations (plasmons and excitons),^{11, 12} two or more coupled particles with hybridized excitations of individual clusters^{13, 14}. Linear chains of nanoparticles have also been proposed as possible candidates for electromagnetic energy transport¹⁵⁻¹⁷, catalysis¹⁸ and as efficient nanolens¹⁹. Also, the Scanning Tunneling Microscope (STM)-creation of chains of gold atoms (up to 20-atom long) on NiAl (110) substrate has sparked an interest in the optical properties of the atomic chains²⁰. Since the optical properties of such chains and nanoparticles potentially have many practical applications, it is very important to understand the nature of the excitations in these systems, the most pronounced of which are plasmons. In this work, we study the absorption spectrum of single and multiple chains of pure Au as well as Transition-metal (TM) doped chains of Au. It is shown that the doping opens additional opportunities to tune the system properties, including the plasmon response. We have also studied the case of coupled chains, which consist of different types (noble and TM) of chains.

We also study another important excitation – excitons. Excitons are bound states of electrons and holes that play an important role in the optical response of semiconductors and insulators. Unlike plasmons, excitons are formed in systems with energy gap. We have considered Au chains with a geometry that leads to a bandgap in the electronic spectrum (like zigzag chains) with ability to create exciton states. Creating coupled systems of “plasmon” and “exciton” chains opens an opportunity to tune the optical response by creating corresponding hybridized states or transferring the energy

between these two types of excitations. We have studied such a possibility, and found that the energy transfer is especially efficient when the system is doped with TM impurities.

We also study *the ultrafast response*, including femto-second emission, in monolayer MoS₂. Monolayer MoS₂ shows a great potential to be used in novel nanoelectronics and nano-optical devices. One of the characteristic features of single layer MoS₂ is that it shows strong luminescence as opposed to its bulk counterpart which is attributed to its direct band gap. There are evidences of strongly bound excitons and trions in the optical absorption spectrum and the doped system demonstrates high electron mobility. Study of the slow and ultrafast (~100fs) optical response of monolayer MoS₂ is also important from the point of view of science and technological applications. We have carried out DFT calculations of the photoluminescent properties of monolayer MoS₂. In particular, we have analyzed the role of electron-phonon interactions in the photoluminescence process. Phonon properties were used to calculate electron self-energy and spectral function. We found that the photoemission spectrum is in good agreement with experimental data. We focused on the ultrafast relaxation of the electron system resulting from electron-phonon interaction and evaluated the photoluminescence of the excited system by using the effective electron temperature model²¹. It is shown that similar to graphene, MoS₂ demonstrates significant ultrafast photoluminescence.

Finally, we studied *the magnetic properties* of small bimetallic clusters. Nanoparticles possess very unique magnetic properties, different from their bulk counterparts, e.g. non-magnetic bulk materials are magnetic in nanometer scale. The magnetic properties of nanoparticles can also be manipulated by changing size, shape or composition of nanoparticles. Bimetallic nanoparticles are of particular interest, since in these systems novel properties can be generated by just changing the chemical composition. Pure TM clusters such as Fe, Co, and Ni have spin and orbital moments and magnetic anisotropy energy that are much enhanced as compared to their respective bulk structures. Alloying 3d and comparatively heavier 4d and 5d elements is particularly interesting. In particular, bulk FeRh alloy has been actively studied with regard to the Antiferromagnetic (AFM)- Ferromagnetic (FM) transition at $T \sim 300\text{K}$ ²². It is very interesting to note that similar bimetallic alloy FePt does not demonstrate this transition (it undergoes FM-paramagnetic (PM) transition at $T \sim 730\text{K}$ ²³). With the study of magnetic properties of FeRh nanostructures, it might be possible to get an insight into the origin of the FM-AFM transition in the bulk. Towards this end we performed spin-DFT calculations for these structures with different ratios of Fe and Rh atoms. We systematically studied the ferromagnetic properties, including the individual atom magnetization, of the clusters as function chemical composition. We found that the Rh atoms have a rather large magnetic moment (up to $\sim 1\mu\text{B}$), which does not differ significantly for the surface and bulk atoms. In contrast, surface Fe atoms have much larger magnetization ($\sim 3\mu\text{B}$) comparing to the bulk atoms. In particular, we find that the

FM phase is extremely stable in these systems, and the magnetization can be tuned by changing the chemical composition of the clusters.

This thesis is organized as follows: after Introduction (Chapter 1), in Chapter 2, I explain the computational methods that I have used to study the optical and magnetic properties of nanoparticles. Chapter 3 is devoted to two important optical excitations in nanostructures: plasmons and excitons. In particular, I present results for the absorption spectra of single and multiple pure Au chains, TM chains and TM-doped Au chains. In this Chapter, I also try to analyze possibility of collective and local excitations in the systems under study. In addition, I report results for possible excitations in infinite pure zig-zag Au chain coupled to finite pure and TM-doped Au chains. In Chapter 4, I present details of calculations and results for the absorption and emission spectra of monolayer MoS_2 , as well as results for the processes of the ultrafast emission. In Chapter 5, I consider the magnetic properties of 26-atom FeRh nanoparticles and analyze the dependence of the magnetization on the chemical composition and inter-atomic distance. Finally, in Chapter 6 I give a summary of the results and some future prospects for given studies.

CHAPTER 2 THEORETICAL METHODS

2.1 Density Functional Theory

Density Functional Theory (DFT) is a phenomenological quantum mechanical tool to study the electronic structure and some other properties of matter²⁴. This theory can be applied to atoms, molecules, clusters, bulk materials, nuclei, quantum fluids, etc. Most of the properties of materials are defined by their electronic structure and electronic structure calculations are done by using first principles approaches. DFT allows one to obtain the ground state energy and the electron density of the system, though many other material properties can be obtained from these quantities. The ultimate goal of all approaches is to solve approximately the Schrodinger equation, which defines the behavior of many-particle systems in condensed matter physics and quantum chemistry:

$$\hat{H}\psi_i(\vec{r}_1, \vec{r}_2, \dots, \vec{r}_n, \vec{R}_1, \vec{R}_2, \dots, \vec{R}_N) = E_i\psi_i(\vec{r}_1, \vec{r}_2, \dots, \vec{r}_n, \vec{R}_1, \vec{R}_2, \dots, \vec{R}_N) \quad (1)$$

$$\hat{H} = \hat{T}_e + \hat{T}_N + \hat{V}_{e-e} + \hat{V}_{e-N} + \hat{V}_{N-N}, \quad (2)$$

where \hat{H} is the Hamiltonian operator of the system that is composed of the kinetic energy of electron and nuclei terms \hat{T}_e and \hat{T}_N , the electron-electron interaction and electron-nucleii interaction terms \hat{V}_{e-e} , and \hat{V}_{e-N} , and the nucleus-nucleus repulsion term

\hat{V}_{N-N} :

$$\hat{H} = -\frac{1}{2}\sum_{i=1}^n \nabla_i^2 - \frac{1}{2}\sum_{A=1}^N \frac{1}{M_A} \nabla_A^2 + \sum_{i=1}^n \sum_{j>1}^n \frac{1}{r_{ij}} - \sum_{i=1}^n \sum_{A=1}^N \frac{Z_A}{r_{iA}} + \sum_{A=1}^N \sum_{B>A}^N \frac{Z_A Z_B}{R_{AB}} \quad (3)$$

The summation indices i, j run over n electrons, whereas A, B indices run over N nuclei in the system. The exact solution to this equation is impossible owing to complexity that increases as the number of particles increases. So, we have to use approximations, like Born-Oppenheimer approximation which states that electron and nucleus degrees of freedom can be decoupled. Due to much heavier mass, nuclei move much slower as compared to electrons, therefore one can consider the problem of motion of electrons in “static” potential of nuclei, and the correction for the effects of electrons on the nuclei can be taken into account after the equilibrium distribution of electrons has been found. In the “static” approximation, the Hamiltonian reduces to the electronic Hamiltonian:

$$\hat{H}_{elec} = -\frac{1}{2} \sum_{i=1}^n \nabla_i^2 + \sum_{i=1}^n \sum_{j>1}^n \frac{1}{r_{ij}} - \sum_{i=1}^n \sum_{A=1}^N \frac{Z_A}{r_{iA}}. \quad (4)$$

The total energy is equal to the electronic energy plus the energy of the inter-nucleus interaction:

$$\hat{H}_{elec} \psi_{elec} = E_{elec} \psi_{elec} \quad (5)$$

$$E_{tot} = E_{elec} + \sum_{A=1}^N \sum_{B>A}^N \frac{Z_A Z_B}{R_{AB}}. \quad (6)$$

The Born-Oppenheimer approximation makes the problem simpler by excluding the nucleus degree of freedom, though the remaining multi-electron problem is still complicated and one needs to make more approximations. The simplest one is the Hartree approximation that decouples the electronic wave function into product of single electron orbitals and thus gives n equations for n electrons:

$$\psi(\vec{r}_1, \vec{r}_2, \dots, \vec{r}_n) = \varphi_1(\vec{r}_1) \varphi_2(\vec{r}_2) \dots \varphi_N(\vec{r}_N), \quad (7)$$

$$\left[-\frac{1}{2} \sum_{i=1}^n \nabla_i^2 - \sum_{i=1}^n \sum_{A=1}^N \frac{Z_A}{r_{iA}} + \sum_{j \neq i} \int |\varphi_j(\vec{r}_j)|^2 \frac{1}{|\vec{r}_j - \vec{r}_i|} d\vec{r}_j \right] \varphi_1(\vec{r}_1) = \varepsilon \varphi_1(\vec{r}_1). \quad (8)$$

However, this approximation fails to take into account properly the Pauli exclusion principle, expressed in particular in the asymmetry of the wave function with respect to interchange of two electrons. This property is taken into account in the Hartree-Fock approximation. The wave function in the Hartree-Fock approximation is the Slater determinant constructed from single-electron orbitals:

$$\psi(\vec{r}_1, \vec{r}_2, \dots, \vec{r}_n) = \frac{1}{\sqrt{n!}} \begin{vmatrix} \varphi_\alpha(\vec{r}_1) & \varphi_\beta(\vec{r}_1) & \dots & \varphi_v(\vec{r}_1) \\ \varphi_\alpha(\vec{r}_2) & \varphi_\beta(\vec{r}_2) & \dots & \varphi_v(\vec{r}_2) \\ \dots & \dots & \dots & \dots \\ \dots & \dots & \dots & \dots \\ \varphi_\alpha(\vec{r}_N) & \varphi_\beta(\vec{r}_N) & \dots & \varphi_v(\vec{r}_N) \end{vmatrix}. \quad (9)$$

The exchange of two particles is equivalent to the exchange of two columns, which induces a change of sign. Also note that if two rows are equal, the determinant is zero which takes into account the Pauli's exclusion principle: two (or more) identical fermions cannot occupy the same state. Although the Hartree-Fock approximation is much accurate than Hartree one, it is still is not the exact solution. It would be exact if the interactions were described just by the Pauli principle: electrons with the same quantum numbers avoid each other (exchange interaction). In other words, one needs to take into account also effects of explicit Coulomb interaction between electrons, i.e. so called correlation effects. Even the Hartree-Fock approximation is computationally expensive in the case of dozens or more electrons, but the correlation effects make the problem

much more difficult to solve, or in other words the approach mentioned above is computationally very expensive.

One can avoid this complexity by using DFT which maps many-electron problem onto a single-electron one. DFT has become remarkably popular because of its good balance between accuracy and computational cost. In DFT, the electron density determines all ground state properties of the system. Hohenberg and Kohn²⁵ established two theorems which constitute the theoretical foundation of DFT. The first theorem states that for any system of interacting electrons, there is one-to-one correspondence (up to a trivial additive constant) correspondence between the effective external potential $v_{ext}(r)$ that governs the properties of the effective electron with the same charge density as in the many-electron system and the ground-state particle density $n(r)$. The second theorem states that the free energy functional $F_{HK}[n]$ for the interacting electron system, gives the lowest energy of the system if and only if the charge density is the ground state density, i.e.

$$E_0 \leq E_{v_{ext}}[n] \quad (10)$$

and

$$E_{HK}[n] = F_{HK}[n] + \int v_{ext}(r)n(r)dr, \quad (11)$$

where, $F_{HK}[n]$ is a universal functional of the density which does not depend on $v_{ext}(r)$ and, $E_{HK}[n]$ is minimal at the exact ground-state density $n_0(r)$. In simple words, all ground state properties of the system are defined by $n(r)$ which is related to the total

energy by equation (11) and is the energy has minimum only when $n(r)$ is equal to the ground state density. The HK theorems provide general theoretical basis for calculations, but they do explain how to deal with the quantum many-body problem in practice. A practical formulation of DFT was provided by the Kohn and Sham (KS)²⁶. In their approach, the energy functional can be expanded as:

$$E_{HK}[n] = T_0[n] + E_H[n] + E_{xc}[n] + \int v_{ext}(r)n(r)dr, \quad (12)$$

where T_0 is kinetic energy of the non-interacting electrons, $E_H[n]$ is the classical electrostatic (Hartree) energy, given by

$$E_H[n] = \frac{1}{2} \iint \frac{n(r)n(r')}{|r-r'|} drdr', \quad (13)$$

$E_{xc}[n]$ is the exchange-correlation (XC) energy which contains the non-classical interaction energy and the difference between the kinetic energies of the interacting and non-interacting systems. The exact form of $E_{xc}[n]$ is not known exactly. By applying the variational principle of the second theorem to the HK energy functional, one can obtain the Euler equation for the interacting electrons

$$\frac{\delta T_0[n]}{\delta n(r)} + V_{KS}(r) = \mu,$$

$$\text{where} \quad (14)$$

$$v_{KS}(r) = v_{ext}(r) + v_H[n](r) + v_{xc}[n](r), \quad (15)$$

$$v_{KS}(r) = v_{ext}(r) + \int dr' \frac{n(r')}{|r-r'|} + \frac{\delta E_{xc}[n]}{\delta n(r)}, \quad (16)$$

and μ is a Lagrange multiplier that enforces the conservation of the total number of particles. The same equation can also be obtained by applying the variational principle to a system of non-interacting electrons in an effective potential $v_{KS}(r)$. The many-electron wave function, thus, can also be represented by Slater determinant of single electron functions, which are eigenfunctions of the corresponding Hamiltonian:

$$\left[-\frac{1}{2} \nabla^2 + v_{KS}(r) \right] \phi_i(r) = \epsilon_i \phi_i(r), \quad (17)$$

with the particle density constraint

$$n(r) = \sum_{i=1}^N |\phi_i(r)|^2, \quad (18)$$

$n(r)$ is the electron density obtained from summation over all occupied states. Equations (17) and (18) are the key equations of DFT and are known as KS equations. Once one knows density-dependent $v_{KS}(r)$, he can plug it into equation (17) which gives the orbitals and ground state charge density by using Eq. (18), i.e. Eqs. (17), (18) have to be solved self-consistently. The KS potential is often used as local and depends only on the coordinates of given particle, but it effectively takes into account the interaction of the electrons with other electrons. It is important to note that KS orbitals have, in principle, no physical significance, they are just functions used to obtain the ground-state energy and charge density of the full many-body system, though in general they are used as low-interaction limit for the electron wave functions.

2.1.1 Exchange-Correlation Functional

The solution of KS equations is exact provided $E_{xc}[n]$ is exact. As the correct form of $E_{xc}[n]$ is still unknown, various approximations have been applied to get better results.

The simplest approximation is the Local Density Approximation (LDA), which assumes that the $E_{xc}[n]$ energy of a real system behaves locally as that of the uniform electron gas. This is a system where electrons move in positive charge background such that the total system is neutral. The $E_{xc}[n]$ functional is expressed as

$$E_{xc}^{LDA}[n] = \int \varepsilon_{xc}^{hom}(n(r))n(r)dr \quad (19)$$

ε_{xc}^{hom} is the XC energy per electron of the homogeneous electron gas of density $n(r)$.

The quantity $E_{xc}[n]$ can be split into the exchange and correlation parts: $E_x[n] + E_c[n]$.

For the homogeneous electron gas $E_x[n] = -\left(\frac{81}{64}\right)^{1/3} n^{1/3}(r)$ is obtained from the Hartree-Fock approximation for the free homogeneous gas, but the expression for the correlation term is very difficult to calculate even in this case. LDA is rather accurate in the limit of high density or slowly varying density distributions, when it is possible to determine the correlation term. Typically LDA can reproduce the structural and vibrational properties of strongly bound systems very well. LDA overestimates adsorption energies of molecules by 10%~20% and underestimates bond lengths by ~2%. LDA also fails in calculating dissociation energies, some magnetic properties, in the cases of heavy fermions and systems where electron-electron interactions are dominant, etc. Therefore, there is a need to go beyond this approximation. As the first improvement, the Generalized Gradient Approximation (GGA) has been proposed. In

this approximation one takes into account the gradient-corrections to the LDA charge density energy, which takes into account the non-homogeneity effects:

$$E_{xc}^{GGA}[n] = \int \varepsilon_{xc}^{hom}(n(r), |\nabla n(r)|) n(r) dr, \quad (20)$$

or

$$E_{xc}^{GGA}[n] = \int A_{xc}[n] n(r)^{4/3} dr + \int B_{xc}[n] |\nabla n(r)|^2 / n(r)^{4/3} dr, \quad (21)$$

In the last expression, the XC energy includes the lowest-order charge density gradient $|\nabla n(r)|$. The corresponding higher-order expansion (so called Generalized Gradient Expansion (GGE) approximation) leads to a solution that is not stable and does not converge monotonically. So, direct expansion, like in Eq. (21), is not promising approach. Another way is to obtain the expression for the XC that depends on the density and the gradients from other theoretical (phenomenological) reasons, and set the unknown parameters in such a way that different formal exact constraints are satisfied and some known results are reproduced. Alternatively, one can fit the parameters of the functional in order to reproduce a number of experimental results. Several expressions for GGA XC potentials have been considered. The GGA usually significantly improves the LDA results, like in predicting the binding energies of real materials. It has managed to keep the correct features of LDA and add to that the inhomogeneity features which are energetically very important.

BLYP Functional: In 1988, Becke proposed a functional where parameters are fitted to experimental molecular data. The exchange and correlation energy terms have the following form:

$$\varepsilon_X = \varepsilon_X^{LDA} \left(1 - \frac{\beta}{2^{1/3} A_x} \frac{x^2}{1 + 6\beta x \sinh^{-1}(x)} \right), \quad (22)$$

where $x = 2(6\pi^2)^{1/3} s = 2^{1/3} |\nabla n(r)|/n(r)^{4/3}$, $A_x = (3/4)(3/\pi)^{1/3}$, $\beta = 0.0042$,

$$\varepsilon_c = -\frac{a}{1+dn^{-1/3}} \left\{ n + bn^{-2/3} \left[C_F n^{5/3} - 2t_w + \frac{1}{9} \left(t_w + \frac{1}{2} \nabla^2 n \right) \right] e^{-cn^{-1/3}} \right\}, \quad (23)$$

$$t_w = \frac{1}{8} \left(\frac{|\nabla n|^2}{n} - \nabla^2 n \right), \quad (24)$$

and $C_F = 3/10(3\pi^2)^{2/3}$, $a = 0.04918$, $b = 0.132$, $c = 0.2533$, $d = 0.349$.

PBE Functional: In 1996, Perdew, Burke, and Enzerhof (PBE)²⁷ proposed this functional which satisfies many formal properties and limits. The PBE XC energy can be written in terms of what is called the enhancement parameter that depends on density, its gradient and higher powers of that:

$$E_{XC}[n] = \int n(r) \varepsilon_{XC}[n(r)] F_{XC}[n(r), \nabla n(r), \nabla^2 n(r), \dots] dr. \quad (25)$$

In PBE functional, the exchange part of the enhancement parameter $F_X(n, \zeta, s)$ depends on the charge density n , spin polarization density ζ , and a dimensionless parameter given by $s = |\nabla n(r)|/(2k_F n)$

$$F_X(s) = 1 + \kappa - \frac{\kappa}{1 + \frac{\mu s^2}{\kappa}}, \quad (26)$$

where $\mu = \beta \left(\frac{\pi^2}{3} \right) = 0.21951$ and $\beta = 0.066725$ are related to the second order gradient expansion, and $\kappa = 0.804$. This form of equation obeys the spin scaling relationship and reproduces LSDA limit $s \rightarrow 0$. In addition, it also satisfies the uniform scaling condition and recovers the correct uniform electron gas limit, i.e $F_X(0) = 1$. The correlation energy is similar to what is proposed by Perdew and Wang (PW91)²⁸⁻³⁰, and is given as:

$$E_C^{GGA} = \int n(r) \left[\varepsilon_C^{LDA}(n, \zeta) + H[n, \zeta, t] \right] dr, \quad (27)$$

$$H[n, \zeta, t] = (e^2/a_0) \gamma \phi^3 \ln \left\{ 1 + \frac{\beta}{\gamma} t^2 \left[\frac{1 + A t^2}{1 + A t^2 + A^2 t^4} \right] \right\}, \quad (28)$$

$$t = \frac{|\nabla n(r)|}{2\phi k_s n}, \quad (29)$$

where k_s is the Thomas-Fermi screening wave number and $\phi(\zeta) = [(1 + \zeta)^{2/3} + (1 - \zeta)^{2/3}]/2$ is the spin scaling factor. The other parameters are: $\gamma = \frac{(1 - \ln 2)}{\pi^2} = 0.031091$ and

$$A = \frac{\beta}{\gamma} \left[e^{-\varepsilon_C^{LDA}[n]/(\gamma \phi^3 e^2/a_0)} - 1 \right]^{-1}. \quad (30)$$

PBE functional gives good results in many cases. Other important advantages of it is parameter-independence and the fact that it satisfies the exact exchange-correlation hole condition.

Hybrid Functionals: The functionals mentioned above are inadequate to solve problems where the density is not varying slowly. For this case, hybrid functionals were introduced. They consist of DFT and Hartree-Fock parts (the correlation part comes from DFT and the exchange part is combined expression of both DFT and Hartree-Fock parts). In a very general form, the hybrid XC energy can be expressed as

$$E_{XC}^{hyb} = \alpha E_X^{HF} + (1 - \alpha) E_X^{DFT} + E_C^{DFT}, \quad (31)$$

Where α is a fitting parameter (though often put $\frac{1}{2}$ or a value of the same order of magnitude). Popular hybrid functionals, like B3LYP³¹, have the following structure:

$$E_{XC}^{hyb} = \alpha E_X^{Slater} + (1 - \alpha) E_X^{HF} + \beta * \Delta E_X^{Becke} + E_C^{VWN} + \gamma * \Delta E_C^{non-local}, \quad (32)$$

where, α , β , γ are obtained by fitting to the experimental results for a certain set of molecules. VWN³² is a correlation functional, fitting the RPA solution to the uniform electron gas, often referred to as Local Spin Density (LSD) correlation energy. The last, LYP³³ term, is the correlation term that includes both local and non-local contributions. Another popular functional, B3PW91, includes a non-local correlation term given proposed by Perdew and Wang²⁸. These and some other hybrid functionals are computationally not very expensive, and reproduce the geometries, binding energies and other properties of molecular system with a better accuracy comparing to LDA. In this thesis, we use LDA, GGA and hybrid functionals, like B3PW91.

2.1.2 Spin-Density Functional Theory

For many problems in condensed matter physics, for e.g. to calculate the magnetic properties of the system, one has to take into account the spin degrees of freedom. Therefore, one can extend the KS theory on the case of spin densities, which define the total charge density of electrons:

$$n(r) = n_{\uparrow}(r) + n_{\downarrow}(r), \quad (33)$$

$$n_s(r) = \sum_{i=1}^{N_s} |\phi_{i,s}(r)|^2 \quad (34)$$

where s corresponds to spin-up and –down, and N_s is the number of electrons with spin s. The spin-dependent orbitals satisfy the KS equations

$$\left[-\frac{1}{2} \nabla^2 + v_{KS,s}(r) \right] \phi_{i,s}(r) = \epsilon_{i,s} \phi_{i,s}(r), \quad (35)$$

where the spin-dependent KS potential is defined by the spin-dependent XC energy:

$$v_{KS}(r) = v_{ext}(r) + \int dr' \frac{n_{\bar{s}}(r')}{|r-r'|} + \frac{\delta E_{XC}[n_{\uparrow}, n_{\downarrow}]}{\delta n_s(r)} \quad (36)$$

In general, the XC energy functional depends on the total charge density (21) and spin polarization density

$$\zeta(r) = n_{\uparrow}(r) - n_{\downarrow}(r). \quad (37)$$

In the Spin-Density Functional Theory it is assumed that the projection of total spin of the system is a good quantum number. However, this theory fails in the case of non-

collinear magnetism, which can be studied by using Pauli spin matrices along with the spin polarization density vectors.

2.1.3 DFT+U

DFT fails to generate correct results for systems that have localized d- and f –orbitals. It is because LDA corresponds to (locally) homogeneous electron gas, where the electrons are delocalized and some sort of mean-field (averaged and in general weak) electron-electron interaction is assumed. However, it is known that in many systems, like transition-metal oxides and rare earth materials, electrons are localized, so placing an additional electron on given site/orbital will cost rather large (~1-10eV) additional energy, usually defined by letter U. This situation was originally considered by Hubbard. The simplest way to correct the DFT results in the case of such systems is to add the Hubbard term accounting the interaction of localized electrons. In this case, the Hilbert space of the crystal can be divided into weakly correlated subspace that can be studied by the DFT approach, and the strongly-correlated subspace, for which one needs to include the local Coulomb interaction processes in full detail. The Coulomb interaction part of the Hamiltonian in terms of creation and annihilation operators is given as

$$\hat{H}_{coulomb} = \frac{1}{2} \sum_{i=d, l=l_d} \sum_{m, m', m'', m''', \sigma, \sigma'} \langle m, m' | V_{ee} | m'', m''' \rangle \times \hat{c}_{ilm\sigma}^\dagger \hat{c}_{ilm'\sigma'}^\dagger \hat{c}_{ilm''\sigma} \hat{c}_{ilm''' \sigma'},$$

(38)

where i is the atomic site index, n, l, m are energy, orbital momentum and its projection quantum numbers and σ is the spin index. V_{ee} is the screened Coulomb interaction potential. $\hat{c}_{ilm\sigma}^\dagger$ and $\hat{c}_{ilm\sigma}$ are the creation and annihilation operators. The Hamiltonian (38) allows the mixing of all possible combinations of m , some of which are not allowed taking into account the crystal symmetry. More precisely, the Hamiltonian (38) can be rewritten as

$$\begin{aligned} \hat{H}_{coulomb} = & \frac{1}{2} \sum_{i=i_d, l=l_d} \sum_{m, m', \sigma} \{ U_{mm'} \hat{n}_{ilm\sigma} \hat{n}_{ilm'\bar{\sigma}} + (U_{mm'} - J_{mm'}) \hat{n}_{ilm\sigma} \hat{n}_{ilm'\sigma} \} - \\ & \frac{1}{2} \sum_{i=i_d, l=l_d} \sum_{m \neq m', \sigma} J_{mm'} \{ \hat{c}_{ilm\sigma}^\dagger \hat{c}_{ilm\bar{\sigma}} \hat{c}_{ilm'\bar{\sigma}}^\dagger \hat{c}_{ilm'\sigma} + \hat{c}_{ilm\sigma}^\dagger \hat{c}_{ilm\bar{\sigma}}^\dagger \hat{c}_{ilm'\sigma} \hat{c}_{ilm'\bar{\sigma}} \}. \end{aligned} \quad (39)$$

In the last expression, $U_{mm'}$ is the direct Coulomb interaction matrix, while $J_{mm'}$ is the exchange-interaction matrix:

$$U_{mm'} \equiv \langle m, m' | V_{ee} | m, m' \rangle, \quad J_{mm'} \equiv \langle m, m' | V_{ee} | m', m \rangle. \quad (40)$$

In Equation (39), the last term is interaction terms that cannot be represented in terms of density operators. The first part in the last brackets correspond to the spin flip for m and m' orbitals, i.e. $\bar{\sigma} = \downarrow (\uparrow)$ to $\sigma = \uparrow (\downarrow)$ and the second part represents pair transition of two electrons with opposite spins from one orbital to another. These two contributions are often neglected in calculations, since they are relatively small, and their neglect allows one to simplify significantly the problem. In this case, the Hamiltonian reduces to

$$\hat{H}_{coulomb} = \frac{1}{2} \sum_{i=i_d, l=l_d} \sum_{m, m', \sigma} \{ U_{mm'} \hat{n}_{ilm\sigma} \hat{n}_{ilm'\bar{\sigma}} + (U_{mm'} - J_{mm'}) \hat{n}_{ilm\sigma} \hat{n}_{ilm'\sigma} \}, \quad (41)$$

or farther,

$$\hat{H}_{coulomb} = \frac{1}{2} \sum_{i=l_d, l=l_d} \sum_{m, m', \sigma} \{ [U \delta_{mm'} + U' (1 - \delta_{mm'})] \hat{n}_{ilm\sigma} \hat{n}_{ilm'\bar{\sigma}} + (U' - J) \hat{n}_{ilm\sigma} \hat{n}_{ilm'\sigma} \}, \quad (42)$$

where $U_{mm} = U, U_{mm'} = U' \equiv U - 2J$.

Unfortunately the corresponding DFT+U solution contains so called double counting problem. Namely, the correlation part of the energy is counted twice in this case: by LDA (although in a very rough way) and by the U-correction. The problem is fixed by subtracting the mean-field local correction term in the Hamiltonian (which mostly cancels the LDA contribution to the correlation energy):

$$\hat{H} = \hat{H}_{LDA} - \hat{H}_{DC} + \hat{H}_{coulomb}, \quad (43)$$

where

$$\hat{H}_{DC} = \sum_{ilm\sigma} \epsilon_{DC} \hat{n}_{ilm\sigma}, \quad (44)$$

$$\epsilon_{DC} = \bar{U} \left(n_d - \frac{1}{2} \right) \quad (45)$$

and \bar{U} is the average value of the interaction energies U and J over all orbitals, and n_d is the number of electrons in the corresponding shell.

2.2 Combined DFT and Many-Body Approaches

2.2.1 Green's Function and GW Approximation

In the GW approximation, the one-electron Green's function is calculated by taking into account the long-range screened Coulomb repulsion effects that modifies the electron self-energy. The Green's function represents the probability of finding an electron at position r and at time t given that an electron was present at position r' at time t_0 . From Green's function one can calculate the total energy, electronic density, density of states, electronic excitations and many other properties. Green's function can be obtained by solving the following equation:

$$\left\{ -\frac{\hbar^2}{2m} \nabla^2 + v_{ext}(r) - E \right\} G(r, r'; E) + \int \Sigma(r, r''; E) G(r'', r'; E) dr'' = -\delta(r - r'), \quad (46)$$

where $\Sigma(r, r''; E)$ is the self-energy of the electron that describes the interaction effects. If the exact Green's function $G_0(r, r'; E)$ for the reference system (the non-interacting Green's function) and the self-energy are known then by using Dyson's equations it is possible to generate the required Green's function:

$$G(r, r'; E) = G_0(r, r'; E) + \iint G_0(r, r_1; E) \Delta \Sigma(r_1, r_2; E) G(r_2, r'; E) dr_1 dr_2, \quad (47)$$

$$\Delta \Sigma(r_1, r_2; E) = \Sigma(r_1, r_2; E) - v_2(r_1, r_2) \quad (48)$$

where $v_2(r_1, r_2)$ is the interaction potential of the reference system, which is equal to zero for the non-interacting electrons. The single particle Green's function can be expressed using the solution for the single-particle orbitals $\varphi_n(r)$ and eigenvalues ε_n :

$$G_0(r, r'; E) = \sum_n \frac{\varphi_n(r) \varphi_n^*(r')}{E - \varepsilon_n}. \quad (49)$$

In general, the reference system can either be the Hartree-Fock or Kohn-Sham system.

In the LDA approximation, the self-energy of the non-interacting system is given as

$$\Delta\Sigma = \Sigma - v_H - \mu_{XC}, \quad (50)$$

where v_H is the Hartree potential and μ_{XC} is the LDA XC potential. In order to get correct self-energy that includes all many-body interaction effects one has to solve many-body problem with two-particle Green's functions, which is very complicated. A simpler approach is the GW approximation which takes into account only the first term in the expansion of self-energy in terms of the dynamically screened Coulomb interaction W :

$$\Sigma_{GW}(r, r'; E) = i \int G(r, r'; E + E') W(r, r'; E) dE', \quad (51)$$

$$W(r, r'; E) = v_2(r, r') + \iint W(r, r_1; E) P(r_1, r_2; E) v_2(r_2, r') dr_1 dr_2, \quad (52)$$

$$P(r_1, r_2; E) = -i G(r, r'; E) G(r', r; E). \quad (53)$$

Equations (47), (51-53) are solved self-consistently and give more accurate comparing to DFT results for the properties of the many-body system.

2.2.2 DFT+DMFT

Dynamical Mean-Field Theory (DMFT) takes into account correlation effects more accurately, as compared to DFT+U. The approach is similar to DFT+U, but it works also for intermediate values of U , which is often the case in materials of interest. While, DFT

+U treat correlation effects much better as compared to DFT, it does not take into account dynamical effects, which can lead to wrong results. DMFT takes dynamical effects into account (time-resolved local interactions between electrons). It has been successfully applied to study many properties of bulk and layered materials. We formulated a DFT-DMFT approach to study the physical properties of nanostructures and apply the formalism to analyze the magnetic properties of small clusters^{34, 35}. In DFT+DMFT method, the ground state of the system and the non-correlated properties are obtained using DFT and the correlation effects are included via the short-range Coulomb interaction of the quasi-particles within a Hubbard-type tight-binding model. The Hubbard Hamiltonian which contains the hopping (kinetic energy of electrons jumping from one site to other) and Coulomb repulsion parameters has the following expression:

$$H = \sum_{\langle ij \rangle \sigma} t_{ij} c_{i\sigma}^{\dagger} c_{j\sigma} + \sum_i U_i n_{i\uparrow} n_{i\downarrow} . \quad (54)$$

This Hamiltonian can be solved by considering the time-ordered Green's Function:

$$G(r, t, r', t') = -i \langle T c_{i\sigma}(t) c_{j\sigma}^{\dagger}(t') \rangle, \quad (55)$$

which is connected with the self-energy through Equation (47). In the case of high-dimensionality d , the problem can be reduced to the single-site problem with local Green's Function given as

$$G(\omega) = \sum_K \frac{1}{(\omega) + \mu - \epsilon(k) - \Sigma(k, \omega)}, \quad (56)$$

where μ is the chemical potential and $\epsilon(k)$ is the free quasiparticle spectrum, $\Sigma(k, \omega)$ is the self-energy. DMFT assumes the self-energy to be local in space, so it is site-independent $\Sigma(k, \omega) \approx \Sigma_{imp}(\omega)$. The non-local self-energy corrections are of order $1/\sqrt{d} \sim 1/\sqrt{Z}$, where Z is the coordination number³⁶. Thus, the DMFT approach is accurate in the case of high-dimensional systems and highly-coordinated clusters. Frequency-(time-) dependence of the self-energy means that time-dependent (dynamical) effects of the local interactions are taken into account. The DMFT problem is equivalent to solving a single-site problem of electron interacting with a bath, which corresponds to the Anderson impurity model. The effective field of the bath is given as

$$\mathcal{G}(\omega) = \sum_K \frac{1}{\omega - \epsilon_0 + \mu - \epsilon(k) - \Delta(\omega)}, \quad (57)$$

where

$$\Delta(\omega) = \sum_{k,\sigma} \frac{|V_k|^2}{\omega - \epsilon_k^b}, \quad (58)$$

and is connected with the Green's function and the self-energy in the following way:

$$G^{-1}(\omega) = \mathcal{G}^{-1}(\omega) - \Sigma(\omega). \quad (59)$$

These equations follow from the equivalence of the many-body single-electron and the single-impurity Green's functions. The self-consistent DMFT equations are solved by following the steps below:

1. Choose initial self-energy $\Sigma(\omega)$.

2. Calculate local Green's function using Equation (56).
3. Calculate Dynamical mean field $\mathcal{G}(\omega)$ using Equation (59).
4. Find new Green's function using the quantum impurity problem

$$G_{\sigma l; \sigma' m}(\omega) = \int D[\psi] D[\psi^*] \psi_{\sigma l} \psi_{\sigma' m}^* e^{-A_{eff}[\psi, \psi^*, \mathcal{G}^{-1}]} \quad (60)$$

$$A_{eff}[\psi, \psi^*, \mathcal{G}^{-1}] = - \int_0^\beta d\tau \int_0^\beta d\tau' \sum_\sigma \psi_{0\sigma}^*(\tau) \mathcal{G}^{-1}(\tau - \tau') \psi_{0\sigma}(\tau') + U \int_0^\beta d\tau n_{0\uparrow}(\tau) n_{0\downarrow}(\tau) \quad (61)$$

5. Find new self-energy from equation (59).
6. Continue till $\Sigma(\omega)$ converges.

The most difficult part of this scheme is to solve equation (60). One can follow exact numerical methods like Quantum Monte Carlo (QMC) (e.g., Hirsh-Fye or continuous-time QMC approaches), or analytical methods like the iterative perturbation theory expansion to solve that part.

2.3 Time-Dependent Density-Functional Theory

DFT is a ground-state theory, so it cannot be used to calculate the excitation energies or other excited-state properties. Time-Dependent Density Functional Theory (TDDFT) extends the basic idea of DFT to deal with time-dependent external perturbations and calculate the excitation energies or more general time-dependent phenomenon. In TDDFT, similar to DFT, the basic variable is $n(\mathbf{r}, t)$ and the simplest way to determine

the density is using the fictitious system of non-interacting electrons, i.e. solving the time-dependent Kohn –Sham equations. This is very general scheme and can be applied to any time-dependent situation. If the external time -dependent potential is weak, one can use the linear-response theory to calculate the optical absorption spectra and other properties of the system. On the other hand, if the time-dependent potential is strong one has to solve the KS equations exactly. The rigorous mathematical foundation of TDDFT was done by Runge and Gross³⁷ by formulation of the Runge-Gross theorem, which is an extension of the Hohenberg-Kohn theorem. It states that: “For any system of interacting electrons evolving from the same wavefunction there is one to one mapping between the time-dependent external potential and the time-dependent electron density”. The difference is that unlike DFT, TDDFT depends on the initial conditions; this is because the time-dependent Schrodinger equation is the first order differential equation in time. Another difference is that in the static case the ground state of the system can be determined through the minimization of the total energy functional, but in the time-dependent case the total energy is not a conserved quantity. The time-dependent counterpart of the energy is the action:

$$A = \int_{t_0}^{t_1} \left\langle \Psi(t) \left| i \frac{\partial}{\partial t} - \hat{H}(t) \right| \Psi(t) \right\rangle \quad (62)$$

A can be expressed as a functional of the density:

$$A[n] = S[n] - \int_{t_0}^{t_1} \int n(r, t) v_{ext}(r, t) dt dr, \quad (63)$$

where $S[n]$ is a universal functional of the time-dependent density (namely, it does not depend on the external potential). The functional $A[n]$ has minimum in the case of the exact density of the system. Equation (63) is in agreement with the exact solution of the many-body time-dependent Schrödinger equation, in other words the functional $S[n]$ is stationary for the exact time-dependent density:

$$A[n] = S_0[n] + S_H[n] + S_{xc}[n] - \int_{t_0}^{t_1} \int n(r, t) v_{ext}(r, t) dt dr, \quad (64)$$

where $S_0[n]$ is the functional for non-interacting electrons,

$$S_H[n] = -\frac{1}{2} \int_{t_0}^{t_1} \int \int \frac{n(r, t) n(r', t)}{|r - r'|} dt dr dr', \quad (65)$$

and S_{xc} includes all many-body effects. The stationary action principle leads to the Euler equation of non-interacting electrons moving in some time-dependent effective potential $v_{KS}(r, t)$:

$$\frac{\delta S_0[n]}{\delta n(r, t)} - v_{KS}(r, t) = 0, \quad (66)$$

$$v_{KS}(r, t) = v_{ext}(r, t) + v_H[n](r, t) + v_{xc}[n](r, t), \quad (67)$$

or

$$v_{KS}(r, t) = v_{ext}(r, t) + \int dr' \frac{n(r', t)}{|r - r'|} - \frac{\delta A_{xc}[n]}{\delta n(r, t)}, \quad (68)$$

which gives

$$\frac{\partial}{\partial t} \phi_i(r, t) = \left[-\frac{\hbar^2}{2m} \nabla^2 + v_{KS}(r, t) \right] \phi_i(r, t), \quad (69)$$

$$n(r, t) = \sum_{i=1}^N \phi_i^*(r, t) \phi_i(r, t). \quad (70)$$

Similar to static DFT density, the time-dependent density is calculated by solving the one-particle time-dependent equation called the time-dependent Kohn-Sham (TDKS) equation. The total density is the sum over all occupied orbitals ϕ_i , Equation (70). Once again, the accuracy of the results depends on the approximation for the XC potential.

2.3.1 Adiabatic Approximation

The simplest TDDFT approximation is adiabatic LDA, which is an extension of the static LDA. In general case, the exact XC potential depends non-locally on the density both for the spatial and time variables (memory effects). The adiabatic approximation assumes neglecting the memory effects, i.e. the XC potential at given time depends on the density at the same moment of time. The general form of adiabatic XC potential can be obtained as

$$v_{xc}^{adia}[n](r, t) = v_{xc}^{GS}[n](r, t), \quad (71)$$

where v_{xc}^{GS} is the density dependent ground-state (DFT) XC functional, calculated for time-dependent (instantaneous) density, $n(r, t)$. Although, it seems like a dramatic approximation it works well in many cases, especially when the perturbation is weak

and/or slow. Each ground-state functional such as LDA, GGA or hybrid one can be used for the adiabatic TDDFT approximation.

2.3.2 Linear Response Theory

In majority of cases, when the external time-dependent potential is small, perturbation theory can be applied to calculate the absorption spectra and other properties. One of the main applications of TDDFT is the calculation of the optical absorption spectra in the linear-response regime, using the dipole approximation, where works remarkably well. We will be working in the frequency domain, by using Fourier transformation of time-dependent quantities. For given many-body system, the linear response theory can be applied to study the variation of a given physical observable (like density) due to the application of a weak external perturbation. Let us assume that for time $t < t_0$ the system is in its ground-state with external (nuclei) potential v_0 and ground-state density n_0 . At t_0 a weak perturbation v'_{ext} is applied, so that the total external potential becomes

$$v_{ext} = v_0 + v'_{ext}. \quad (72)$$

The applied perturbation will induce charge density evolution. Since the perturbation is slow, the density can be expanded in series:

$$n(r, t) = n_0(r) + n'(r, t) + n''(r, t) + \dots \quad (73)$$

Here, $n'(r, t)$ depends linearly on v'_{ext} , $n''(r, t)$ depends quadratically on v'_{ext} and so on.

Because the perturbation is small, we are interested only in the linear part $n'(r, t)$,

which in the frequency domain can be written as:

$$n'(r, \omega) = \int \chi(r, r', \omega) v'_{ext}(r', \omega) dr'. \quad (74)$$

The generalized susceptibility $\chi(r, r', \omega)$ is a fundamental quantity in TDDFT. It is also known as the density-density response function, which can be calculated as

$$\chi(r, r', \omega) = \sum_n \left[\frac{\langle \Psi_0 | \hat{\psi}^\dagger(r) \hat{\psi}(r) | \Psi_n \rangle \langle \Psi_n | \hat{\psi}^\dagger(r') \hat{\psi}(r') | \Psi_0 \rangle}{\omega - (E_n - E_0) + i\eta} - \frac{\langle \Psi_0 | \hat{\psi}^\dagger(r') \hat{\psi}(r') | \Psi_n \rangle \langle \Psi_n | \hat{\psi}^\dagger(r) \hat{\psi}(r) | \Psi_0 \rangle}{\omega + (E_n - E_0) + i\eta} \right], \quad (75)$$

where η is an infinitesimal positive number, Ψ_0 and Ψ_n are the ground state and excited-state wave functions, corresponding to the energies E_0 and E_n , and $\hat{\psi}^\dagger(r)$ and $\hat{\psi}(r)$ are the field operators. The operator $\hat{\psi}^\dagger(r) \hat{\psi}(r)$ is the secondary-quantized density operator with the eigenvalues

$$\hat{n}(r) = \sum_{i=1}^N \delta(r - r_i), \quad (76)$$

where N is the total number of electrons in the system. The poles of Equation (75) give the excitation energies of the system. In the case of an independent particle system with single-particle orbitals $\phi_i(r)$ and energies ϵ_i , Ψ_0 and Ψ_n are the Slater determinants and Equation (75) can be written as

$$\chi(r, r', \omega) = \sum_{ij} (n_j - n_i) \frac{\phi_j^*(r) \phi_i(r) \phi_i^*(r') \phi_j(r')}{\epsilon_j - \epsilon_i + \omega + i\eta}, \quad (77)$$

where n_j and n_i are the occupation numbers. Obviously, the response function for the non-interacting system is much easier to calculate than the interacting one. From the

response function we also find many important quantities, like polarizability of the system:

$$\alpha_{ij}(\omega) = \int r_i \chi(r, r', \omega) r_j' dr dr'. \quad (78)$$

In case of an homogeneous external electric field $\mathbf{E}(\omega)$, the external potential is given by

$$V_{ext}(r', \omega) = -\mathbf{E}(\omega) \cdot \mathbf{r} \quad (79)$$

(dipole approximation), and

$$\alpha_{ij}(\omega) = \frac{d_i'(\omega)}{E_j(\omega)}, \quad (80)$$

where $d_i'(\omega)$ is the dipole moment, i.e. polarizability is the response tensor of the dipole to an external electric field. In the case of non-polarized radiation, the mean polarizability is

$$\bar{\alpha}(\omega) = \frac{1}{3} Tr \alpha(\omega) = \sum_n \frac{f_n}{(E_n - E_0)^2 - \omega^2}, \quad (81)$$

where

$$f_n = \frac{2}{3} (E_n - E_0) (|\langle \Psi_0 | \hat{x} | \Psi_n \rangle|^2 + |\langle \Psi_0 | \hat{y} | \Psi_n \rangle|^2 + |\langle \Psi_0 | \hat{z} | \Psi_n \rangle|^2) \quad (82)$$

is the oscillator strength for the excitation energy $E_n - E_0$. Most molecules are bound excited electronic states in addition to the ground electronic state E_0 . These states arise when an electron from the occupied orbital in the ground state jumps to a vacant higher energy orbital and this excitation of an electron occurs when the absorbed photon has

the energy that matches the energy difference between the two states. The classical Franck-Condon principle states that because the rearrangement of electrons is much faster than the motion of nuclei, the nuclear configuration does not change significantly during the energy absorption process. Thus, the absorption spectrum of molecules is usually calculated at fixed ion positions. In the extended case, since the photon momentum can be usually neglected (it is much smaller than the Fermi momentum), usually the vertical transitions (with fixed momentum) are considered.

The evaluation of the response function for interacting system is a complicated problem. We recall that in the TDKS framework, the density of the interacting system of electrons is obtained from a fictitious system of non-interacting electrons. So, we can also calculate the linear change of density due to the external perturbation using the KS formalism. In this case, the density can be written as:

$$n'(r, \omega) = \int \chi_{KS}(r, r', \omega) v'_{KS}(r', \omega) d r', \quad (83)$$

where

$$v'_{KS}(r', \omega) = v'_{ext}(r', \omega) + v'_H(r', \omega) + v'_{xc}(r', \omega), \quad (84)$$

and

$$\chi_{KS}(r, r', \omega) = \sum_{ij} (n_j - n_i) \frac{\phi_j^*(r) \phi_i(r) \phi_i^*(r') \phi_j(r')}{\epsilon_j - \epsilon_i + \omega + i\eta} \quad (85)$$

Corresponds to the non-interacting KS electrons. n_i, n_j are the occupations of the ground state orbitals ϕ_i, ϕ_j .

The KS potential v'_{KS} , depends on the density and controls the external perturbation. It consists of the external potential v'_{ext} and the Hartree and the XC parts:

$$v'_{Hxc}(r, \omega) = v'_H(r', \omega) + v'_{xc}(r', \omega) = \int \kappa(r, r', \omega) n'(r', \omega) dr', \quad (86)$$

$$\kappa(r, r', \omega) = \frac{1}{|r-r'|} + \left. \frac{\delta v_{exc}(r, \omega)}{\delta n(r, \omega)} \right|_{n=n_0}. \quad (87)$$

The kernel $\kappa(r, r', \omega)$ has contributions from both the Hartree and the XC parts. The second term in Equation (87) is the XC kernel f_{xc} and that depends on the charge density. In the adiabatic approximation, the frequency dependence vanishes and the kernel depends on the ground state density:

$$f_{xc}^{adia}(r, r', t - t') = \left. \frac{\delta v_{exc}(r)}{\delta n(r')} \right|_{n=n_0} \delta(t - t'). \quad (88)$$

Using Equations (83), (84) and (86), we obtain the linear response function:

$$\chi(r, r', \omega) = \chi_{KS}(r, r', \omega) + \iint \chi_{KS}(r, r_1, \omega) \kappa(r_1, r_2, \omega) \chi(r_2, r', \omega) dr_1 dr_2 \quad (89)$$

As mentioned before, the poles of this function give the excitation energies and the residues give the corresponding oscillator strengths of the interacting system. Formally, Equation (89) is the exact representation of the linear response function, if we know exact χ_{KS} . The self-consistent solution of the above equation gives the susceptibility of the interacting system. The f_{xc} term contains the corrections to the non-interacting Kohn-Sham susceptibility and includes all the many-body effects in it. This is a very complex quantity difficult to find exactly, and many approximations have been used for it. The

simplest one is the Adiabatic LDA (ALDA), which is local in both space and time, and uses the XC potential of the homogeneous electron gas:

$$f_{xc}^{ALDA}(rt, r't') = \delta(r - r')\delta(t - t')f_{xc}^{HEG}(n)|_{n=n(r,t)}, \quad (90)$$

where

$$f_{xc}^{HEG}(n) = \frac{d}{dn}v_{xc}^{HEG}(n). \quad (91)$$

ALDA approximation in spite of being very simple works well for many systems, especially in the low frequency regime. Another type XC kernel is PGG kernel derived by Petresilka et al. in 1996:

$$f_x^{PGG}(rt, r't') = -\delta(t - t') \frac{1}{2} \frac{1}{|r - r'|} \frac{|\sum_k^{occ} \varphi_k(r) \varphi_k^*(r')|^2}{n(r)n(r')}, \quad (92)$$

The solution of Equation (89) is computationally expensive and also requires a huge amount of memory. The calculation of the empty states of the ground-state KS Hamiltonian scales as the third power of the dimension of the basis set. If one uses small number of states, then he is restricted to the low-energy range. Also, constructing the susceptibility χ_{KS} in real or reciprocal space requires a computational effort of the order of $N_v N_c N_{grid}^2$, where, N_v and N_c are the number of valence and conduction bands and N_{grid} is the dimension of the grid. The memory requirement is of the order of N_{grid}^2 and solving the matrix inversion and multiplications costs are proportional to N_{grid}^3 . Furthermore, the calculation has to be done for many frequencies, making them very tedious and expensive. Therefore, there is a need in more efficient technique.

2.3.3 Casida Equations

The Casida equations³⁸ used the eigenvalue problem to calculate the excitation energies of the system. This approach is mostly used in quantum chemistry and condensed matter physics community and is also implemented in many ab initio codes. For any TDDFT Casida analysis, the first step is calculation of the electronic excitation energies from usual DFT calculations, with a chosen XC functional. The difference between the occupied and unoccupied Kohn-Sham DFT electronic energies resembles excitation energies and this difference is the starting point of the Casida approach. The charge density is obtained by substituting Equation (85) in Equation (83):

$$n'(r, \omega) = \sum_{ij} P'_{ij} \phi_j^*(r) \phi_i(r), \quad (93)$$

where the expansion coefficients are given by

$$P'_{ij}(\omega) = \frac{n_j - n_i}{\varepsilon_j - \varepsilon_i + \omega + i\eta} \int \phi_i^*(r) v'_{KS}(r, \omega) \phi_j(r) dr. \quad (94)$$

These coefficients are equal to zero if the virtual states are not the same as the occupied states. Now, substituting n' into Equation (74) one gets

$$\sum_{kl} \left[\frac{\omega - (\varepsilon_k - \varepsilon_l)}{n_j - n_i} \delta_{ik} \delta_{jl} - \mathcal{K}_{ij,kl} \right] P'_{kl}(\omega) = \int \phi_i^*(r) v'_{ext}(r, \omega) \phi_j(r) dr, \quad (95)$$

where

$$\mathcal{K}_{ij,kl}(\omega) = \iint \phi_i^*(r) \phi_j(r) \kappa(r, r', \omega) \phi_k^*(r') \phi_l(r') \quad (96)$$

is the coupling matrix that depends on the XC kernel. Equation (95) can be reduced to the Casida eigenenergy equations (by setting $v'_{ext} = 0$):

$$\hat{\Omega}F_I = \omega_I^2 F_I,$$

where (97)

$$\Omega_{ij,kl} = (\varepsilon_l - \varepsilon_k)^2 \delta_{ik} \delta_{jl} + 2\sqrt{(n_i - n_j)(\varepsilon_j - \varepsilon_i)} \mathcal{K}_{ij,kl} \sqrt{(n_k - n_l)(\varepsilon_l - \varepsilon_k)} \quad (98)$$

is a Hermitian matrix. The eigenvalues of Equation (97) are the excitation energies and the eigenvectors define the spectroscopic oscillator strengths. The diagonal part of a matrix (first term) gives the square of the Kohn-Sham DFT excitation energies. The off-diagonal part is the coupling matrix that on addition to the diagonal part corrects the Kohn-Sham energies. The XC kernel contribution is different for the spin-singlet and in the spin-triplet states.

The Casida formalism allows us to calculate oscillator strengths which are needed to obtain the frequency-dependent polarizability, and the corresponding optical spectrum. The oscillator strengths are given as a second-rank tensor, in the Cartesian coordinates. After obtaining the energy levels E_i and the transition dipole moments $\langle i|D|j\rangle$, one can calculate the absorption spectrum using the standard expression

$$A(\omega) = \sum_{i \neq j} (E_i - E_j) |\langle i|D|j\rangle|^2 e^{-|E_i - E_j - \omega|/\Gamma}, \quad (99)$$

where ω is the frequency and Γ is the peak broadening.

The Casida equations are computationally less expensive owing to the iterative methods that do not require explicit calculation and storage of the complete matrix. But, this iterative method restricts the calculations to only lowest eigenvalues, which is not suitable for very large systems. In order to solve Casida equation the first step is to calculate the empty Kohn Sham states, which is done by diagonalizing the Hamiltonian and this diagonalization becomes very expensive when the basis set is large. Also when the size of the system increases the density of transitions in the given energy range increases as well. Real time propagation TDDFT approach helps deal with these problems. It can handle large systems and also takes in account the non-linear effects. The computational cost is more but it is favorable approach for large systems. For this thesis we will be focusing on small chains so we will restrict to Casida formalism.

CHAPTER 3 OPTICAL PROPERTIES OF NANOCHAINS

3.1 Plasmonic Effects

3.1.1 Plasmons

Plasma oscillations in a metal is a collective excitation of electrons in a fixed positive background. Collective excitations involve a significant number of particles in the system, that move in a synchronized way. These excitations can be very unusual and have very useful characteristics for applications. The nature of these oscillations can be understood in terms of a very simple model. One can imagine them as displacement of the entire electron gas as a whole through some distance d with respect to the fixed positive background of ions (Fig.1).

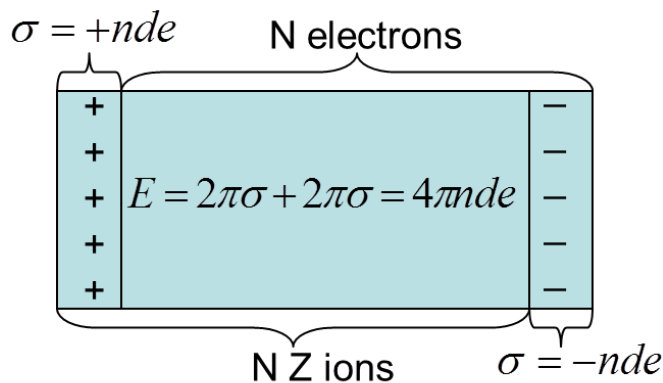


Figure 1. Electron gas model to describe the charge oscillation.

The resulting surface charge σ will give rise to an electric field of magnitude $4\pi\sigma$ in the slab (see Fig.1 for details). Consequently, the electron gas will obey the equation of motion:

$$Nm\ddot{d} = -Ne|4\pi\sigma| = -Ne(4\pi nde), \quad (100)$$

$$Nm\ddot{d} = -4\pi ne^2 Nd, \quad (101)$$

where d is the dipole moment. Equation (101) is nothing but the harmonic oscillator equation with the frequency known as the plasmon frequency

$$\omega_p^2 = \frac{4\pi ne^2}{m}. \quad (102)$$

The last result is valid for the bulk system. For the surfaces the plasmon frequency is related to the bulk frequency as $\omega_s = \frac{\omega_b}{\sqrt{2}}$.calculated from Maxwell's equations. The dispersion relation of wave propagating on surface is given by $k_x = \frac{\omega}{c} \left(\frac{\epsilon_1 \epsilon_2}{\epsilon_1 + \epsilon_2} \right)^{1/2}$ and in the free electron gas model the dielectric function is given as $(\omega) = 1 - \frac{\omega_p^2}{\omega^2}$. The surface plasmon frequency is the asymptotic curve given by $\omega_s = \omega_p / \sqrt{1 + \epsilon_2}$ and for air it reduces to $\omega_p / \sqrt{2}$. In the case of nanoparticles, there is no general formula for the plasmon frequencies. If the diameter of a nanoparticle is of the order of the penetration depth of electromagnetic waves in metals, the excitation light is able to penetrate through the particle. This electromagnetic wave, when enters inside the metal, it causes conduction electrons to shift with respect to positive ions. As the electrons moves to one side they build up a charge on the surface of the particle on that side. The attraction between the negative charge of electrons and the positive charge of the ions on the opposite side results in a restoring force. The alternating surface charges correspond to

dipole oscillations, which can lead to an electromagnetic emission. If the frequency of the excitation source is in resonance with the eigen frequency of this collective oscillation, the resulting oscillation can be rather strong even for small exciting field. The oscillations also depend on the damping, which can be both radiative and non-radiative. The value of the resonance frequency depends on the strength of the restoring force which depends on the separation of the surface charges, the particle size, and the polarizability of the medium. For particles larger than 10nm classical Mie's theory can be applied to calculate the absorption spectrum. Mie³⁹ presented a solution to Maxwell's equations that describes the extinction spectra (extinction = scattering + absorption) of spherical particles of arbitrary size. He found that for spherical particles, as long as their diameter is much smaller than the wavelength of incident radiation, there is a single resonance frequency that is independent of the particle diameter. The absorption spectrum is more complex if the particle is not spherical, and one needs to take into account quantum effects for smaller particles. Therefore, for smaller nanoparticles one needs to use quantum approaches, like TDDFT. It was shown by Kummel et al.⁴⁰, who applied both TDDFT and quantum fluid dynamics methods in the local current approximation (LCA) to small Na atom clusters, that collective oscillations exist even for very small clusters of two atoms.

In our studies, we focused on the plasmons in linear chains of atoms. Analytically, we can estimate the plasmon frequency of the chain from Eq. (102) by assuming the chain to be a tube of some radius r and length l given in Eq. (103)

$$l = ((N_{atoms} - 1)d + 2r) \quad (103)$$



Figure 2. Schematic representation of plasmons in chains.

We estimate the radius of the tube as such that it contains 90% of the orbital electronic charge. For example, in the case of the 6s orbitals for Au, r is equal to 21.07\AA . So we get the plasmon energy:

$$\hbar\omega = \sqrt{4\pi n \frac{\hbar^2 e^2}{m_e} \frac{m_e}{m}}, \quad (104)$$

where n is the density given as $n = N/V$ and the volume of the tube is $V = \pi r^2 l$.

Substitution of the expressions above into Equation (104) gives:

$$\hbar\omega = 20.95 \sqrt{\frac{N}{((N_{atoms}-1)d + 2r)r^2} \frac{m_e}{m}} \text{ eV}. \quad (105)$$

This expression gives qualitatively correct value for the plasmon absorption energy and this is justified by our studies also as presented in section 3.1.b below.

3.1.2 Single pure and doped Au chains

The characteristics of monoatomic nanostructures and bimetallic nanostructures consisting of a noble and transition metal (TM) atoms is an active area of both experimental and theoretical study. One of the main reasons for this is that bulk noble metals such as Au and Ag and their extended layered structures display plasmon excitations in the visible frequency range which may be further tuned by changing either the geometry or chemical composition via doping with TM atoms. Since the TM atoms have both extended s and localized d states, one may expect interesting and unusual interplay of the role of these two types of states in determining the properties of noble metal-TM systems, particularly at the nanoscale. Collective excitations in few-atom clusters shown initially by Kummel et al.⁴¹ have been the subject of several theoretical investigations following recent scanning tunneling microscope observations showing development of 1D band structure when the number of atoms in Au chains on NiAl(110) exceeds 10^{20} . Subsequent theoretical calculations at the same time confirmed the presence of the collective plasmon mode for Na^{42, 43}, Ag^{44, 45}, and Au^{46, 47} chains containing more than 10 atoms. Experimental observation of such collective excitations requires the chains to be grown on a substrate that does not quench them rapidly. While there are theoretical indications that NiAl(110) surface does not affect the electronic properties of the Au chains⁴⁸ its metallic nature precludes a short lifetime for any plasmon excitation. On the other hand, it is possible to grow Au chains and wires on semiconductor substrates such as Si (557)^{49, 50}, Ge(001)⁵¹ and quartz⁵² which may be amenable for capturing the plasmon effects (especially with the bandgap much larger

than the chain plasmon and other excitation energies of interest). In principle, one may expect a significant change of the interatomic distances when the chains are put on the substrate. However, as our calculations demonstrate, the qualitative results remain qualitatively and semi-quantitatively the same when the bond lengths change (in a reasonable, ~ 0.01 - 0.1 nm, interval). The experimental study of TM (Pd) doped small Au chains on NiAl(110)⁵³ found local electronic resonances around the dopant atom. As for optical properties of TM doped noble metal chains, we are not aware of any previous study. Here I present results of theoretical calculations of the optical properties of Au chains and doped chains, $\text{Au}_{n-m}\text{X}_m$, consisting of $n = 2$ to 24 atoms. In the doped case, we consider weakly-doped chains with different TM atoms ($\text{X} = \text{Ni}, \text{Rh}$ and Fe , $m = 1$ - 4)

3.1.2.1 Computational Details

We have applied the TDDFT approach as employed in the Gaussian 03⁵⁴ code with a B3PW91³¹ hybrid functional and a LanL2DZ basis set⁵⁵. We have considered $\text{Au}_{n-m}\text{X}_m$ chains of length up to $n=24$ atoms, in which $\text{X}=\text{Ni}, \text{Rh}$ or Fe , with m ranging between 1 and 4 (though in most cases $m=1$). For pure Au chains, our results are in a good agreement with those of other TDDFT calculations⁴⁶. Calculations of optimized Au-Au bond lengths show that the optical absorption spectrum does not significantly depend on the interatomic distances. Ab-initio calculations show that NiAl (110) surface acts mostly as a structural template for Au chains and do not affect the electronic properties of the chains. Therefore, as a first approximation we do not take into account the chain

substrate interaction to study the plasmon excitations, we only set the interatomic distance d to 2.89\AA , corresponding to that observed experimentally for Au chains on NiAl (110) substrate²⁰. For doped chains, we optimized the bond lengths in Au-X dimer and Au-X-Au trimer. Since our interest is mainly in the visible spectrum and since the computational time for a given number of excited states increases dramatically with increasing chain size, we have focused our attention on states below 5eV, also since the visible range is the most interesting from solar energy application point of view.. This choice allowed us to study the longitudinal plasmon modes in all cases, but not the high-energy (ultra-violet) transverse plasmon modes, found for example in Au chains⁴⁶. In order to make the figures more transparent, in plotting $A(\omega)$ we neglected the contribution of dipole moments less than 0.1 in atomic units as it is very small as compared to the main plasmon peak.

3.1.2.2 Results

Fig.3 confirms the finding of Lian et.al.⁴⁶, that a new (collective) longitudinal plasmonic mode emerges in the optical absorption spectrum when the number of atoms in the even numbered chains is of order 6. The position of the peaks moves into the infrared region with increasing n and becomes close to the asymptotic value $\sim 0.6\text{eV}$ when $n=20$.

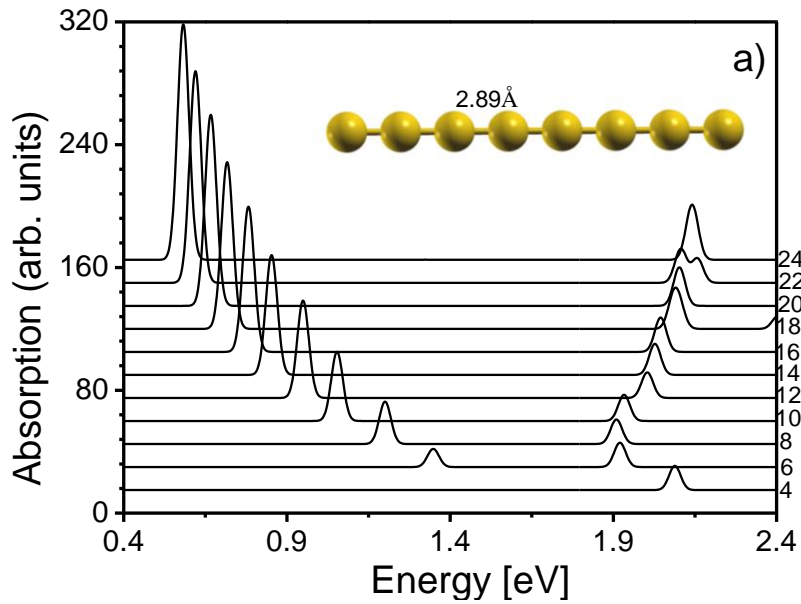


Figure 3 The optical absorption spectrum of the Au_n ($n=4-24$) from bottom to top.

Since the magnitude of the peak grows with n , this excitation becomes dominating as the number of electrons involved in the collective motion also increases with n . The redshift of the plasmon energy with increasing n is related to the reduction in the energy gap (the bandgap in the many-atom case) involved in the dipole excitation (see also Ref.⁴⁶).

The high energy peaks survive as n decreases. They correspond to the atomic/molecular level transitions. Interestingly, we have found for pure gold chains with an odd number of atoms a smaller satellite peak with the energy ~ 0.1 below the main peak, which might be attributed to additional oscillations related to the unbonded extra

charge from the "odd" atom at the edge. However, in this study we focus on examining chains with even number of atoms, and don't analyze the nature of such peaks in detail.

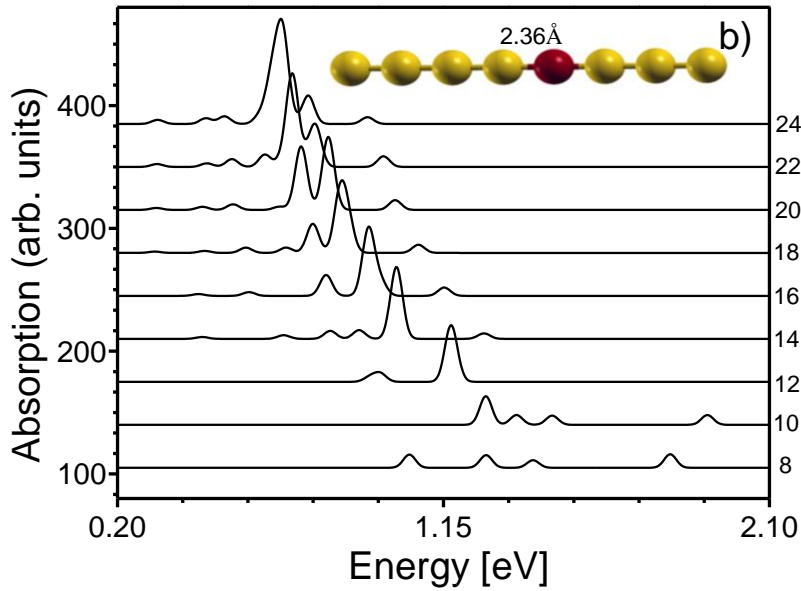


Figure 4 The optical absorption spectrum for $Au_{n-1}Ni$ ($n=8-24$). The local plasmon peak emerges at the left of the main peak at $n=12$ and changes its relative position at $n>20$

As for the doped chains, we consider first those of length $n=2$ to 24, doped with only one TM atom $X=Ni, Rh$ and Fe . We find that when $X= Ni$, there is an additional plasmon peak close in energy to that of the main peak (Fig. 4). Since this additional peak does not exist in the case of short chains ($n<12$), it must also have a collective nature. The fact that this peak appears when the Au chain is doped with one atom and that its position is independent of the position of the doping atom in the chain (except when it is very close to the chain edge) suggests that it must have a localized nature (see the next

subsection). The localized plasmon mode appears also when the doping atom is Fe, but Rh. Note that the highest occupied s-orbital of an Rh atom contains only one electron, as does that of Au, while in Ni and Fe this orbital is doubly occupied. The presence of the extra peak may be closely related to the charge redistribution in the doped chains, which is expected to be much larger in those containing Ni or Fe atoms with unfilled d orbitals, while in Rh-doped chains, the d-levels are filled (see below). This explanation is supported by our calculations for chains in which the dopant is an Ag atom (for which the s-state is likewise singly-occupied): as in the Rh case, no new plasmon peak appears.

A closer look at those plasmonic modes in the Ni doped case reveals that a redistribution of the oscillation strength takes place: what is the dominant mode at $n=18$ turns at $n=24$ into a secondary mode. In between at $n=20$ the plasmon modes are of almost equal strength. A plausible explanation for this is that when a Ni atom sits in the middle of this chain, we have what amounts to two separated gold chains, each of a size close to the critical value (10) at which the collective extended plasmonic mode appears, and one may assume that these two chains generate strong coherent oscillations, raising the strength of the lower mode to a level close to that of the dominant. The magnitude of the lower peak increases as n increases further. The second mode can be attributed to the local plasmon, with higher energy comparable to that of the collective plasmon at $n>20$. The reason for this is that the attractive positive background potential is stronger for the local mode than that for the collective mode.

The position of the local peak depends much less on the chain length than does the collective plasmon because number of electrons involved in the local plasmon oscillations will not increase with the entire chain length increasing. The size of the chain area involved in local oscillations depends on the impurity potential.

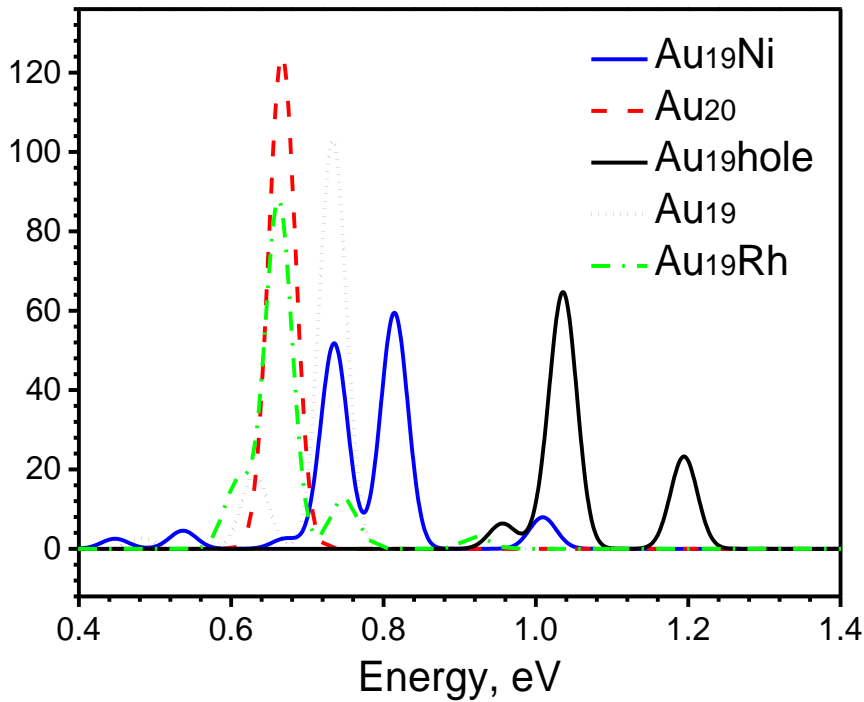


Figure 5 The optical absorption spectrum of Au₂₀, Au₁₉, Au₁₉Ni, Au₁₉Rh, Au₁₉.hole

The origin of the extra peak is further analyzed in Fig. 5 which compares the absorption spectrum of the Au₁₉Ni and Au₁₉Rh chains with those of Au₂₀, Au₁₉, and Au₁₉ with a hole in the middle. One of the peaks for Au₁₉Ni coincides with that of Au₁₉ reflecting that it is indeed the collective excitation of the 19 Au atoms in the chain while the other is

inherently linked to the presence of the Ni atom. The absorption spectrum of the Au_{19}Rh chain in Fig.5 asserts that its optical properties are similar to the Au_{20} chain with a small lower energy peak revealing the effect of the dopant. On the other hand, a hole in the Au_{19} chain breaks the response into that for a 10-atom and 9-atom chain.

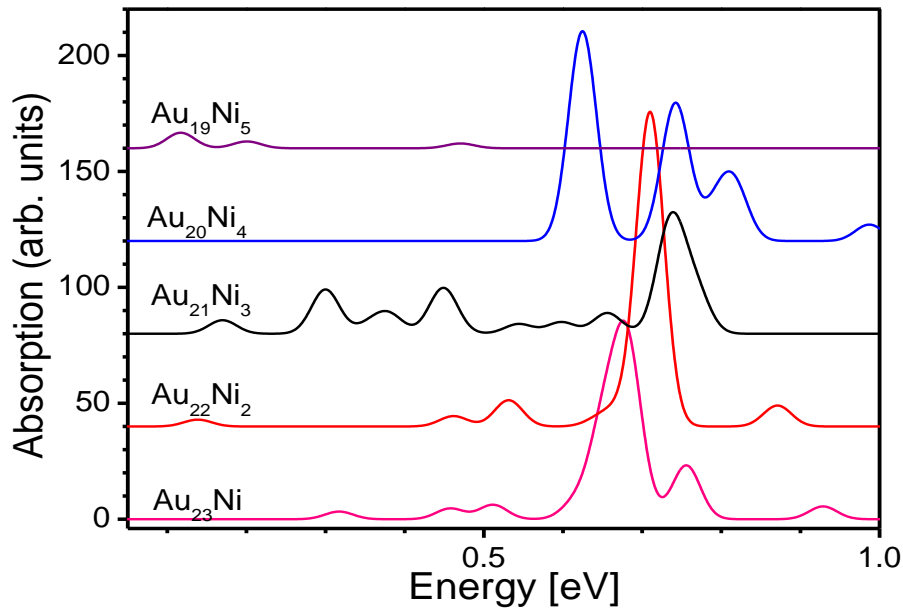


Figure 6 The optical absorption spectrum of the $\text{Au}_{24-n}\text{Ni}_n$ ($n = 1, 2, 3, 4, 5$) chains.

We have found that the plasmonic peaks in the optical absorption spectrum disappear when the number of dopant atoms is around 5. The results for the case of quasi-equidistant Ni impurities far from the edges in the 24-atom Au chain are presented in Fig.6. Indeed, in the case of 5 impurities, consisting of five 3-atom and one 4-atom Au chains separated by the TM atoms, the constituent chains are too short to excite either

collective or local plasmons (see Fig.3). Similar results emerged when the 5 Ni atoms situated directly next to each other (“clubbed together,” as it were). In the case of weakly-doped $\text{Au}_{18}\text{Ni}_2$ chain, there are two plasmon peaks in both the separated and the clubbed Ni atom cases, about 0.1eV, though the center of the peak positions is different in the two cases. This result also suggests that there are two kinds of excitations in the system: collective motion in subchains and some local- charge oscillations near the Au-Ni border.

3.1.2.3 Discussion

Casida formalism allows us to look at the energy ranges for longitudinal oscillations only and that is where the focus of our calculations is. The main objective of this study is to see how doping affects the plasmon resonance in small chains. The effect is different for larger nanoparticles where Au and Ni when mixed together destroys the plasmon peak⁵⁶. But in small chains with just one atom one can get new modes in the absorption spectrum and also larger absorption band (in the case of double doped chains: see next section). These calculations are all electron calculations and so all the orbitals are taken into account making the basis set even larger. This restricts us to lower energy values for larger systems. One can use frozen core approach to look at larger energies or transverse oscillations⁴⁶. But for this thesis we will focus just on the longitudinal oscillations. In this discussion we have used various analytical approaches to understand the nature as well as origin of excitation peaks that we see in the absorption

spectrum. All the given approaches suggest that the collective oscillations exist in pure chains and additional peak arise because of the potential well generated by impurity potential. With these approaches we explain different results, for example, to understand the nature of oscillations involved in particular excitation, one dimensional electron gas model is used and to understand the reason for additional peak, impurity model using tight binding Hamiltonian is used. The Mulliken charge analysis suggest the reason so as to why the additional mode in Rh is weak as compared to Ni and the analytical plasmon frequency is calculated by deriving a simple formula from the bulk plasmon frequency which can be further refined to use for multiple chains (see next section). Although these different calculations agree qualitatively with the TDDFT calculations, the latter are important because there we have used all electron calculations which make them more accurate while in all other analytical approaches only valence electrons and orbitals are considered. One dimensional gas model cannot be used to explain the new peaks generated because of doping. Also the formula to calculate the plasmon frequency is only for pure chains and cannot give the frequency for the additional mode because there we have considered the oscillations over the entire chain. So even when each model has its own restrictions combining various approaches strengthen the idea of local and collective oscillations observed with TDDFT calculations. Below we discuss each of the analytical approaches in detail.

To understand qualitatively the nature of the excitations in the chains under study, we used a simple model of quasi-one-dimensional electron gas as proposed by Gao et al.,³⁸ and motivated by recent calculations which show the presence also of quadrupole excitations in confined one dimensional systems⁵⁷. The ground state of the electron gas is described by standing electron waves confined between the infinite walls at both ends:

$$\psi_n(\rho, x) = \sqrt{\frac{2}{L}} \sin \frac{n\pi x}{L} \varphi(\rho) \quad (106)$$

with

$$\varphi(\rho) = \frac{1}{\sqrt{2\pi b^2}} e^{-\frac{\rho^2}{4b^2}} \quad (107)$$

being the transverse wave function, ρ is the radial coordinate perpendicular to the chain. The quasi-one-dimensional electron gas system has length L and the transverse radius $2b$. The response function of interacting electron gas is calculated from the free response function and electron-electron interaction kernel K :

$$\Pi_0^R(x, x', \omega) = \sum_{k, k'} \frac{f_k(1-f_{k'})}{\omega - \epsilon_{k'} + \epsilon_k} \psi_k(x)^* \times \psi_k(x') \psi_{k'}(x')^* \psi_{k'}(x) \quad (108)$$

$$\Pi^R(x, x', \omega) = \Pi_0^R(x, x', \omega) + \int dx_1 \int dx_2 \Pi_0^R(x, x_1, \omega) \times K(x_1, x_2) \Pi^R(x_2, x', \omega), \quad (109)$$

where $(x_1, x_2) = v(x_1, x_2)$, the reduced Coulomb interaction given by

$$v(x_1, x_2) = \int \rho_1 d\rho_1 \int \rho_2 d\rho_2 \int \frac{d\phi}{2\pi} \times \frac{\phi^2(\rho_1) \phi^2(\rho_2)}{\sqrt{(\rho_1^2 + \rho_2^2 - 2\rho_1 \rho_2 \cos \phi) + (x_1 - x_2)^2}}. \quad (110)$$

From the response function, in turn, one can calculate both the dipole strength function

$$S(\omega) = \frac{2m}{\pi} \omega \text{Im}\alpha(\omega), \quad (111)$$

$$\alpha(\omega) = - \int dx \int dx' x \Pi^R(x, x', \omega) x' \quad (112)$$

and the induced charge density

$$\delta n(x, \omega) = - \int dx' x' \Pi^R(x, x', \omega). \quad (113)$$

From the above equations we calculate the absorption spectra for pure and doped 10-atom chains. As shown in Fig. 7, the spectrum of the doped chain has more peaks than that of the pure 10-atom chain. The nature of excitations can be qualitatively understood from the induced charge-density plots shown in Figs.8,9. For the main peak, which is around 1eV, the charge-density oscillations are extended over the entire chain, owing to collective excitations. While this peak does not shift under doping, other peaks appear only with doping on doping. The charge-density plot for the additional mode, which is around 5ev, shows the oscillation taking place in the middle area of the chain, which is where the dopant is placed, indicating that the dopant generates local oscillations.

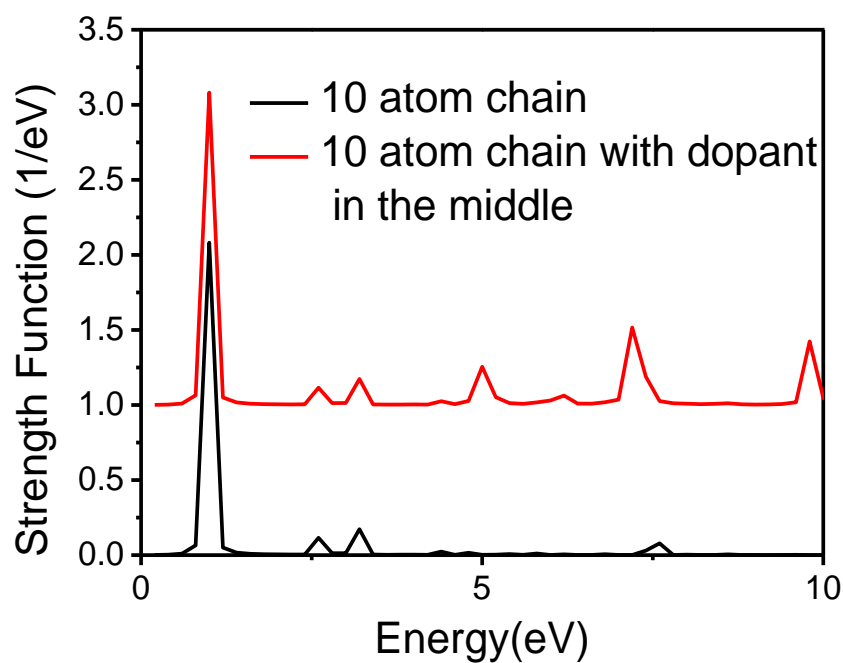


Figure 7 Dipole strength function of a quasi-one dimensional electron gas with 10 atoms

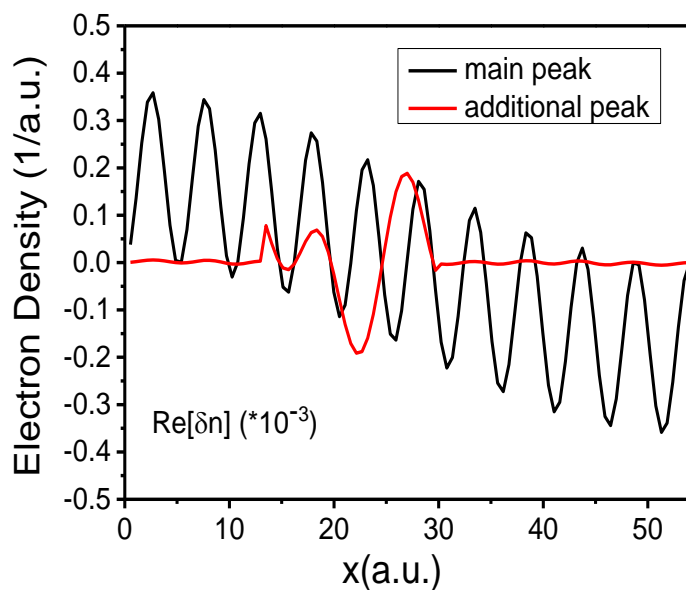


Figure 8 Real part of induced charge densities for a 10-atom chain.

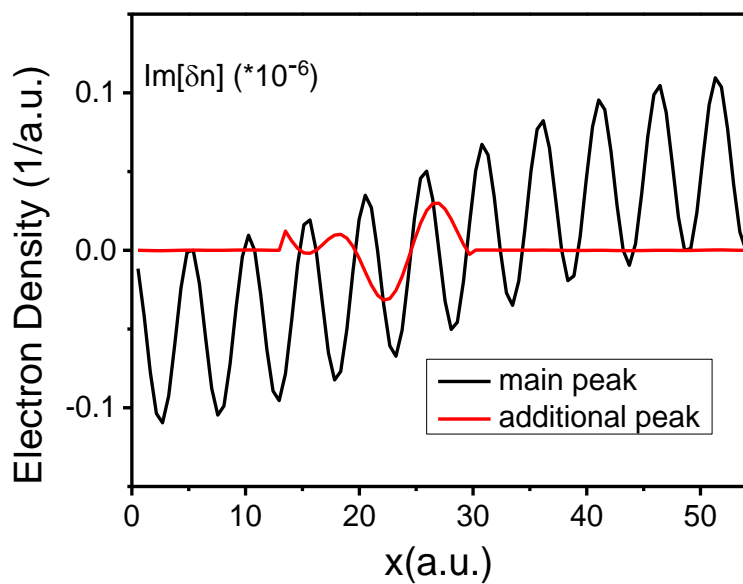


Figure 9. Imaginary part of induced charge densities for a 10-atom chain.

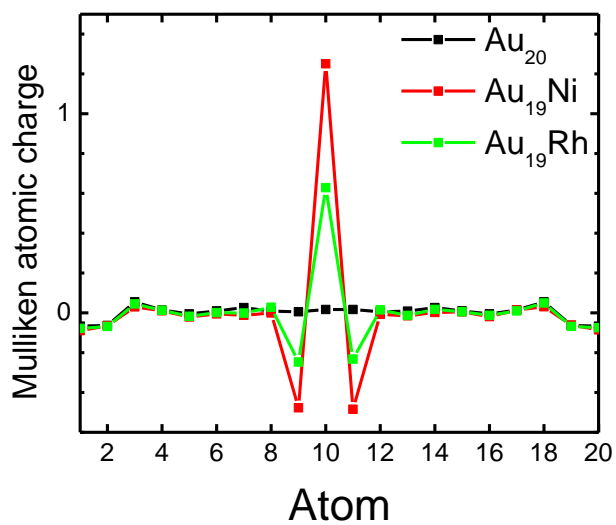


Figure 10. The Mulliken atomic charge distribution in the case of Au_{19}X ($\text{X} = \text{Au}; \text{Ni}; \text{Rh}$) chains. The impurity atom is put at the site 10 from the left.

To get more understanding of possible reasons for the observed splitting of plasmon peaks, we analyze the Mulliken atomic charge distributions in the case of Au and single-doped Au chains. The results for the Au_{20} , Au_{19}Ni and Au_{19}Rh are presented in Fig.10 (The results for Au_{19}Fe are very similar to those for Au_{19}Ni). Since the charge distribution on the edges is almost identical in all three cases and there is no second plasmon peak in the pure Au chain, we infer that the edge oscillations are not responsible for the second peak in the doped chains. On the other hand, among the three cases there are quite strong differences in charge distribution near the impurity atom at the center of the chain. In the case of Ni atom, the impurity ion has a very large positive charge, while the nearest Au atoms are negatively charged. One can think of this situation in terms of a jellium model of electrons in presence of one high potential wall and two neighboring valleys; the rest of the chain can be considered as the positive background, usual in the studies of plasmon phenomena. To understand the difference between the results for Rh impurity on one hand and Ni and Fe impurity on the other, one should note from Fig.10 that the height of the potential well and the depth of the valleys are much smaller in the case of Rh. In this case, when the charge from the right sub-chain close to the valley moves to the right but the valley potential is not deep enough to move the charge back, there is no reason for the local oscillations. The plasmon oscillations can be modeled as a local mode and a collective mode in the case of atom with impurities (Figs.11d and 11e).

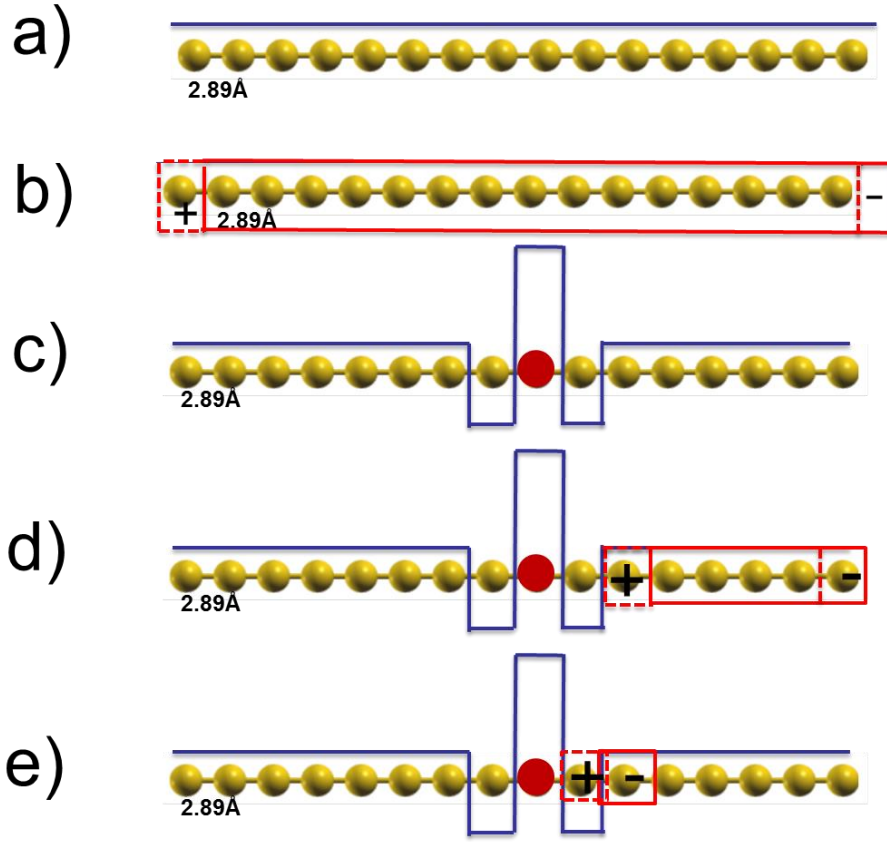


Figure 11. Schematic form of the positive charge background potential for the Au_{16} (a) and Au_{15}X (c) chains. In the case of Au_{16} , the plasmon excitation corresponds to the charge oscillation along all the chain (b). In the case of Au_{15}X chains, there are possible two kinds of plasmonic oscillations: collective plasmon excitations in each half of the chain (d) and local plasmon oscillations on both sides of the impurity atom potential wall (e).

To estimate the necessary potential strength to generate local plasmon oscillations, one can assume that the restoring energy effects are important when this energy is of order

or larger of the kinetic energy in the system. The kinetic energy of electrons can be estimated as twice nearest-neighbor hopping energy. We approximate it by the expression for the Slater-Koster parameter $V_{ss\sigma} = 1.32\hbar^2/md^2$ multiplied by 2, where m is the electron effective mass, which for simplicity we put equal to the free electron mass m_e and $d = 2.89\text{\AA}$ is the inter-atomic distance. This gives $E_{\text{kin}} = 1\text{eV}$. The potential energy is of the order of the local plasmon frequency ω_p , which can be estimated from equation (5). This gives potential energy of chain as 0.638eV which is in good agreement with what we get from our calculations (0.66eV). When an impurity is introduced, its charge shifts to its neighboring Au atoms, and as that charge density increases in turn, the plasmon frequencies increase along with it. From the estimations above, in order to get the local plasmon oscillations it is necessary that $\omega_p \simeq E_{\text{kin}} \sim 1\text{eV}$, which corresponds to the following number of electrons per atom: $(1\text{eV} / 0.66\text{eV})^2 \sim 2$. In other words, the Au atoms nearest to the impurity atoms receive one extra electron – and in doing so generate local plasmons. As one can see from Fig.10, this analysis gives semi-quantitatively correct results in the case of Ni and Rh atoms. In the first case, the extra charge is ~ 0.5 electrons, i.e., on the order of one electron, while in the case of Rh atom the charge received is almost an order of magnitude smaller.

We have also used another analytical model to test the presence of local oscillations around the impurity atom. For this we have used the impurity model suggested by Muniz⁵⁸. The pure chains can be modeled using a tight binding Hamiltonian

$$H_0 = -t \sum_{\langle a,b \rangle} (c_a^\dagger c_b + c_b^\dagger c_a) + \sum_a U_a c_a^\dagger c_a - \mu \sum_a c_a^\dagger c_a \quad (114)$$

where t is the hopping parameter and μ is the chemical potential. U_a is the impurity potential felt at a site which is not the impurity site:

$$U_a = U_o \exp\left(\frac{-|x_a - x_o|^2}{2\sigma^2}\right), \quad (115)$$

here U_o is the impurity potential generated by the impurity present at site x_o and σ defines the range of potential and is given in terms of the lattice sites. We have used $\sigma = \sqrt{2} \times 2.89$, and different U_o 's. The total Hamiltonian consists of H_0 and the impurity perturbation term:

$$H = H_0 + V = H_0 + \sum_{abmn} V_{abmn} c_a^\dagger c_b^\dagger c_m c_n, \quad (116)$$

$$V_{abmn} = \frac{e^2}{2} \int dx \int dx' \frac{\varphi_a^*(x) \varphi_b^*(x') \varphi_m(x') \varphi_n(x)}{|x - x'|}. \quad (117)$$

The polarization operator for the interacting system includes this perturbation term:

$$\Pi(\omega) = \Delta n (\Delta E - \omega I - V \Delta n)^{-1} \quad (118)$$

The diagonal matrices ΔE and Δn are given as

$$\Delta n_{\alpha\beta,\gamma\delta} = \delta_{\alpha\gamma} \delta_{\beta\delta} (n_\alpha^0 - n_\beta^0) \quad (119)$$

$$\Delta E_{\alpha\beta,\gamma\delta} = \delta_{\alpha\gamma} \delta_{\beta\delta} (E_\alpha^0 - E_\beta^0) \quad (120)$$

By using retarded Green's functions, spectral density function of this system is given by

$$A(\omega) = -\Delta n \delta(\Delta E - \omega I - V \Delta n), \quad (121)$$

which is non zero only at the plasmon frequencies because of the delta function. The size of these matrices involved is $n_{site} \times n_{orbital}$. In our calculations we use energy levels from the TDDFT calculations performed earlier. So the first check was to see how many orbitals are required to get accurate results. As in TDDFT we can use as many as 200 orbitals in most part of our calculations and the matrix size is $n_{site} \times n_{orbital}$, we cannot have $n_{orbital}$ larger than 5 for a 20 atom chain.

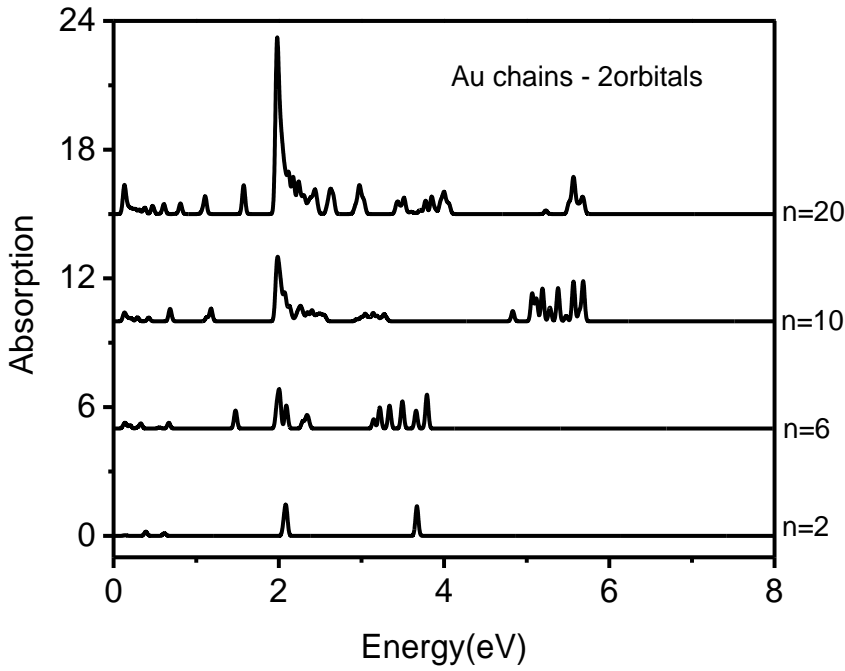


Figure 12. Absorption spectra of 20 atom pure Au chain by using $n_{orbital} = 2$.

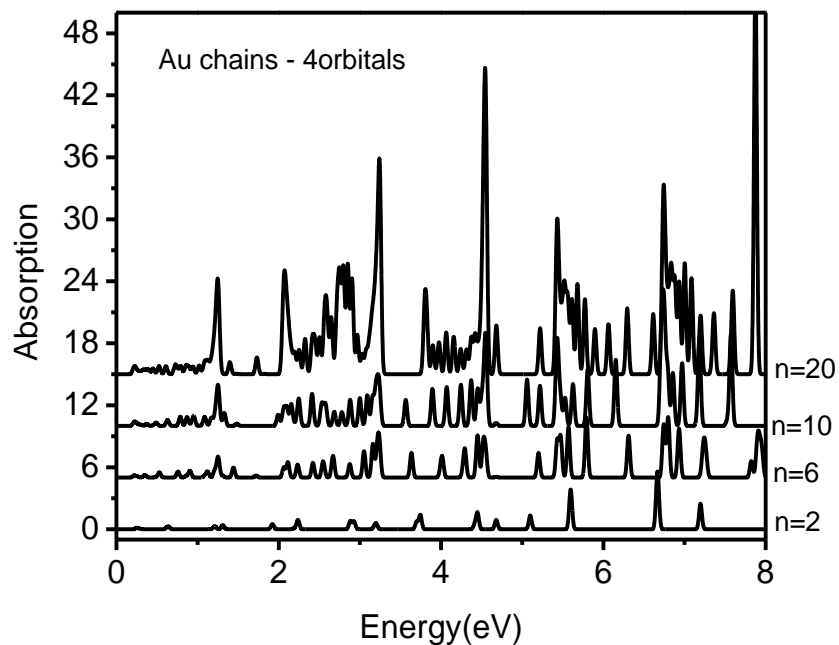


Figure 13. Absorption spectra of 20 atom pure Au chain by using $n_{orbital} = 4$.

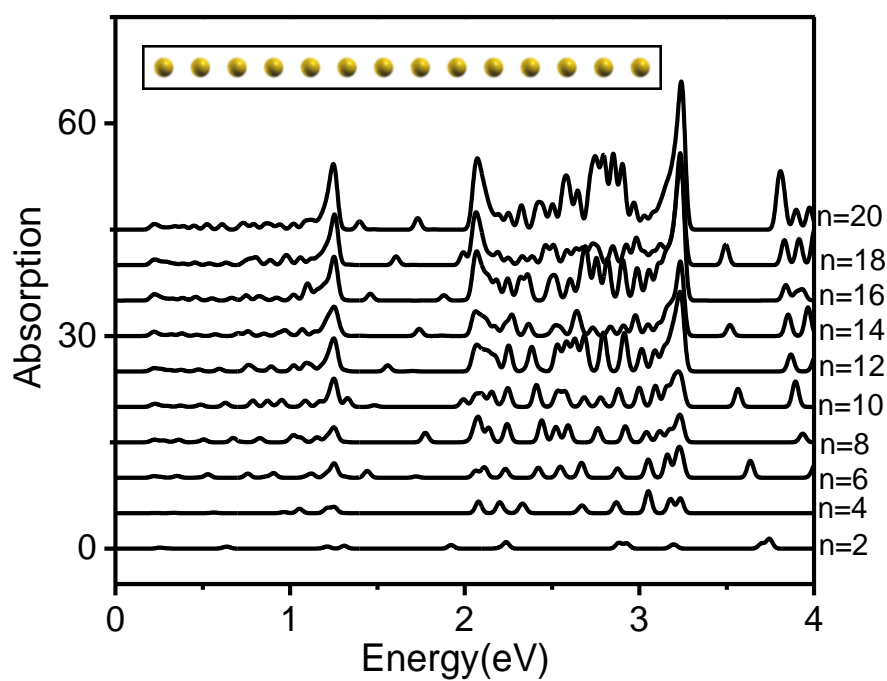


Figure 14 Absorption spectra of pure Au chains using tight binding approach.

Absorption spectrum is calculated using Equation (115). It changes significantly from 2 to 4 orbitals, however our calculations show that there is no significant change when we go from 5 orbitals and above. So we fixed $n_{orbital}$ as 4 for rest of our calculations. The difference between the cases with 2 and 4 orbitals can be seen from Fig.12 and Fig.13. The absorption spectra for pure Au chains show the plasmon peak at 6 atoms and the peak grows with the number of atoms (Fig.14). The features are not as sharp as those from TDDFT calculations as these calculations are based on a simple model and performed only to understand the nature of the oscillations. On adding the impurity atom in the middle additional modes are observed (Fig.15).

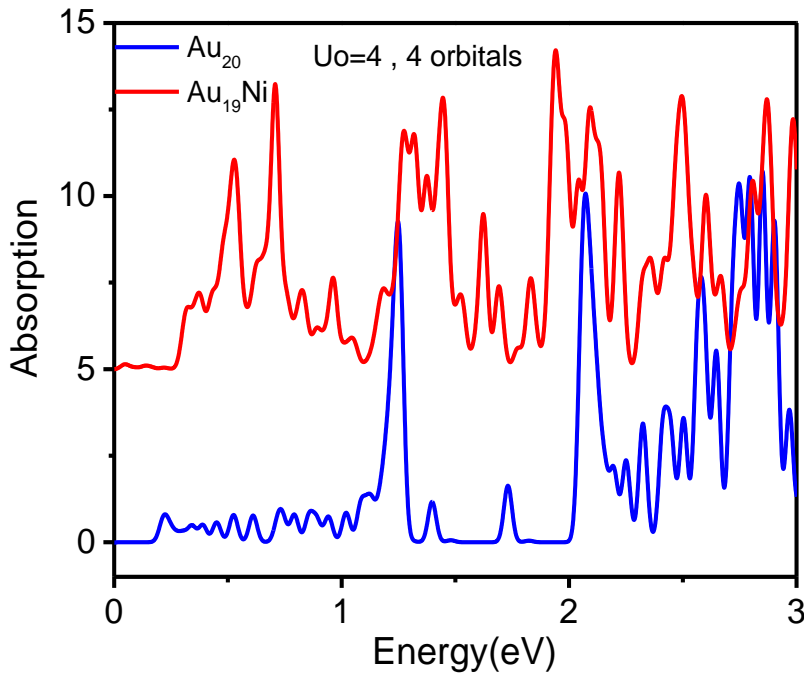


Figure 15. Comparison of absorption spectrum of Au_{20} and $Au_{19}Ni$ chains.

We analyzed the contributions to the local mode by isolating the orbitals that contribute to the strength of the mode to find that in all the cases the orbitals of the impurity atom or the ones surrounding it are the major contributors to the strength of the local peak. Fig. 16 shows the local mode strength for different atoms.

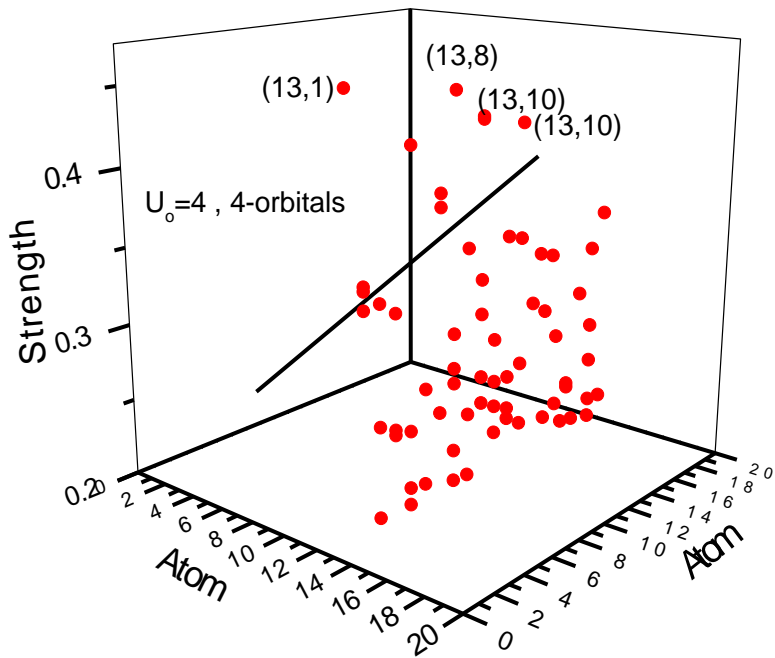


Figure 16. Atoms contributions to the local peak in Au_{19}Ni chain (Ni in the middle).

In Fig.16 it is clear that the contributions are from atom 13 and 10, the latter being the impurity atom. These are contributions from energy close to that of the additional mode, also shown above are only the excitations that have strength > 0.2 units.

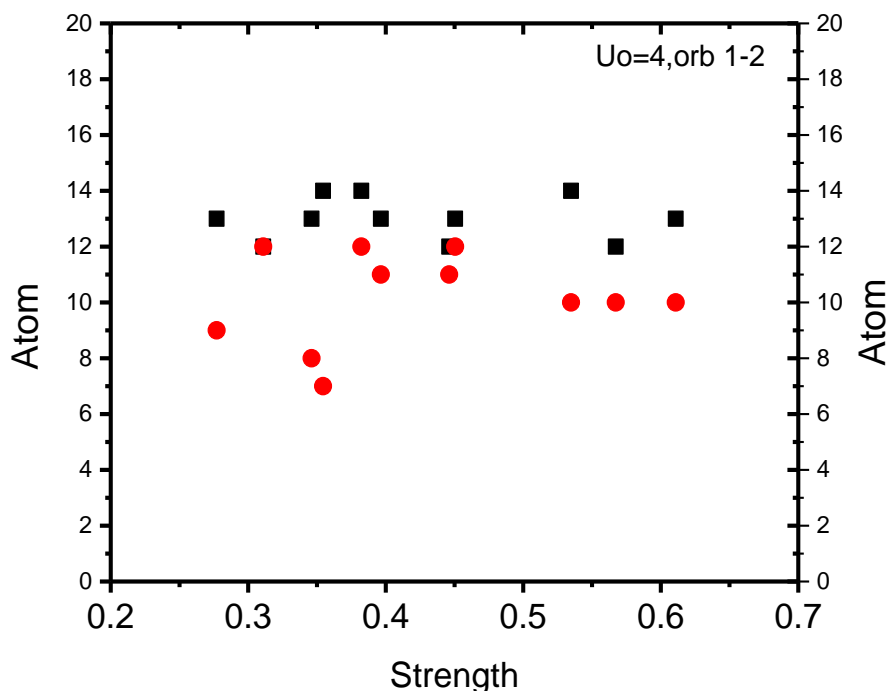


Figure 17 Analysis of the additional mode of Au_{19}Ni chain (black squares represent orbital 1 and red circles represent orbital 2).

Fig. 17 gives a much clearer picture of the dominating atoms with the orbitals contributing to the local oscillations: the strength is coming from oscillations between the impurity atom number 10 and the atoms surrounding it. It is also seen that atoms further away on either side of the impurity (labeled <6 and >16) do not participate in the local oscillations, confirming our earlier prediction.

One can also analyze the basis for the charge redistribution from the bonding point of view. Since there is only one valence s-electron in the case of a Rh atom, this electron participates in σ bonding, while the eight d-electrons are not very chemically active. Thus, one can assume that the charge of the Rh core is +1, similar to the Au atoms,

with the result that the positive and negative charges of the Au_{n-1}Rh and Au_n "plasmas" are almost the same. Hence, the type of excitations in these chains will be the same, i.e. a single plasmon peak. In the case of Ni and Fe atoms, the valence s-state is doubly occupied which means that it is mainly the d-states that contribute to atomic bonding. A more precise look shows that d^2 , dxz and dyz orbitals donate most of the charge to the bonding, resulting in a positively charged core with charge $Z > +1$. This is the main reason for the potential well at the impurity atom. Thus, one can estimate which sorts of atoms may lead to the generation of a localized plasmon by looking at the bonding charge redistribution. Obviously the estimation presented above is not very accurate, but more refined estimations can be easily obtained by improving this one, in particular by using some more accurate values for the electron effective mass. We believe, however, that even such simple estimations give the energy of possible plasmon excitations within the correct order of magnitude. In summary, we have shown that weak doping of Au chains with some TM metal atoms may lead to generation of local plasmon modes. This effect is a result of a delicate balance between s- and d-states of the dopant atoms causing charge redistribution in chain near the TM atom. We propose a simple criterion for the possibility of generation of local plasmon mode based on this charge redistribution, i.e. the double occupancy of the highest s-orbital and partial occupancy of the d-states are necessary for this. Our results show that some TM metal atoms can be used to tune the optical properties of nanostructures.

3.1.3 Multiple Chains

Recently, detailed studies have been done on the mechanism of the collective excitations of alkali-metal clusters.⁵⁹⁻⁶¹ Ma et al.⁶² studied the sensitivity of plasmon resonance in Au nanoparticles and their dimers as a function of particle size and inter-particle distance. Studies of the plasmon excitations in planar Na structures^{63, 64} reveal the importance of dimensionality in the formation and development of the plasmon peaks. Recently, Scanning Tunneling Microscope (STM) experiments have demonstrated development of 1D band structure in Au chains on NiAl(110) when the number of atoms in the chain exceeds 10.²⁰ In the previous section and in our study⁶⁵ we examined the role of TM doping in generating plasmon modes in single Au chains, demonstrating that such doping leads to several changes in the absorption spectrum, including (most strikingly) new local mode. These new excitations are a result of a complex rearrangement of the ionic potential around the impurity atom felt by the delocalized electrons participating in the plasmon oscillations around the TM atom, as well as a collective effect of the localized (TM d-) and de-localized (s) electrons. Indeed, the mutual effects of both subsystems may be nontrivial, in particular leading to a change of the spectral function of the localized electrons (see, e.g., Ref. ⁶⁶), or to local electronic resonances around the dopant atom, as was shown experimentally in the case of Pd-doped Au chains on NiAl(110).⁵³ This complexity opens the door to new opportunities for tuning the optical properties of nanostructures by changing their shape or size and by TM doping. In this study, we confirm this possibility for several coupled noble-metal/TM and pure noble-metal nanochains.

3.1.3.1 Computational Details

All calculations have been carried out using the TDDFT approach as employed in the Gaussian 03⁵⁴ code with a B3PW91 hybrid functional^{31, 30, 29} and a LanL2DZ basis set⁵⁵. Unless specified, all interatomic distances are set to be 2.89 Å. The absorption spectrum is calculated from Equation (63) where E_i and $\langle i|D|j\rangle$ are the energy levels and transition dipole moments respectively computed from TDDFT calculations, ω is the oscillation frequency and Γ is the peak broadening which we set to 0.2 eV. For clarity of the figures, in plotting $A(\omega)$ we neglect the contribution of dipole moments with intensity of less than 1% of the main plasmon peak.

3.1.3.2 Results

(1)*Pure chains*: Increasing of the number of atoms in the double chains leads to generation of a plasmon mode when n reaches a certain threshold. This mode gains strength and moves to lower energy with further increase in the number of atoms. Fig.18 shows how this mode is generated when $n \geq 6$ (n being the number of atoms in one chain, the 10-atom chain is shown on the top). in double Au chains – similar to what happens in the case of a single Au chain.⁶⁵

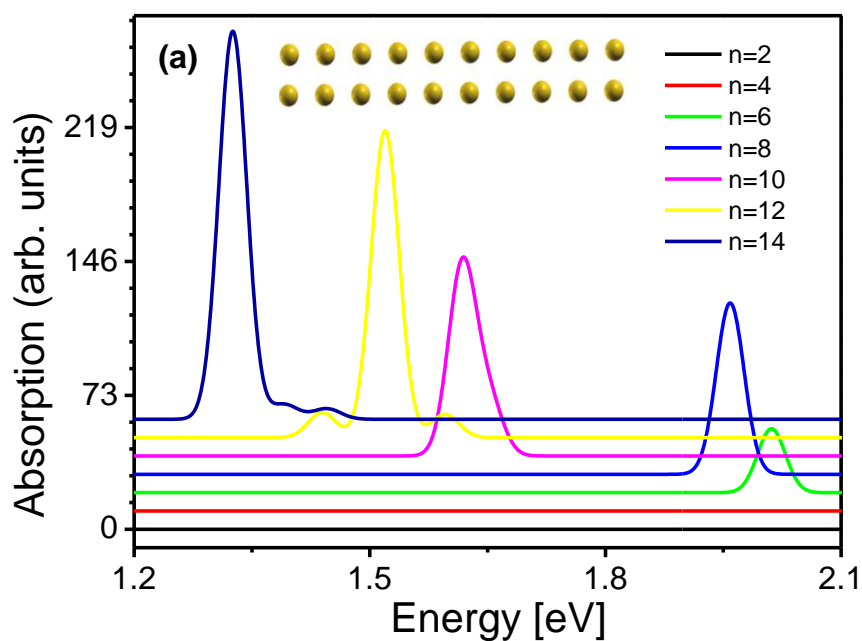


Figure 18 Optical absorption spectra of the n -atom double Au chains, $n=2-14$

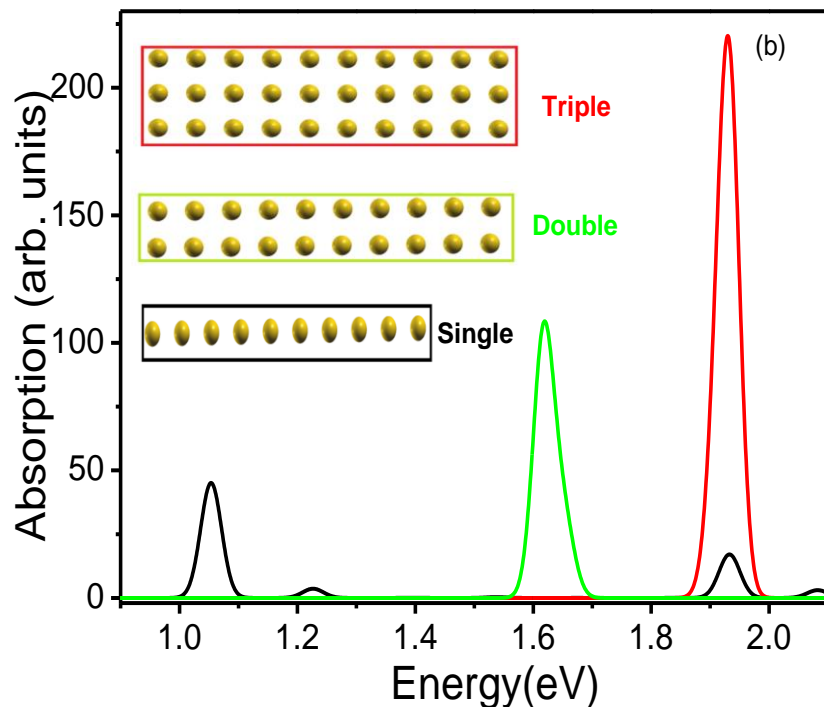


Figure 19 Absorption spectra of arrays of pure Au chains of 10 atoms each.

The absorption spectra of single, double and triple ten-atom Au chains (Fig. 19) demonstrate that the plasmon peak moves in to the visible range (1.7eV -3.0 eV) as the number of chains increases. A similar effect can be produced by changing the geometry of the system while keeping the number of atoms fixed (Fig. 20). We have considered four different geometries, three of which have been previously studied, but for infinite chains³⁷. In the square pattern (SQ3) the two chains are parallel to each other, and each atoms coordination number is three. In single zigzag geometry the chains are aligned at some (non - 90^0) angle to each other, depending on the vertical distance between the two chains. Each atom's coordination number is four. Examples are ZZ4-eq (in which that angle is 60^0 , so that the atoms form equilateral triangles) and ZZ4-iso (in which they form this or that isosceles triangle). In double zigzag geometry (ZZ3+5), two zigzag chains are combined. Although the average coordination number is four, but four atoms in the unit cell alternate between coordination number three and five. The plasmon peaks for SQ3 and ZZ4-iso chains lie below the visible range, while two of the three for ZZ4-eq and both of those for the ZZ3+5 chains fall within the visible range.

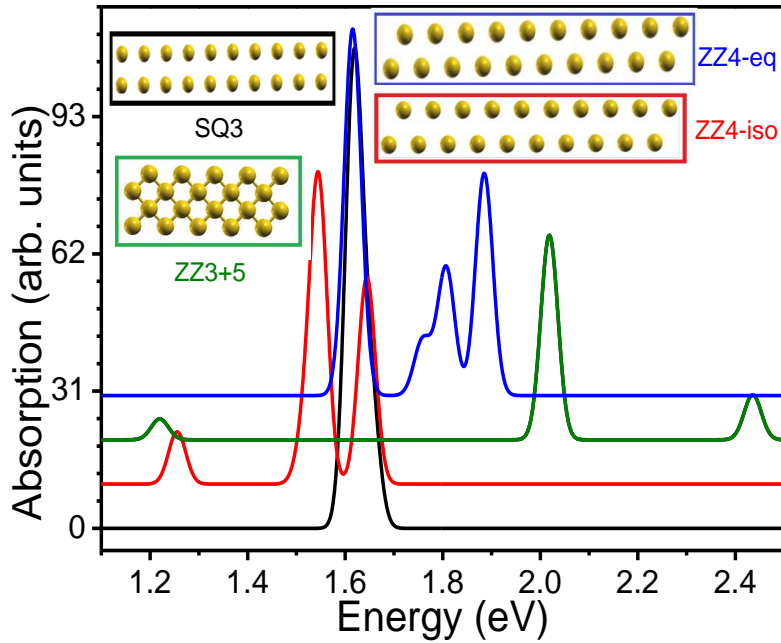


Figure 20 Absorption spectra of pure Au chains with different geometries -- square, zigzag (with different vertical distances between chains) and double zigzag.

(2) *Doped chains*: The contrast between the absorption spectra of single and double TM-doped chains is more complicated than that between the corresponding spectra of pure single and double chains. In both cases the peaks shift to higher energy and the strength of the plasmon peak increases. However, when the chains are doped in the middle with TM, bringing two chains together increases the number of plasmon modes and moves some of the absorption spectrum peaks into the visible range (Fig 21). Putting Ni atom at the end of chain does not affect the plasmon mode of pure Au double chains whereas Ni in the middle splits the mode into two. However, it's not the case with Pd doping. (Fig. 23).

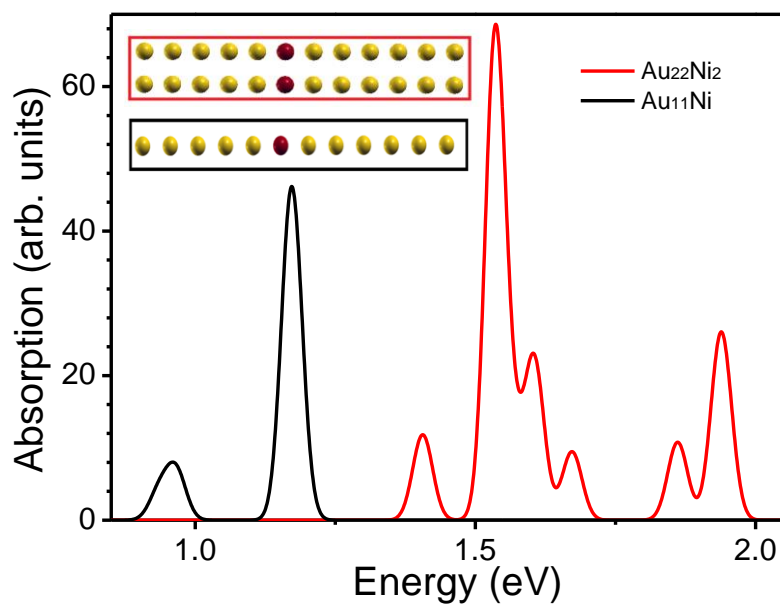


Figure 21 Optical absorption spectra of single and double Au_{11}Ni chains.

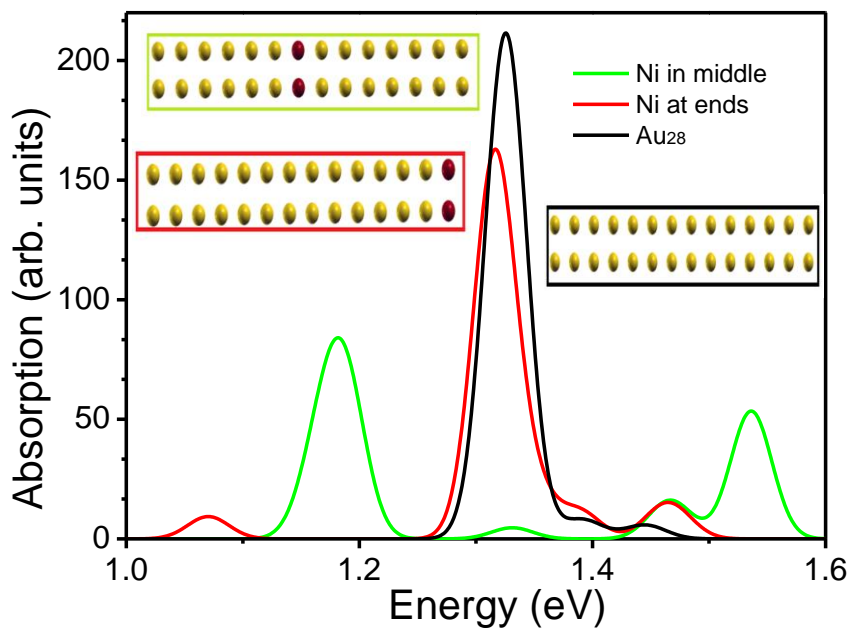


Figure 22 Optical absorption spectra of Au_{28} , $\text{Au}_{26}\text{Ni}_2$ (Ni in the middle) and $\text{Au}_{26}\text{Ni}_2$ (Ni at the end) chains.

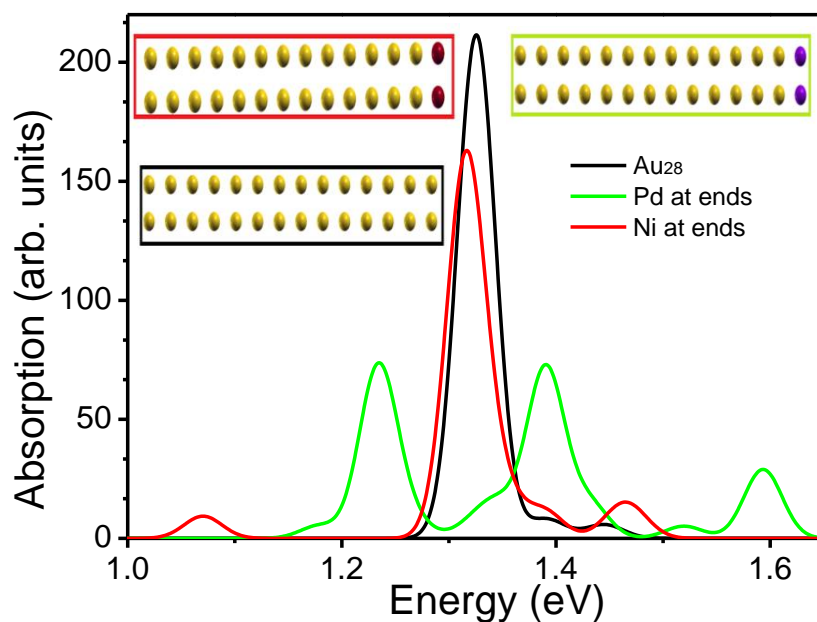


Figure 23 Optical absorption spectra of Au_{28} , $\text{Au}_{26}\text{Ni}_2$ (Ni at the end) and $\text{Au}_{26}\text{Pd}_2$ (Pd at the end) chains.

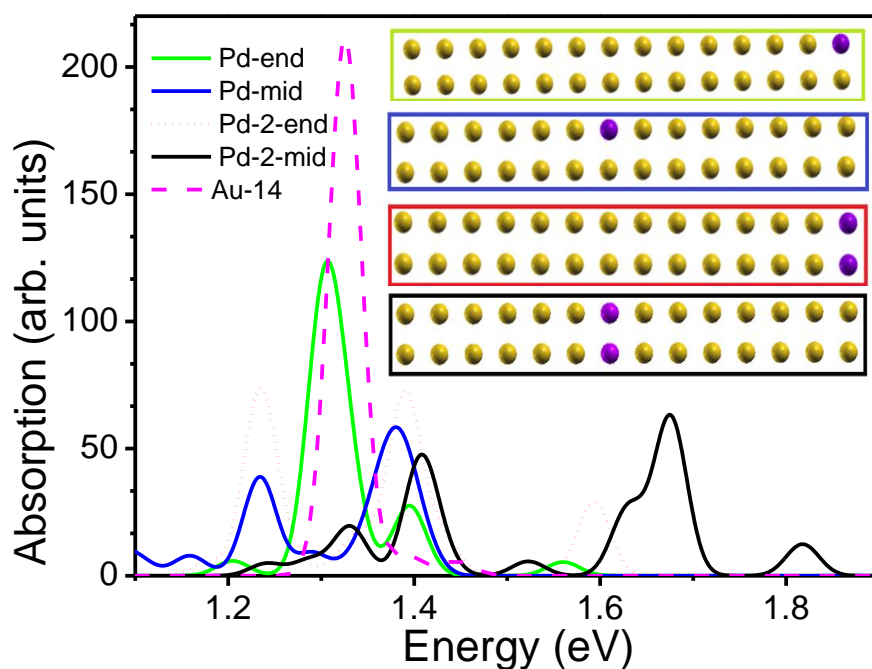


Figure 24 Optical absorption spectra of Au_{28} , $\text{Au}_{26}\text{Pd}_2$ (Pd at ends and in the middle) and Au_{27}Pd (Pd at the end and in the middle) chains.

(3)Mixed Chains: In the case of double chains, one of which is Au and other either TM or other noble-metal, the results are also very interesting. In particular, when an Ag chain is coupled with a Cu chain, the resulting plasmon peak is situated halfway between the peaks of pure Ag and pure Cu double chains (Fig.25). But when either an Ag or a Cu chain is coupled with an Au chain, the plasmon peak is much closer to that of the pure Au double chain than that of either of the pure Ag or Cu chains, implying that collective oscillations from Au chains are much stronger than from two other chains. When the Au chain is coupled to a TM (Ni, Fe, Rh, Pd) chain the plasmon modes are highly suppressed (Fig. 26).

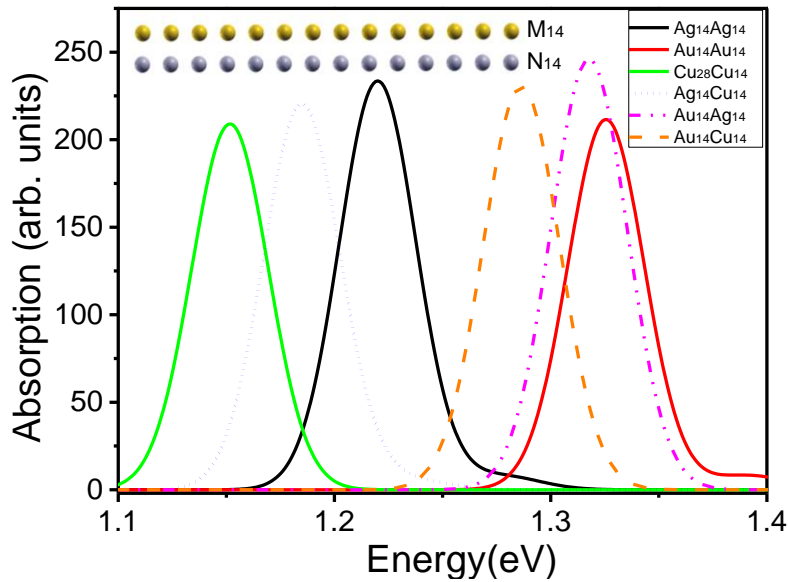


Figure 25 Coupled $M_{14}N_{14}$ chains absorption spectra (a) $Au_{14}Au_{14}$, $Ag_{14}Ag_{14}$, $Cu_{14}Cu_{14}$, $Au_{14}Ag_{14}$, $Au_{14}Cu_{14}$, $Ag_{14}Cu_{14}$ chains.

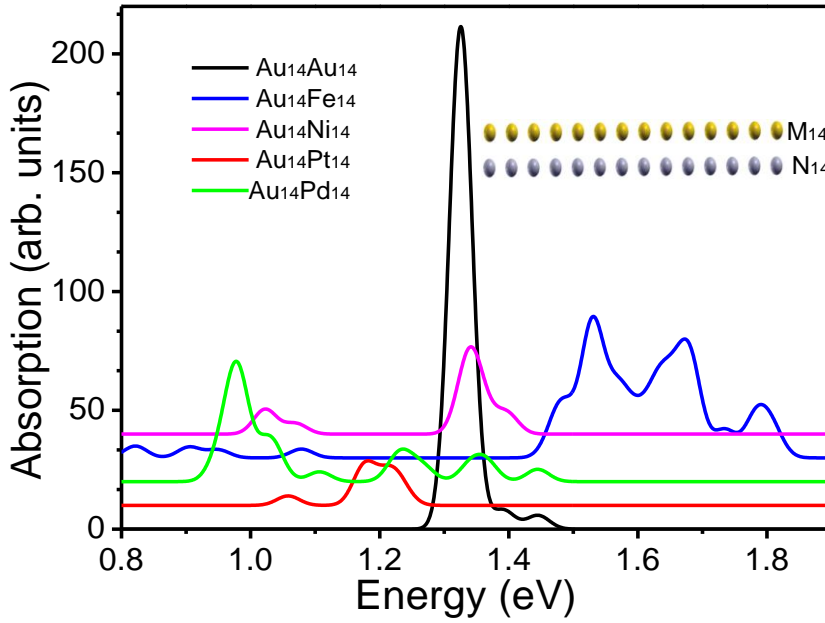


Figure 26 Coupled $M_{14}N_{14}$ chains absorption spectra, $Au_{14}Au_{14}$, $Au_{14}Ni_{14}$, $Au_{14}Pt_{14}$, $Au_{14}Pd_{14}$, $Au_{14}Fe_{14}$ chains.

3.1.3.3 Discussion

As follows from the results, the position of the plasmon peak in pure chains moves to the right as the number of atoms increases (Fig. 19). This effect can be described by the simple expression for the plasmon energy which follows from the jellium model:

$$E = \hbar \sqrt{\frac{4\pi n_{el} e^2}{m}} \quad (122)$$

In this expression, n_{el} is the charge density and, e and m are the electron charge and mass, for which we use the free-electron values. The particle density is $n = N/V$, $N = nn_{ch}$ is the number of s-electrons (n – the number of atoms in the chain, n_{ch} - the

number of chains), and V is the volume of the system, which can be estimated as follows. It is equal to the effective system length l multiplied by the effective width d and height h . The chain length can be approximated by $l = \Delta l(n - 1) + 2R$, where $\Delta l = 2.89\text{\AA}$ is the inter-atomic distance in the chain, and R is the s-orbital radius. The last quantity can be estimated as the radius of the sphere around the atom which contains 90% of the s-electron charge. For Au atoms this comes to $R=21.07\text{\AA}$. The system height is $h=2R$ in this case, and the system width $d = \Delta l(n_{ch} - 1) + 2R$, which gives:

$$E = \hbar \sqrt{\frac{2\pi n n_{ch} e^2}{mR[\Delta l(n-1)+2R][\Delta l(n_{ch}-1)+2R]}} \quad (123)$$

Since in a system consisting of only few chains $\Delta l(n_{ch} - 1)$ is much smaller than $2R$, and in a system consisting of long chains ($n>20$), $\Delta l(n - 1)$ is much larger than this quantity, one can use the following approximate expression for the dependence of the plasmon energy on the number of atoms in the chain:

$$E = \hbar \sqrt{\frac{\pi e^2 n_{ch}}{mR^2 \Delta l}} \quad (124)$$

For the parameters used above this gives $E \approx 0.52eV\sqrt{n_{ch}}$, or 0.52eV, 0.74eV and 0.9eV, for the single-, double- and triple-Au chains, respectively. This is in reasonable agreement with the results presented in Figs. 18 and 19. One can also estimate the plasmon energy for 2D (infinite) arrays. In this case, $n, n_{ch} \rightarrow \infty$, so that one gets from Equation (117)

$$E \approx \hbar \sqrt{\frac{2\pi e^2}{mR\Delta l^2}} \approx 1.98eV. \quad (125)$$

As it follows from these estimations, the energy of the plasmon peak moves into the visible range as the number of chains increases.

Another important result which follows from Equation (117) is an additional criterion for recognizing the presence of collective response of the system: when $\Delta l(n - 1)$ becomes larger than $2R$ the plasmon energy weakly depends on the chain length (n 's in the numerator and denominator cancel), as should be the case for the collective behavior of “the extended” system. In other words, the criterion of collective response is $\Delta l(n - 1) > 2R$, or $n > \frac{2R}{\Delta l} + 1$, which gives $n > 15.5$. Given the simplicity of the model this is in reasonable agreement with the numerical result $n > 10$. The energy becomes almost n -independent when $\Delta l(n - 1) \gg 2R$, or $n \gg \frac{2R}{\Delta l} + 1 = 15.5$, which is again in agreement with the analytical estimation of $n > 20$.

In the case of doped chains, the shape of the spectra strongly depends on the chemical composition of the structures and on the position of the impurity atoms. In the single-chain case, as we have reported earlier³⁴, a single impurity leads to an extra peak in the case of some TMs, and the plasmon peaks are suppressed when the number of impurities is large enough ($\sim 4-5$).

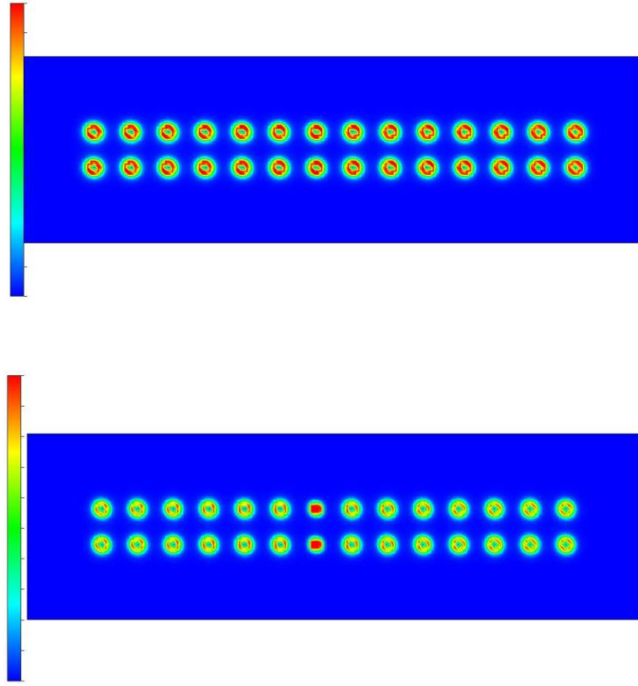


Figure 27. The electron charge density in the case of two Au_{14} chains doped in the middle by Rh(top) and Ni (bottom) atoms.

The plasmon effects were found to be especially pronounced in the case of Ni, and almost absent in that of Rh. Our analysis demonstrated that this can be explained by a local potential created by the d-electron impurity, which leads to charge oscillations around it in the case of excited system. Since the Rh atom has only one s-valence electron, it did not significantly perturb the Au system. Doping with Rh barely affects the charge distribution, which corresponds to the jelly model (with its homogeneous positive background). On the other hand, doping with a Ni atom introduces a strong repulsive potential at its location and generates attractive valleys at neighboring Au atoms (see Fig 27 in which one can compare the charge gradients in the Ni- doped and pure systems).

In the case of doped multi-chain structures the situation is more complicated. One would expect in general to find local and collective plasmons in each chain, and that interaction among these many modes leads to extra (“hybridized”) peaks, so that the plasmon spectrum is much more complex and difficult to understand. Moreover, when the chains and/or the impurity atoms in different chains are close to each other one might anticipate inter-chain oscillations, i.e. the appearance of additional new modes. In order to get some insight on the nature of possible plasmon excitations in such doped multi-chain systems, we present the Mulliken charge distribution and charge densities for all the absorption spectra presented above (Figs. 28-35). As these figures indicate, an impurity atom leads to a significant redistribution of the Mulliken charge, and hence the effective positive background charge.

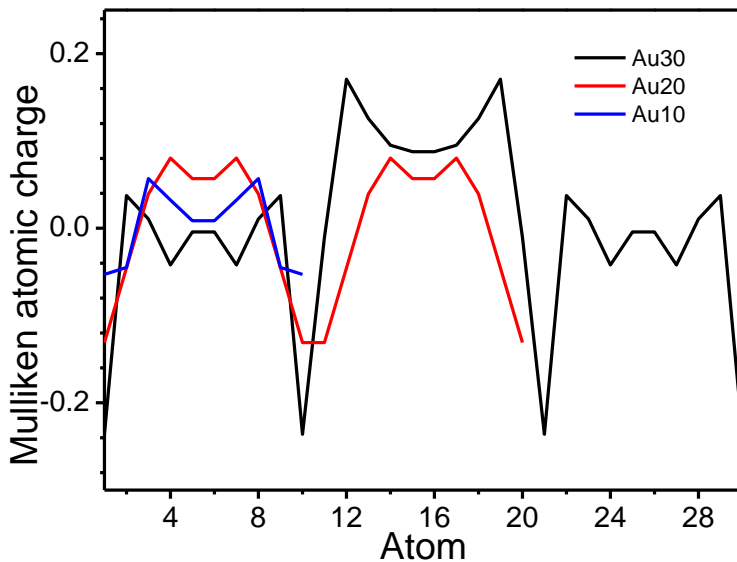


Figure 28. Mulliken atomic charge for the pure Au chains illustrated in Fig. 19 with different array sizes.

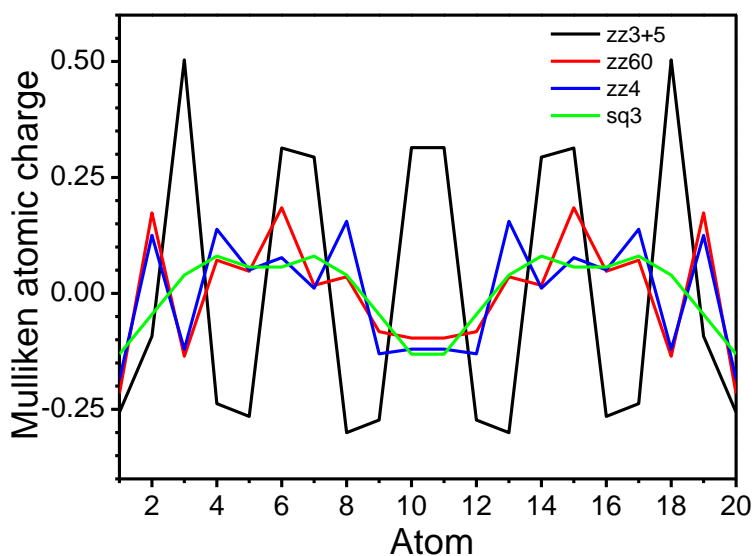


Figure 29. Mulliken atomic charge distribution for the pure Au chains with different geometries presented in Fig.20

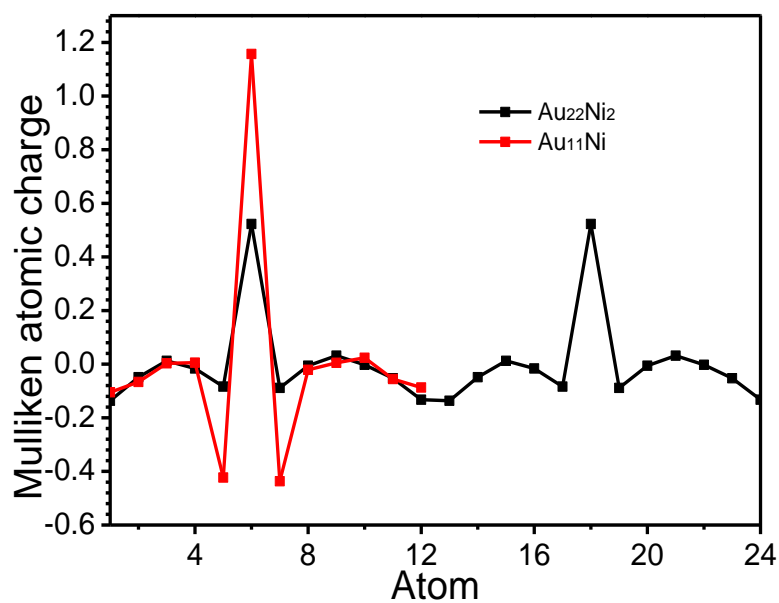


Figure 30. Mulliken atomic charge distribution for the Ni-doped Au chains illustrated in Fig. 21 (the second chain atoms in the double chain correspond to Atoms 13-24).

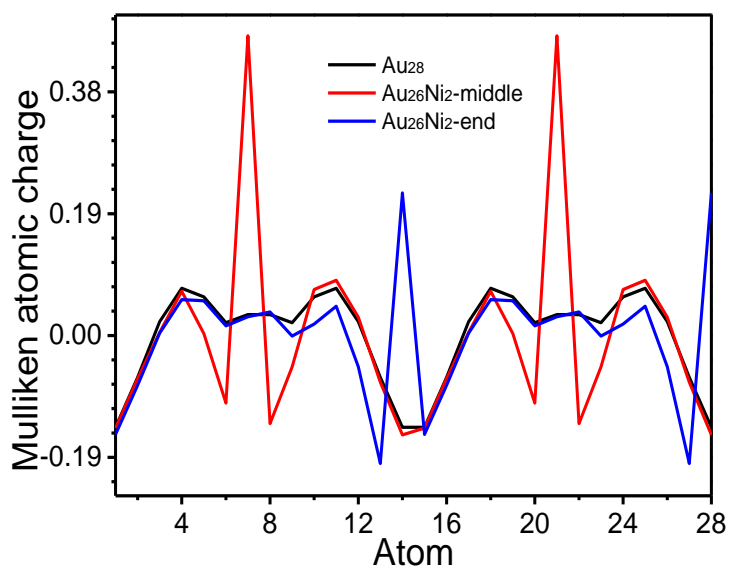


Figure 31. Mulliken atomic charge for double Au chains – one pure, one doped with Ni in the middle, one doped with Ni at the end.

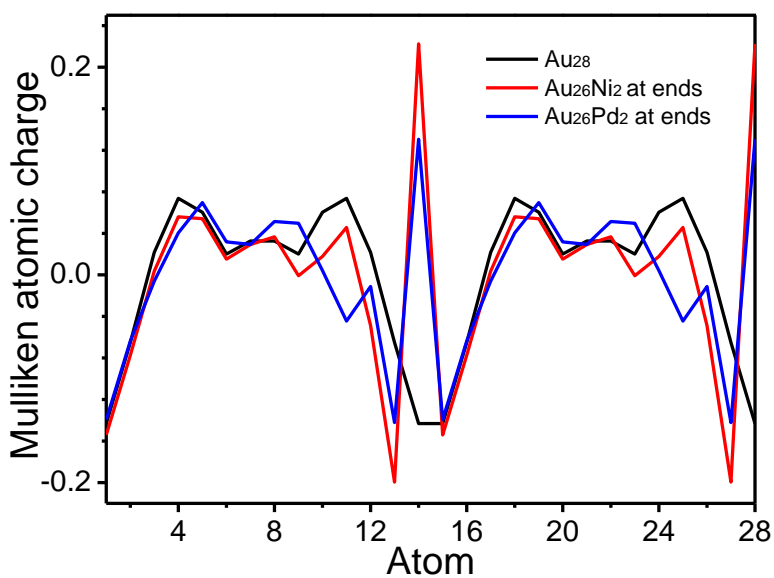


Figure 32. Mulliken atomic charge for the Au chains illustrated in Fig. 4: pure, end-doped with Ni and end-doped with Pd with 1 and 2 Pd atoms at different positions.

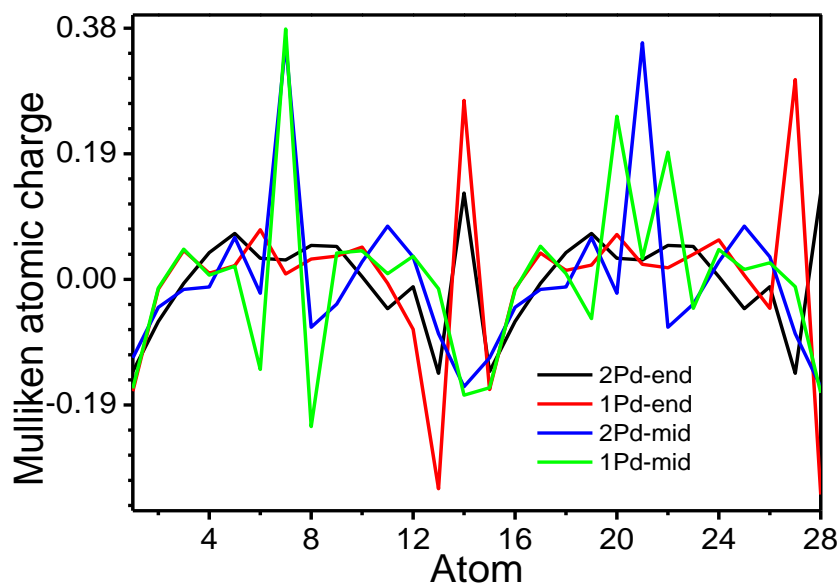


Figure 33. Mulliken atomic charge for the Au chains with 1 and 2 Pd atoms doped at different positions.

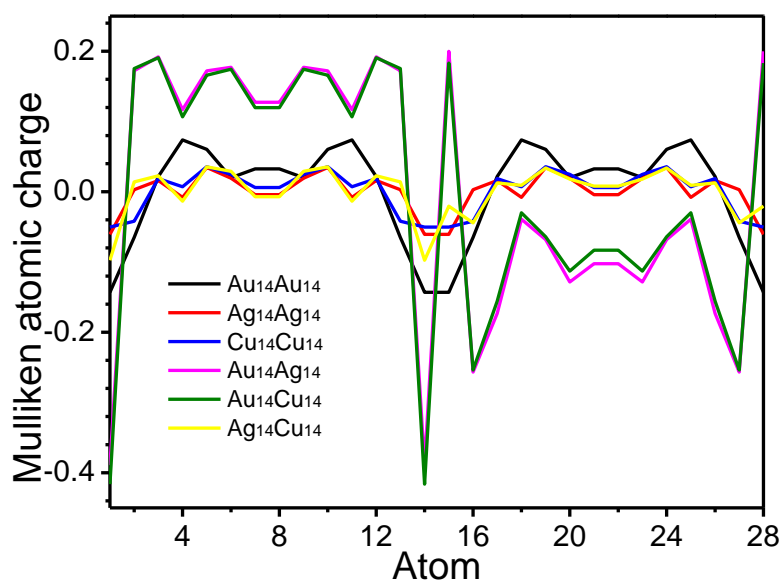


Figure 34. Mulliken atomic charge for coupled the $M_{14}N_{14}$ chains illustrated in Fig. 5: Au_{28} , Ag_{28} , Cu_{28} , $Au_{14}Ag_{14}$, $Au_{14}Cu_{14}$, $Ag_{14}Cu_{14}$ (b) Au_{28} , $Au_{14}Ni_{14}$, $Au_{14}Pt_{14}$, $Au_{14}Pd_{14}$, $Au_{14}Fe_{14}$.

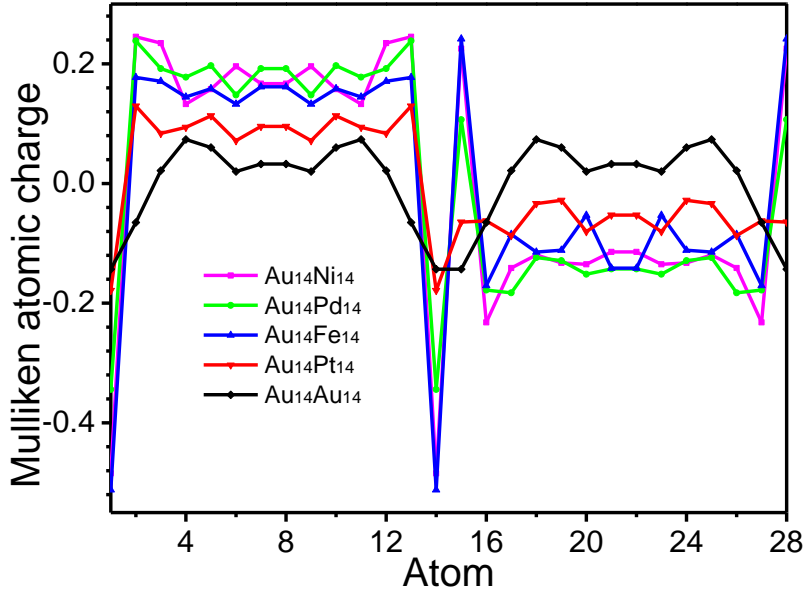


Figure 35. Mulliken atomic charge for coupled the $M_{14}N_{14}$ chains: Au_{28} , $Au_{14}Ni_{14}$, $Au_{14}Pt_{14}$, $Au_{14}Pd_{14}$, $Au_{14}Fe_{14}$.

An effective theory of plasmon excitation in this case can be described by the following system of equations:

$$i\dot{p}_{i\alpha} = \varepsilon_{i\alpha}p_{i\alpha} + \sum_{j,\alpha \neq \beta} V_{i\alpha;j\beta} p_{i\alpha}p_{j\beta}, \quad (126)$$

where $\varepsilon_{i\alpha}$ is the energy of plasmon in chain i , α or β are the corresponding local or collective modes, and $V_{i\alpha;j\beta}$ is the plasmon-plasmon coupling within the system. Since the plasmon-plasmon interaction is of the dipole type, it should decay rapidly ($1/R^3$) with increase in the distance R between the plasmon “centers of mass,” so only the nearest-chain interaction matrix elements V need to be taken into account (as highlighted in Fig.38). Therefore, the corresponding modes will split, leading to extra modes with respect to the single chain case. The striking results for the (and only for the) Pd edge-doped chains leads to extra modes can be explained by an enhanced “resonance”, due

to interaction between the oscillations at the end of the chains with collective modes. Though such qualitative analysis can provisionally explain the main features of the plasmon spectrum in this case, a detailed quantitative analysis is necessary for every particular case.

Another surprising result is suppression of the plasmon modes in noble metal chains coupled to a TM chain (Fig. 26). Although both chains support plasmons (albeit weaker for TM), in the coupled case these excitations are damped by the strong mutual scattering between the d-wave orbital charges of the TM chain, orbitals oriented perpendicularly to the chains, and the s-orbitals of the neighboring Au chain.

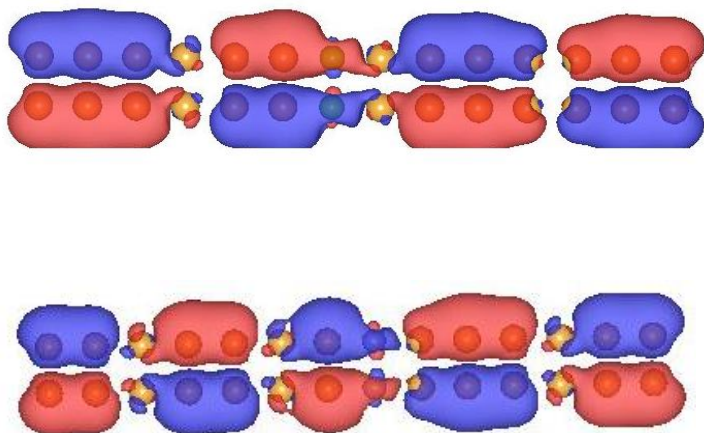


Figure 36. HOMO (top) and LUMO (bottom) of two Au₁₄ chains each doped in the middle by one Ni atom (red and blue indicate an extra and missing charge, respectively).

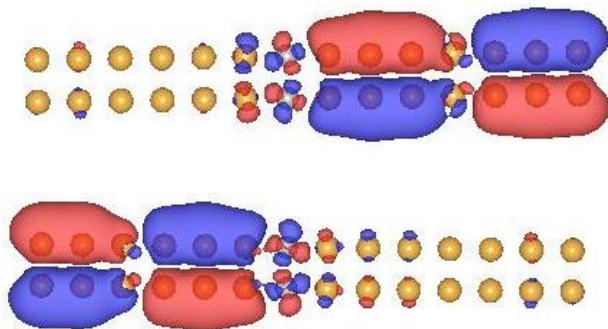


Figure 37. The same chains as in Fig. 29 but doped (also in the middle) with Pd atoms.

Finally, we would like to draw attention to the charge redistribution in the Ni- and Pd-doped systems when they are excited from the HOMO to the LUMO states (Figs 37,38). Since such an excitation can take place simultaneously with the plasmonic excitations, it may lead to interesting effects on plasmon oscillations as well as on charge and energy transport. While in the case of Ni doping, the HOMO-LUMO excitations lead mostly to “a flip” of the quasi-periodic areas with extra and missing charge (with two such new areas), in the Pd case the areas with the charge non-homogeneity in the HOMO state emerge to the right of the impurity, but moves to the left when the system is LUMO-excited. The effect of the LUMO (and possibly other) excitation(s) on the behavior of plasmons is a problem for future studies. Appendix A shows various molecular orbitals HOMO-LUMO for different cases under study.

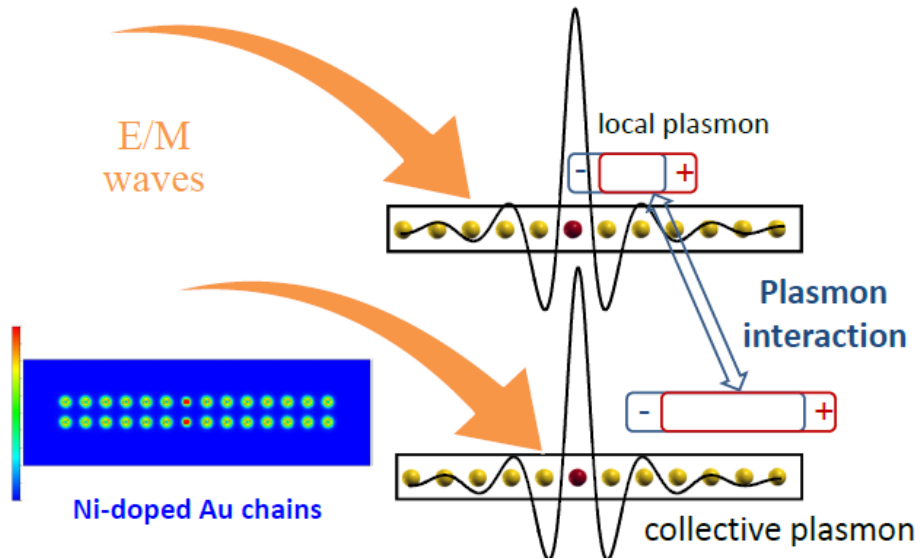


Figure 38. Schematic representation of the collective and local plasmon oscillations in double chains.

To summarize, we have analyzed the optical properties of arrays of multiple pure and TM-doped noble metal nanochains systems. In the case of pure chains, the system demonstrates a plasmon peak when the chain contains about 10 atoms or more. The position of the peak in the optical absorption spectrum moves to lower energies as the number of atoms n increases, and becomes almost n -independent at $n > 20$. The position of the peak moves to higher energies when the length of the chain is fixed but the number of chains increases. Doping of a single chain with some TM atoms (with different non filled shells) leads to extra plasmon peaks which can be explained by local plasmon oscillations around the impurity atom (Fig.38). In the multichain case such doping leads to multiple in-chain plasmon oscillations and also to an inter-chain interaction between different plasmon modes, mostly in the nearest-neighbor chains.

These extra plasmon modes can be explained as a result of plasmon-plasmon interaction, which leads to the mode splitting of the modes. Interestingly, we have found plasmon modes even in pure TM chains. To our knowledge, ours is the first report of such an effect in TM materials, though when such pure chains coupled to pure noble metal chains, no plasmon modes were found, owing to mutual scattering between s- and d-states excitations in different chains. Though our studies have mainly focused on Au chains doped with Ni, Rh or Pd atoms, but as pure Ag and Cu cases behave similarly to Au, so one can expect similar picture for Ag and Cu chains doped with TM atoms. The results obtained in this paper can be used to tune the optical properties of nanosystems including the visible spectrum case.

3.2 Effects of Exciton Plasmon Interaction in Coupled Chains

3.2.1 Excitons

An exciton is an electrically neutral quasiparticle consisting of a bound pair of electron and hole which are attracted to each other by electrostatic force. As excitons are electrically neutral particles, they can transfer energy without transferring net charge. Excitons are formed when a photon with energy larger than the bandgap, excites an electron from the valence band into the conduction band of a semiconductor or insulator. As an electron moves into the conduction band, it leaves behind a hole that has a positive charge and an effective mass that may be similar to that of the electron. These positive and negative charges attract each other through a screened Coulomb attraction and form a bound pair (Fig.39).

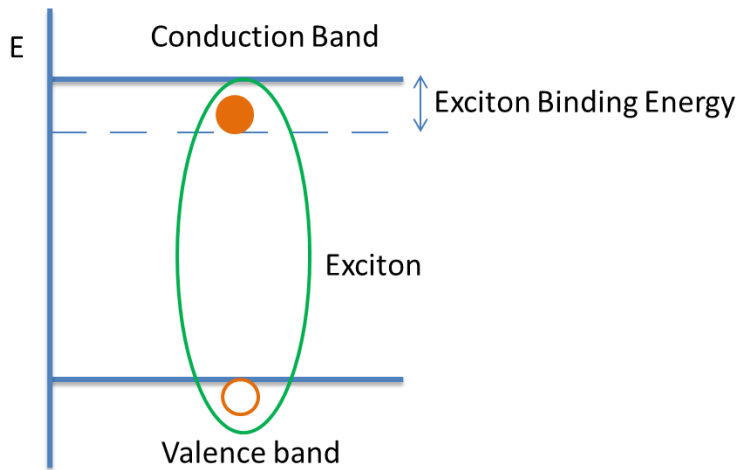


Figure 39 Schematic representation of an exciton.

An exciton has two momenta: the pseudomomentum, which is equal to the vector sum of electron momentum and hole momentum (center-of-mass momentum) and the relative momentum of the electron and the hole. The pseudomomentum enables exciton to move throughout a crystal and the relative momentum determines its internal structure. Excitons are classified into Frenkel and Wannier types based on their size.

Frenkel Exciton: Excitons localized over a single lattice site are called Frenkel excitons. They are tightly bound excitons that can hop from one atom to another. If the electron is excited from the valence band of one atom to its conduction band, it can move into the conduction band of the neighboring atom. Now as the neighboring atoms have an additional electron in the conduction band the repulsive force between the valence and conduction band electron might push the valence band electron to the corresponding atom to fill the hole there. So, the electron-hole pair moves to the neighboring atom. The translational states of Frenkel excitons take the form of propagating waves just as

excitations in periodic systems. Frenkel excitons are most commonly found in biological systems, polymers and molecular crystals.

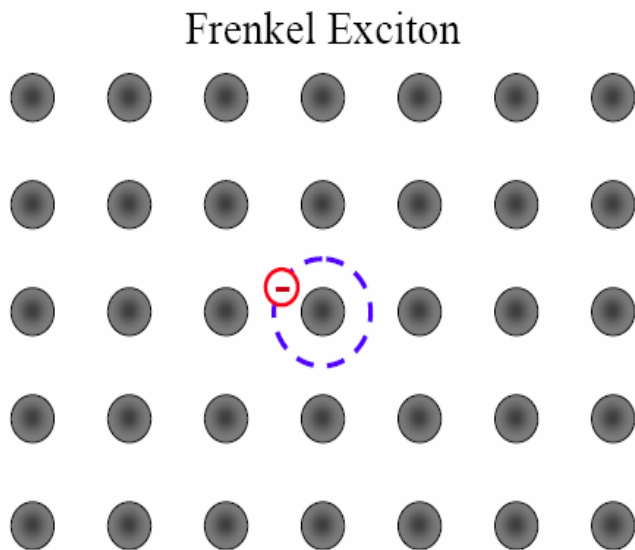


Figure 40 Schematic representation of Frenkel exciton.

Wannier Excitons: In the case of Wannier excitons the lattice atoms act as a background field in which electron and hole exist as free pair. The bound pair is formed by electron and hole orbiting each other on this background. The distance between electron and hole is much larger than the lattice constant of the system. In this weakly-interacting system for which the background also is very important, one has to take into account the effective masses of electron and hole as well as the dielectric constant of the material.

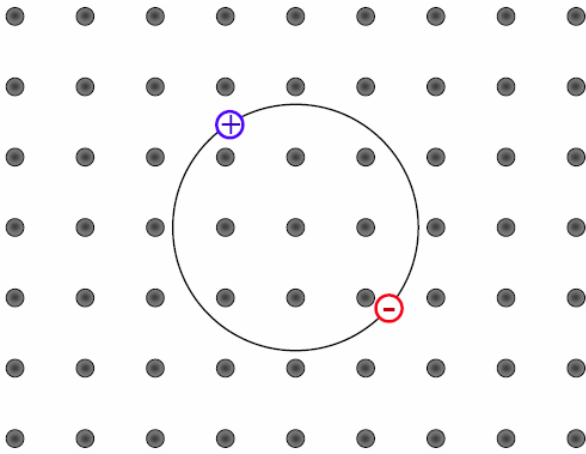


Figure 41 Schematic representation of a Wannier exciton.

Excitons in Au chains -- Infinite Au chains with zig-zag structure are semiconducting. In our studies, the vertical distance between two atoms is fixed at 2.89\AA and the horizontal distance is 5.006\AA (Fig.42).

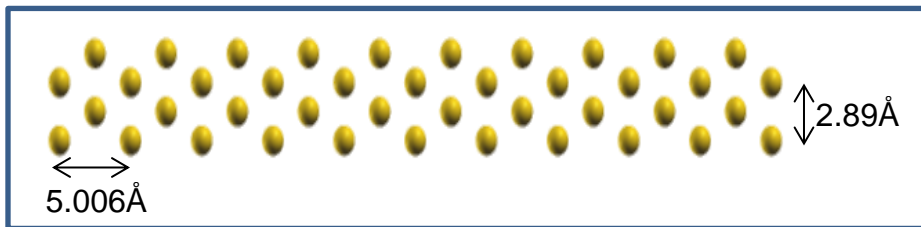


Figure 42 Schematic of the Infinite zig-zag chain.

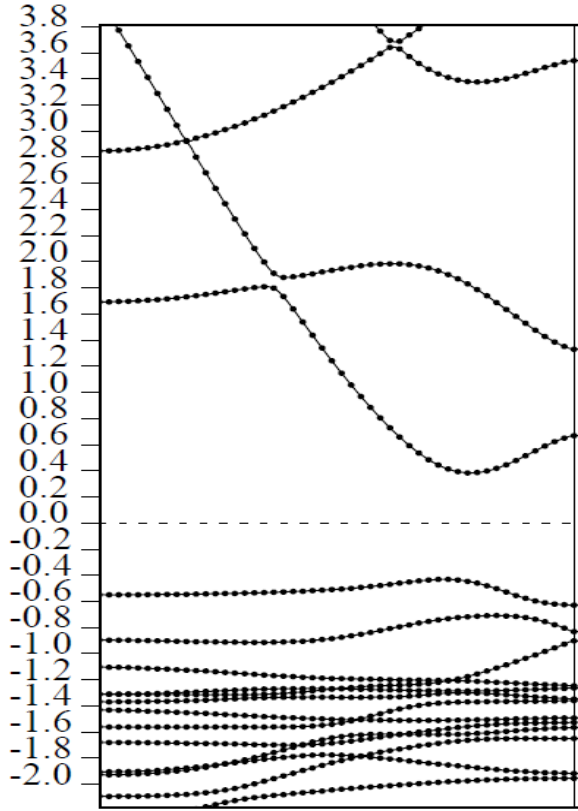


Figure 43. Band structure for infinite zig-zag chain

The exciton binding energy for infinite chain is calculated using different exchange and exchange-correlation potentials by using the TDDFT⁶⁷. We found that exciton binding energy is very sensitive to the choice of potential used. We have considered local, LDA and Slater potentials where we have added just exchange or exchange and correlation both and the results are tabulated in Table 1.

$$f_x^{LDA}(r, r') = -[9\pi n_o^2(r)]^{-\frac{1}{3}}\delta(r - r') \quad (127)$$

$$f_x^{local}(r, r') = -A\delta(r - r') \quad (128)$$

$$f_x^{slater}(r, r') = - \frac{2 \left| \sum_{jk} \theta(\epsilon_F - \epsilon_{jk}) \psi_{jk}(r) \psi_{jk}^*(r') \right|^2}{|r - r'| n_o(r) n_o(r')} \quad (129)$$

Table 1. Exciton binding energy for infinite zig-zag chain with different TDDFT potentials.

Potential	Exciton Binding energy(meV) [Exchange]	Exciton Binding energy(meV) [Exchange- Correlation]
Local	0.461	1.490
LDA	0.636	1.670
Slater	1.271	2.317

As it follows from our calculations, the binding energy is in ranges of meV, which means that the exciton excitation energy is not very different from the gap value, ~0.8eV, close to the plasmon energy in the finite chains.

3.2.2 Exciton Plasmon Energy Transfer

The advantages of nanomaterials are not limited to controllable optical properties of single components and potentially synergistic properties caused by interactions between the nanoscale constituents. Exciton-plasmon interaction allows one to design system properties such as emission and absorption. It also gives control over energy transfer processes at the nanoscale and creation of new excitations. Exciton plasmon interactions can be very strong as both the building blocks and the separation between the components have nanoscale dimensions. The number of possible hybrid materials that can be built from existing nanostructures is enormous; therefore, the potential for creating highly functional hybrid materials that enable, modify, and control energy processes and pathways is very promising. An important mechanism of such interaction is fluorescence resonance energy transfer (FRET) or Forster Energy Transfer^{67, 68}. This transfer mechanism provides a very efficient coupling between optically excited systems because it comes from Coulomb interaction between nanostructures. The fundamental optical excitations are transitions between these discrete levels in the conduction and valence bands that in particular lead to the formation of bound electron-hole pairs or excitons. The equivalents in metal nanostructures are so-called plasmons that are collective oscillations of conduction band electrons. Typically the exciton energy flows from large bandgap nanocrystal (donor) to a nanocrystal with smaller band gap (acceptor). Interactions between excitons and plasmons occur when metal and semiconductor nanostructures are in close proximity and they are often described by the coupling of the exciton dipole with the electromagnetic (also dipole) field of the

plasmons. This model has been used to explain the original experiments by Drexhage⁶⁹ who studied the change of the excitation decay rate of an emission dipole in the proximity of a plane metal surface. In general, well known phenomena including enhanced absorption cross-sections, increased radiative rates, and exciton-plasmon energy transfer⁷⁰ are described in the weak coupling regime. The challenge remains to properly calculate the electromagnetic fields in the proximity of metal nanoparticles. Such interactions have been studied in quantum dots^{71, 72}, nanowires⁷³ etc. We model a semiconductor –metal system, where infinite Au chains are semiconducting and finite chains are metallic. The excitons in the infinite chains transfer energy to Au nanochains to generate plasmon in them. FRET between the excitonic and plasmon states in coupled chain-wire system takes place on the femto-second time scales. Such a transfer might be used to manipulate the absorption and emission spectra of technological devices based on these systems. This opens up also a possibility for coupled excitations that can act differently than the optical excitations of the individual components.

3.2.2.1 Computational Details

When these wires are coupled with nanochains the Coulomb interaction between the wire and the chain electrons and the holes may lead to a non-radiative energy transfer. The process of energy transfer can be described as a transition between two states

$$(D^*, A) \xrightarrow{k_T} (D, A^*), \quad (130)$$

where D^* (D) is the donor in the excited (unexcited) state, A^* (A) is the acceptor in the excited (unexcited) state, and kT is the rate of resonance energy transfer between the donor and acceptor pair. In this process, the donor absorbs an external photon leaving it in an excited state. Then, the donor transfers its excited energy, via a non-radiative process, to the acceptor leaving it in an excited state. From Förster's theory [29], the rate of energy transfer from a donor to an acceptor $kT(r)$ is given by

$$k_T(r) = \frac{1}{\tau_D} \left(\frac{R_0}{r} \right)^6, \quad (131)$$

where, τ_D is the decay time of the donor in absence of acceptor, R_0 is the Förster distance, and r is the donor-to-acceptor distance. The efficiency of the energy transfer (E) is the fraction of photons absorbed by the donor which are transferred to the acceptor:

$$E = \frac{k_T(r)}{\tau_D^{-1} + k_T(r)} \quad (132)$$

It can be shown that the equation above corresponds to:

$$E = \frac{R_0^6}{R_0^6 + r^6}. \quad (133)$$

Therefore, the efficiency of such transfer between the systems separated by distance r is proportional to $1/r^6$.

Nanowire –nano chain system is described by the local environment around them i.e. by the dielectric constants of the nanowire, nanochains and substrate ϵ_{NW} , ϵ_{NC} , ϵ_0 . The local dielectric constant approach provides us with reliable description if the transferred

exciton energy is not very close to the band gap of the semiconducting wire. The formalism is based on the multipole expansion and fluctuation-dissipation theorem. We have used two-band model to calculate the exciton binding energy⁷⁴ using different XC kernels. The rate of energy transfer can be calculated as

$$\gamma_{\alpha}(\omega_{exc}) = \frac{2}{\hbar} \text{Im} \left[\frac{\varepsilon_{NC}(\omega_{exc})}{2\pi} \right] \int dV \vec{E}_{\alpha} \cdot \vec{E}_{\alpha}^*, \quad (134)$$

where ω_{exc} is the exciton frequency and \vec{E}_{α} is the electric field induced by the dipole field of the exciton, given by the gradient of the potential

$$\Phi_{\alpha} e^{-i\omega t} = \frac{e d_{exc}(\vec{r} - \vec{r}_{NW}) \hat{\alpha}}{\varepsilon_{eff} |\vec{r} - \vec{r}_{NW}|^3} e^{-i\omega_{exc} t}, \quad (135)$$

d_{exc} is the dipole moment of the exciton and $\hat{\alpha}$ is the direction of optical dipole moment

$$d_{exc} = \frac{1}{\Omega} \int \psi_k^c(r) \vec{r} \psi_q^v(r) dr, \quad (136)$$

$$\varepsilon_{eff} = \frac{2\varepsilon_0 + \varepsilon_{NW}}{3}, \quad (137)$$

\vec{r}_{NW} is the position of the nanowire and \vec{r} covers the entire space where the plasmon charge cloud could be present. The dielectric constant of the nanochains was calculated using the oscillator model:

$$\varepsilon_{NC}(\omega) = 1 - \frac{\omega_0^2}{2\sqrt{\omega_0^2 - \mu^2}} \left(\frac{1}{\omega - \sqrt{\omega_0^2 - \mu^2} + i\mu} - \frac{1}{\omega + \sqrt{\omega_0^2 - \mu^2} + i\mu} \right), \quad (138)$$

ω_0 is the resonance frequency, or the plasmon frequency. μ is the damping put equal 0.025.

3.2.2.2 Results

As it was shown above, finite Au chains have collective excitations and when they are doped with TM atoms additional local excitations are seen in the absorption spectrum. We analyse how these local and collective excitations interact with the excitons in the infinite semiconducting Au wires. We fix number of atoms in chain to be 14 and consider four different cases: Au₁₄ chain, Au₁₃Ni, Au₁₃Fe, Au₁₃Rh. The absorption spectra calculated using equation 95 for all of these cases are shown in Fig.44-47. The finite chain with 14 atoms have plasmons as shown above (The absorption spectra of 14 atom Au chain is shown in Fig.44). The plasmon peak is at 0.85eV so that plasmon energy and the gap of the infinite chain are comparable.

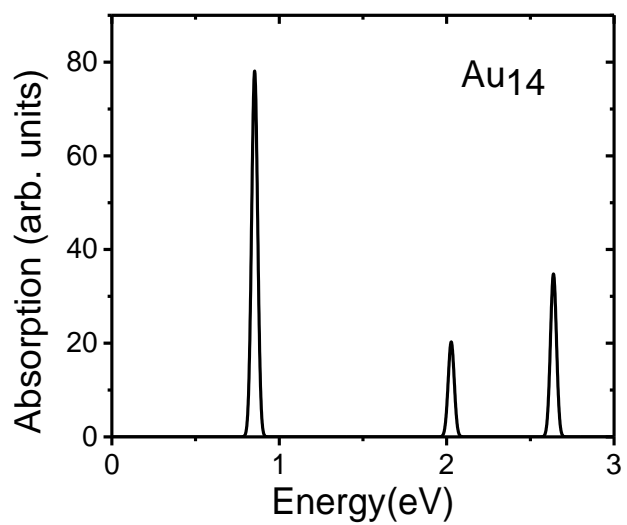


Figure 44. Absorption Spectra of pure Au chains of 14 atoms.

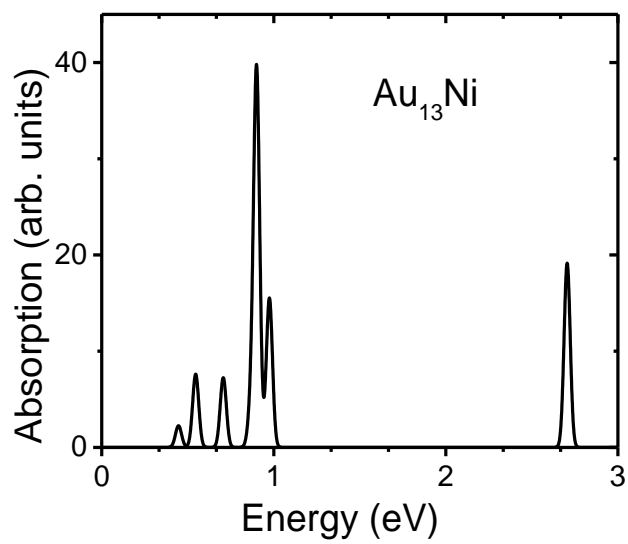


Figure 45 Absorption Spectra of Au₁₃Ni chain.

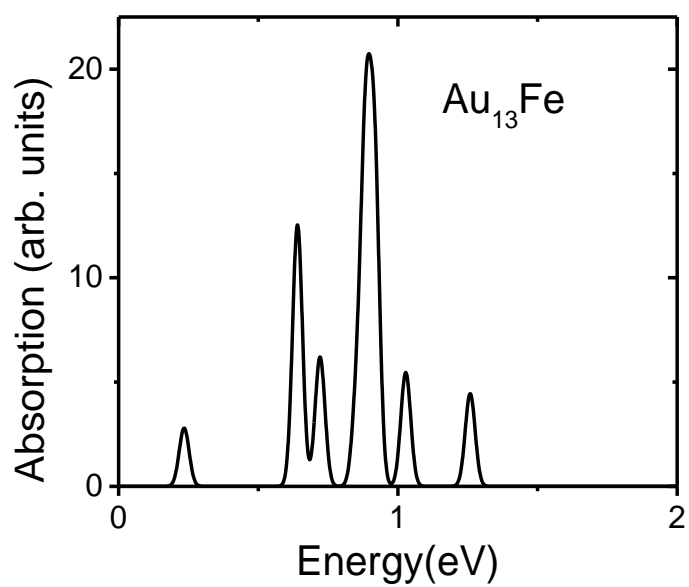


Figure 46 Absorption Spectra of Au_{13}Fe chain.

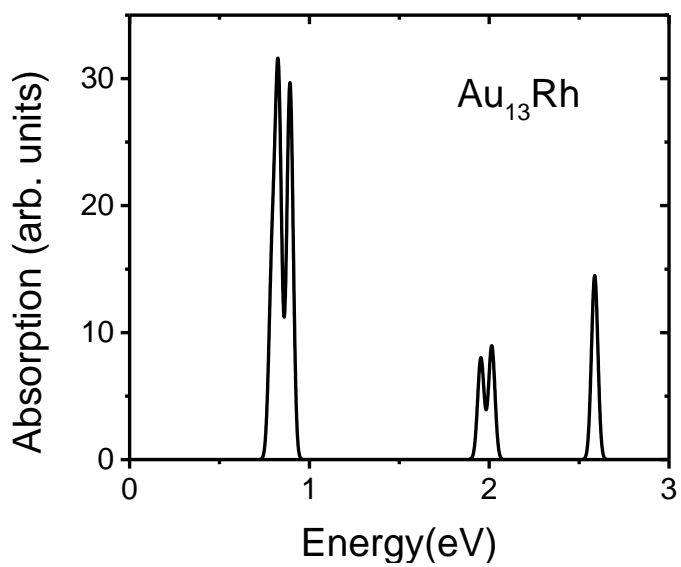


Figure 47. Absorption Spectra of Au_{13}Rh chain.

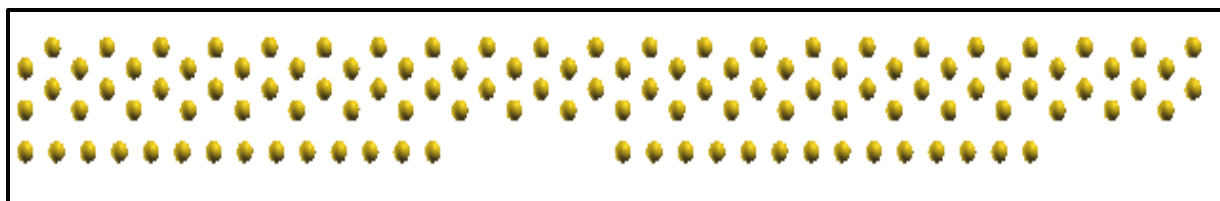


Figure 48. . Schematic of the Infinite zig-zag chain with finite Au₁₄ chain.

When the two chains, i.e the infinite and the finite chains, are brought together one can calculate the rate of energy transfer which is $9.3 \times 10^{11} \text{ s}^{-1}$, i.e. picosecond scale. When these chains are coupled with doped chains the exciton-plasmon coupling is enhanced because of the presence of local plasmons, so the transfer rate is substantially increased (in some cases by an order of magnitude), Table 2.

Table 2. The dielectric constant and rate of energy transfer (equation 131) for zig-zag chain and pure, doped chains of Au.

System	ϵ	$\Upsilon \times 10^{11} (1/s)$
Au	27.32	9.23
Au-Ni	59.39	20.0
Au-Fe	186.30	62.9
Au-Rh	127.13	42.9

This means that one can expect a possibility to manipulate the optical properties of the systems by changing the doping.

3.2.2.3 Discussion

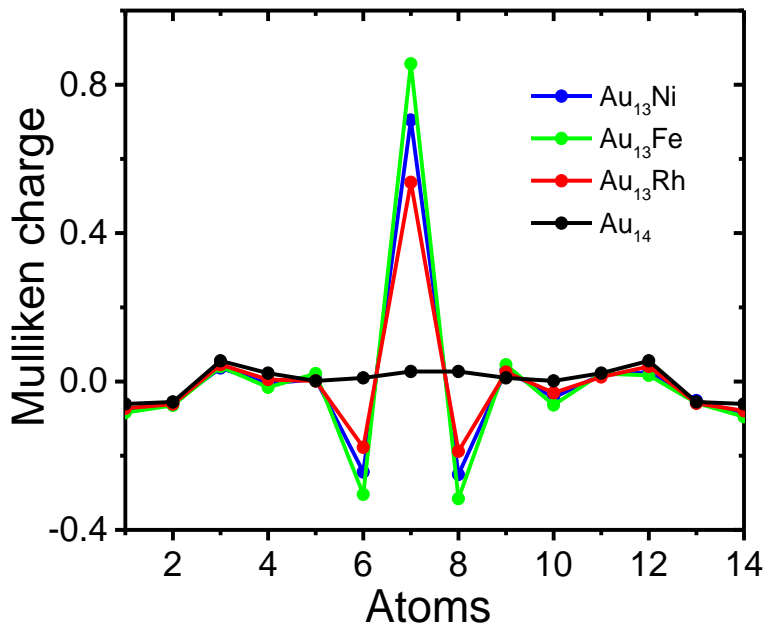


Figure 49. Mulliken Atomic charge of Au₁₄, Au₁₃Ni, Au₁₃Fe, Au₁₃Rh.

We have studied excitonic effects in the infinite semiconductor Au chains and effects of the exciton-plasmon interaction in coupled chains on their optical properties. In particular, we have found that the exciton binding energy in the chains can be significant, comparable to the values in other semiconducting materials⁷⁵. When the “excitonic” chains are coupled to the finite chains with plasmon excitations one can

expect an energy transfer between the chains. The effect is especially pronounced when the exciton and plasmon energies have close values and when hybridization between the excitations may occur. It was found that the largest transition dipole moment corresponds to the transfer between the exciton and local plasmon which is excited around the impurity atom. Thus, our results suggest that impurity atoms in the finite chain can be served as trapped centers for excitons. It may open a possibility to collect absorbed energy in particular spacial areas, with consequent local emission. For instance, very long semiconducting chains can be used to absorb the solar energy over a large area, while the created excitons travelling through the chains will be transformed into the local plasmons in the finite chains near the impurity atoms. This effect might have applications in solar cell technologies, for example in concentrators.

CHAPTER 4 ULTRAFAST EMISSION IN SINGLE LAYER MoS₂

Single layer MoS₂ shows a great potential to be used in novel nanoelectronics^{76, 77} and nano optical devices^{78, 79} and in catalysis. It's the tunable electronic structure of MoS₂ as well as strong absorption and emission makes it very attractive to be used in wide variety of applications like phototransistors⁸⁰, light emitting devices operating in visible region⁸¹. One of the important features of single layer MoS₂ is that it shows strong luminescence as opposed to its bulk counterpart^{82, 83}. The intensity of the emission decreases about 100 times as the number of layers increases to bulk value. This decrease in intensity has been attributed to the indirect band gap in the bulk MoS₂. Many experiments have reported photoluminescence in single layer MoS₂ and a great amount of work is being done in this field to understand the nature of the emission and absorption spectra^{83, 84}. Different experimental groups get different values of energy for the photoluminescence peak, the energy range varies from 1.8 -1.9 eV depending on the sample used^{82, 84}. To our knowledge there are no theoretical calculations for photoluminescence spectra that can give the insight on the reason for different results. We calculate the absorption and emission spectra of single layer MoS₂ and also study the role of electron phonon interactions on the peak position. There are evidences of strongly bound excitons⁸² and trions^{85, 86} in the optical absorption spectrum, so it is important to include exciton effects in the calculations. Tuning the bandgap in the single material makes MoS₂ a very promising material that can capture broad range of spectrum and also concentrate excitons and other charge carriers. The doped system

demonstrates high electron mobility. Study of the slow and ultrafast optical response of monolayer MoS₂ is important from the point of view of science and technological applications. It has been found that graphene which is also a single-layer material like MoS₂ shows strong emission when excited by ultrafast pulses²¹. It is very interesting to explore the ultrafast response of monolayer MoS₂ to ultrafast pulses, in particular its photoluminescence properties.

Photoluminescence is the emission of light which happens when the material is irradiated with some external light source. Phosphorescence and fluorescence are two different types of photoluminescence which differ from each other only by the emission time. Fluorescence is the prompt emission, i.e. the emission that occurs in the time range of microseconds after the excitation, whereas in phosphorescence the time scale is larger, of the order of milliseconds. When a material is irradiated by light, electrons are excited from valence band to conduction band. The lifetime of electrons in the conduction band is short because of various scattering processes like electron-electron scattering and electron-phonon interactions, which move electrons to the bottom of conduction band, which finally results in the transition back to the valence band and light emission. Electron-phonon interactions play a very important role in many processes in metals and semi-conductors, such as in electrical and thermal transport. In simpler picture, electron-phonon coupling alters the dispersion and lifetime of electronic states in the material. We have carried out first principles calculations of the photoluminescence properties of monolayer MoS₂ using DFT. We have tested our

approach by testing it on bulk Au and on graphane. In particular, we have analyzed the role of the electron-phonon interactions in the photoluminescence process. Phonon dispersion curves calculated using density functional perturbation theory served as the basis for the evaluation of the system electron-phonon coupling, which in turn was used to calculate the electron self-energy and the electron spectral function.

4.1 Computational Details

We have used QUANTUM ESPRESSO⁸⁷ code to calculate the ground state properties of monolayer MoS₂. We have used post processing software to calculate the electron-phonon coupling for semiconductors. The Quantum Espresso code uses the following steps to calculate electron-phonon coupling in metals. The ground state atomic and electronic configurations are obtained from usual DFT and then phonon spectrum is calculated using Density Functional Perturbation Theory. In order to know the electron-phonon coupling parameters, one has to determine the electron-phonon coefficient g which gives the probability of electron scattering from an initial electron state (i) with momentum \mathbf{k} to a final electron state (j) by a phonon with momentum \mathbf{q} and mode index ν :

$$g_{qv}(k, i, j) = \left(\frac{\hbar}{2M\omega_{qv}} \right)^{1/2} \left\langle \psi_{i,k} \left| \frac{dV_{SCF}}{d\hat{u}_{qv}} \cdot \hat{\epsilon}_{qv} \right| \psi_{j,k+q} \right\rangle, \quad (139)$$

where M is the atomic mass, $\psi_{i,k}$ and $\psi_{j,k+q}$ are the electronic wave functions for the initial and final states, respectively. $\frac{dV_{SCF}}{d\hat{u}_{qv}}$ is the gradient of the self-consistent potential with respect to the atomic displacements induced by the phonon mode (\mathbf{q}, ν) with frequency ω_{qv} and phonon polarization vector $\hat{\epsilon}_{qv}$.

The phonon line width is defined as

$$\gamma_{qv} = 2\pi\omega_{qv} \sum_{ij} \int \frac{d^3k}{\Omega_{BZ}} |g_{qv}(k, i, j)|^2 \delta(e_{q,i} - e_F) \delta(e_{k+q,j} - e_F), \quad (140)$$

and the electron-phonon coupling constant for mode ν and wave vector q is given by

$$\lambda_{qv} = \frac{\gamma_{qv}}{\pi\hbar N(e_F)\omega_{qv}^2}, \quad (141)$$

where $N(e_F)$ is the electron DOS at the Fermi level. It can be seen from the equation above that the electron-phonon coupling constant depends on the DOS at the Fermi level and that is why the codes fail to calculate it in the case of semiconductors where this parameter is zero. To avoid this problem, in the case of our semiconducting system we have manually shifted the Fermi level to a point where we have some finite DOS. This is equivalent to introducing doping in the system. The effectiveness of phonons with energy $\hbar\omega$ to scatter electrons is expressed in terms of the Eliashberg function $\alpha^2F(\omega)$. When the initial electron energy and momentum are fixed, the corresponding state-dependent Eliashberg function gives the e-ph coupling between the initial state and all other final states, which differ in energy by $\hbar\omega$ (due to the phonon emission (E) or absorption (A) processes). The Eliashberg function is defined as

$$\alpha^2 F(\omega) = \frac{1}{2\pi N(e_F)} \sum_{qv} \delta(\omega - \omega_{qv}) \frac{\gamma_{qv}}{\hbar \omega_{qv}}. \quad (142)$$

The coupling λ can also be defined as the first reciprocal momentum of the Eliashberg function

$$\lambda = \sum_{q,v} \lambda_{qv} = 2 \int \frac{\alpha^2 F(\omega)}{\omega} d\omega \quad (143)$$

To study the absorption and emission properties, one can calculate the spectral function $A(k, \omega)$, which is proportional to the probability of finding an electron with energy $\hbar\omega$ and momentum k in the given state (occupied or excited) and is given by

$$A(k, \omega) = \frac{|Im \Sigma(k, \omega)|}{[\omega - E^0(k) - Re \Sigma(k, \omega)]^2 + [Im \Sigma(k, \omega)]^2}, \quad (144)$$

where $E^0(k)$ is the band dispersion in the absence of interactions, $\Sigma(k, \omega)$ is the complex self-energy that include all many-body interaction effects. The real part of the self-energy renormalizes the dispersion and the states acquire a finite lifetime through the finite imaginary part. The imaginary part of the electron self-energy due to phonon scattering in the lowest-order approximation is related to the Eliashberg function through the integral over all the scattering events that conserve the energy and the momentum:

$$2Im\Sigma(\epsilon_i, k; T) = 2\pi \int_0^{\omega_{max}} \{ \alpha^2 F^E(\epsilon_i, k; \omega) [1 + n(\omega) - f(\epsilon_i - \omega)] + \alpha^2 F^A(\epsilon_i, k; \omega) [n(\omega) + f(\epsilon_i + \omega)] \} d\omega \quad (145)$$

In the last equation, f and n are the Fermi and Bose distribution functions, respectively.

The term in the first square bracket represents the phonon emission and the term in the second square brackets is associated with the phonon absorption processes

In the quasi-elastic approximation:-

$$2\text{Im}\Sigma(\epsilon_i, k; T) = 2\pi \int_0^{\omega_{max}} \alpha^2 F^E(\epsilon_i, k; \omega) [1 - f(\epsilon_i - \omega) + f(\epsilon_i + \omega) + 2n(\omega)] d\omega, \quad (146)$$

$$\text{Re}\Sigma(E, T) = \int_{-\infty}^{\infty} d\nu \int_0^{\omega_{max}} d\omega' \alpha^2 F(E, \omega') \frac{2\omega'}{\nu^2 - \omega'^2} f(\nu + E). \quad (147)$$

4.2 Results

As explained above, the electron-phonon coupling in the case of semiconductors is calculated by shifting the Fermi level; which actually corresponds to introducing some doping in the system. This practically is the case for many experiments in which the sample is inevitably doped. To test our approach, we first use the system of graphane (fig.50) where we calculate electron-phonon coupling as a function of doping, the results for which are known⁸⁸. Our results are in good agreement with Savini et. al.⁸⁸, which suggests that our approach is reliable. The structure for graphane was relaxed and the lattice parameters are given in Table 3. The doping in this case corresponds to hole doping.

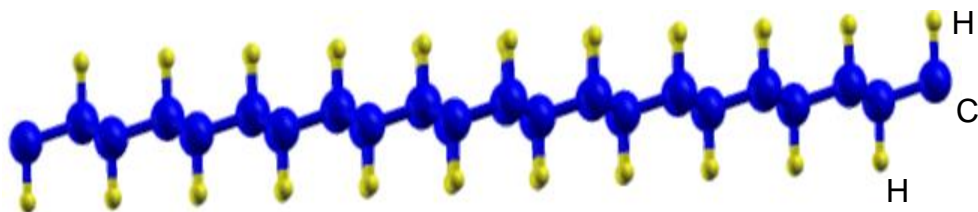


Figure 50 Schematic representation of graphane

Table 3 Lattice parameter and bondlength for graphane obtained by different approaches.

	Our calculations	Savini et. al.⁸⁸
Lattice Parameter	2.53	2.50
C-C bond length	1.53	1.51
C-H bond length	1.10	1.11

The density of states is also in agreement with other calculations (Fig.51). The band gap of graphane is 3.5eV as calculated by previous studies.

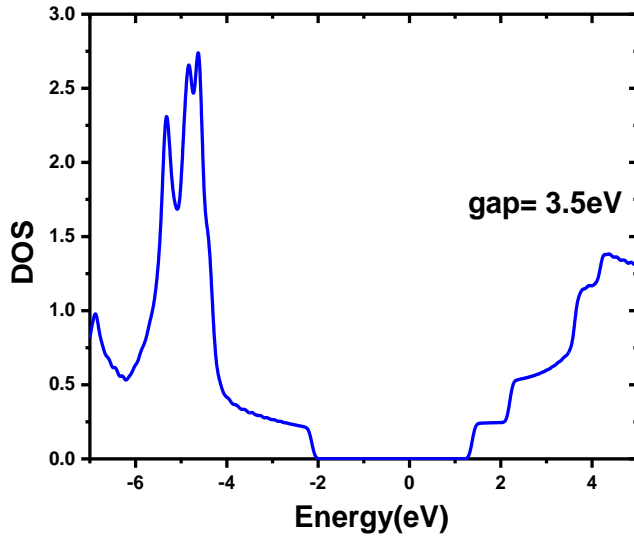


Figure 51. Density of states of pure graphane.

Table 4. Electron-phonon coupling constant in graphane as a function of doping.

Doping	λ	λ (Ref ⁸⁸)
2%	1.13	1.25
4%	1.25	1.37
10%	1.43	1.44

Furthermore, it can be seen from the Table 4 that the electron-phonon coupling constant is in very good agreement with other calculations and varies with the amount of hole doping.

Therefore, we applied the similar approach, mentioned above to single layer MoS₂ (Fig. 52). The single layer MoS₂ has two planes of hexagonally arranged Sulphur atoms which are bonded to hexagonal Mo atoms through covalent bonds. The bulk structure is formed by when such single layers are held together through Vander wall's interaction. The lattice parameter was optimized within Local Density Approximation (LDA) with the energy cut off 60 Ry and the K pointy mesh15x15x1. The values for the lattice constant and the bond lengths are shown in Table 5 and are in reasonable agreement with experimental data^{89, 90}.

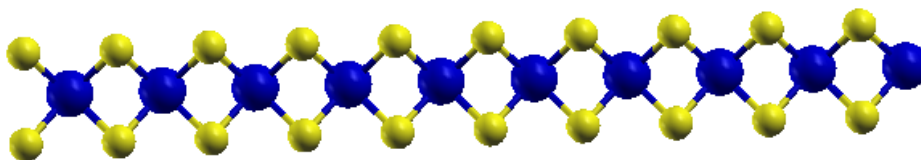


Figure 52 Schematic diagram of monolayer MoS₂.

Table 5 Lattice parameters for monolayer MoS₂.

	Our calculations	Experimental
a	3.167	3.16
Mo-S bond length	2.419	2.414

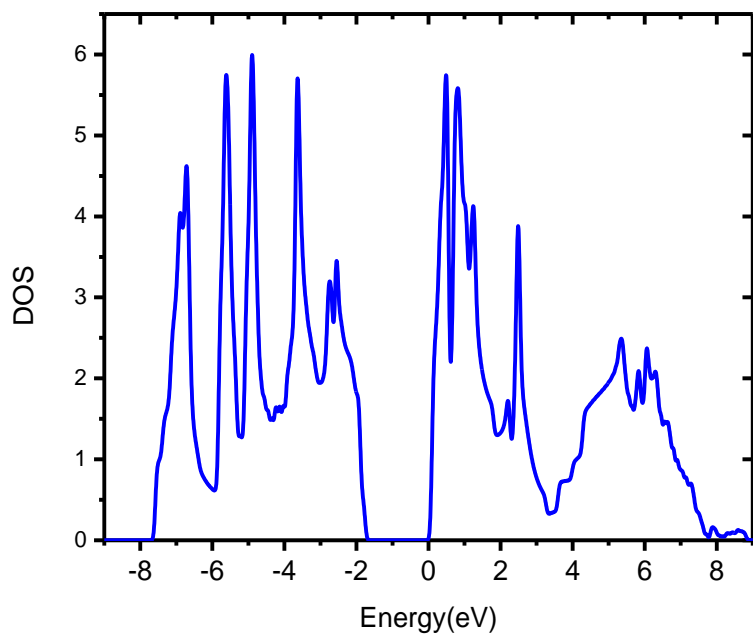


Figure 53 Density of states for single layer MoS₂.

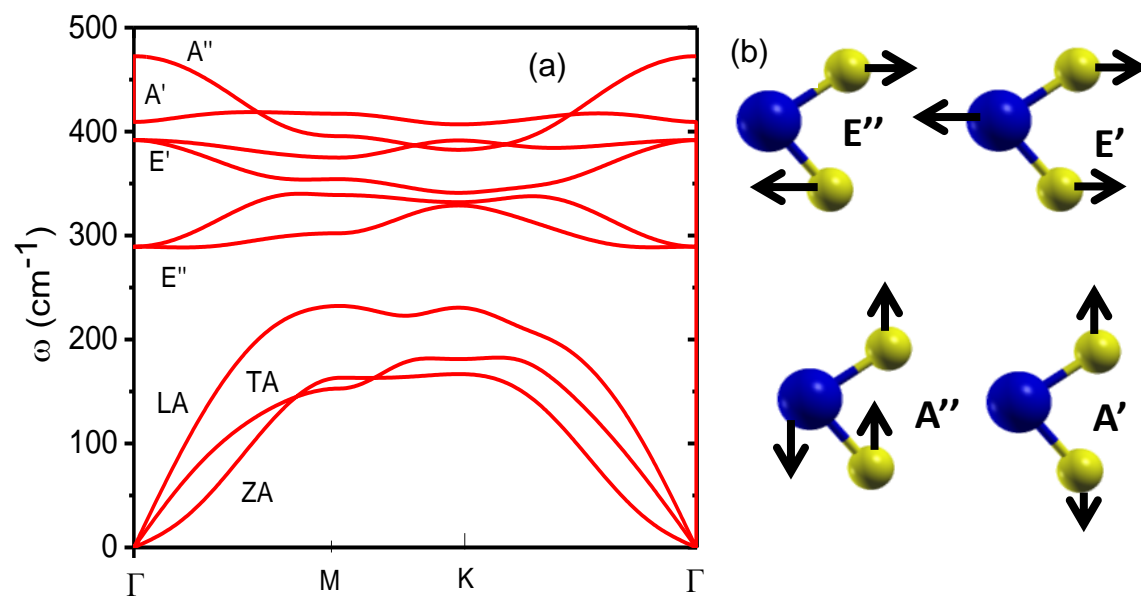


Figure 54 (a) Phonon dispersion curve for single layer MoS₂. (b) Schematic representation of the optical modes.

The electronic DOS shown in Figure 53 demonstrates the band gap of 1.8eV which is expected from DFT calculations⁹¹. GW calculations report band gap to be equal to 2.8eV⁹² and the experimental value is 2.15eV⁹³. Although LDA gives lattice parameters that agree well with experimental results the band gap is not correct. So, we will correct the band gap in order to get correct absorption spectrum.

Figure 54 shows the phonon dispersion of monolayer MoS₂. MoS₂ belongs to the symmetry point group D3h and has 9 branches of phonons, 3 acoustic and 6 optical. The acoustic modes LA and TA are the in plane vibration modes that have linear dispersion and they are higher in energy than the out of plane vibration mode ZA. The lower energy optical modes E' and E'' are in-plane vibrations and both are degenerate at the Gamma-point. Two E'' modes are in-plane vibrations with 2 sulphur atoms moving out of phase and Mo atom being static. The E' optical modes are polar modes with Mo and S atoms moving out-of-phase with respect to each other. A' is the homopolar mode with two sulphur atoms vibrating out-of-phase and Mo atom not moving and A'' is the highest energy optical mode with out-of-plane vibrations, where Mo and S atoms are vibrating out of phase with respect to each other.

The low-mode electron-phonon coupling is calculated with the same approach as for graphane (The Fermi level was shifted to a point where we get a finite DOS). The results of which are shown in Table 6.

Table 6 Electron-phonon coupling constant for different doping in monolayer MoS₂.

Doping	λ
1%	0.12
2%	0.16
3%	0.20

Shifting the Fermi energy to 0.067 eV corresponds to 1% electron doping. It gives $\lambda=0.12$, which is in the range expected by the previous studies⁹⁴. Once we obtain the electron-phonon coupling and the Eliashberg function, we calculate the real and imaginary parts of the self-energy (Figure 55). Then, using Equation (135) we calculate the spectral function, plotted in figure 56. The different curves in these plots represent the different values of chemical potential or Fermi energy (we have used an effective phonon frequency $\omega_E = 0.0497\text{ eV}$). The important point to note is that the imaginary part of self-energy equal to the inverse excitation lifetime $\tau(\omega) = -1/\text{Im}[\Sigma(\omega)]$ is small for frequencies around zero which means low scattering while for some other ω it is very large, which means fast phonon assisted relaxation and hence fast emission.

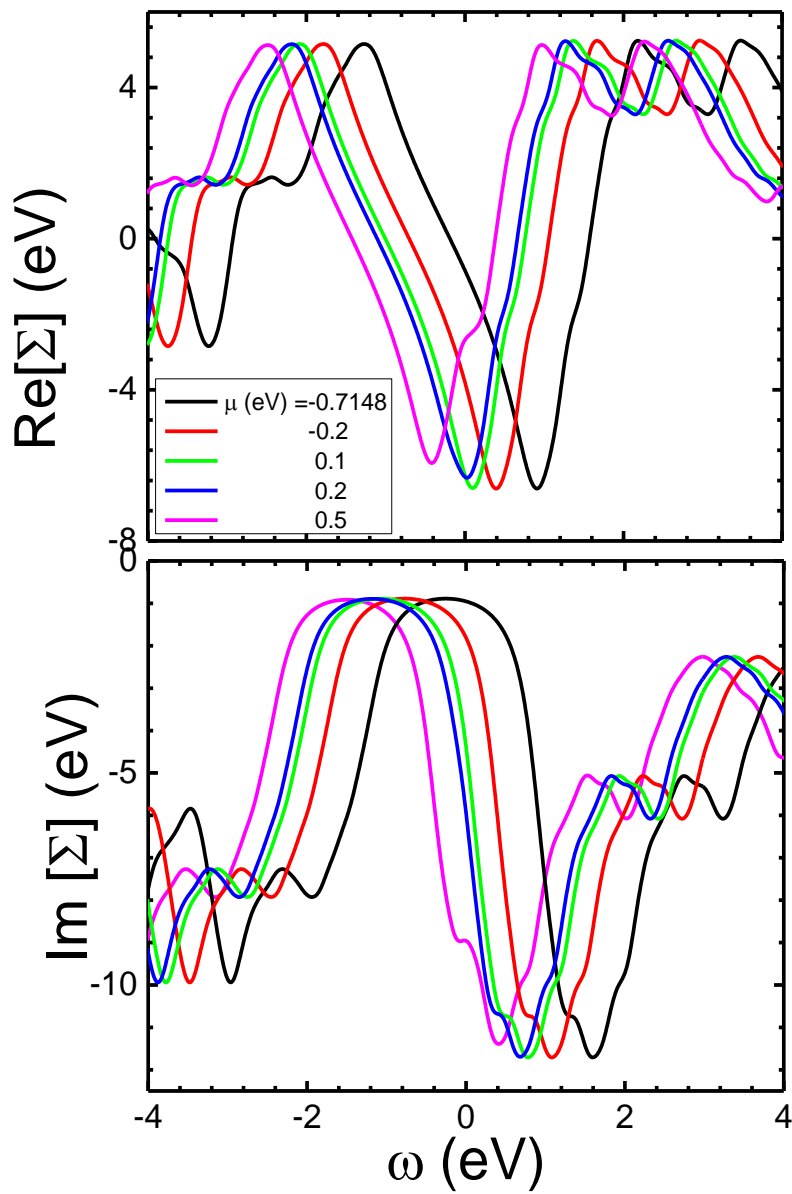


Figure 55 The Real and Imaginary part of the electron self-energy

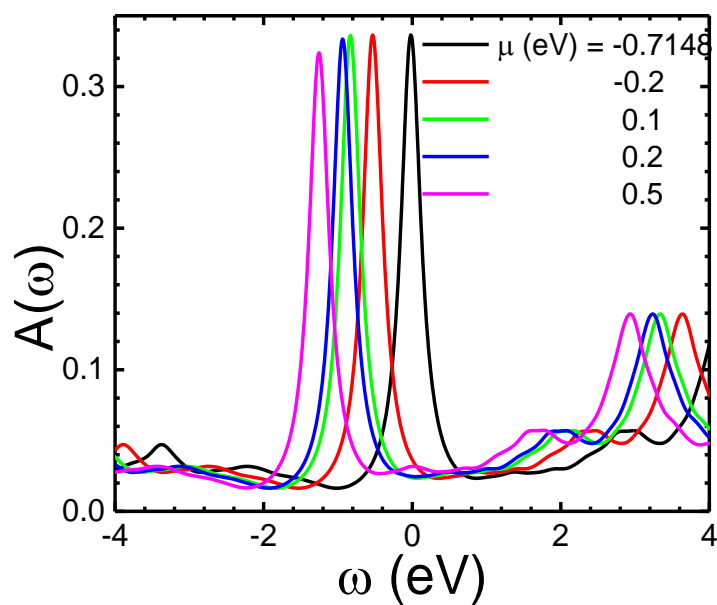


Figure 56 The spectral function of monolayer MoS₂.

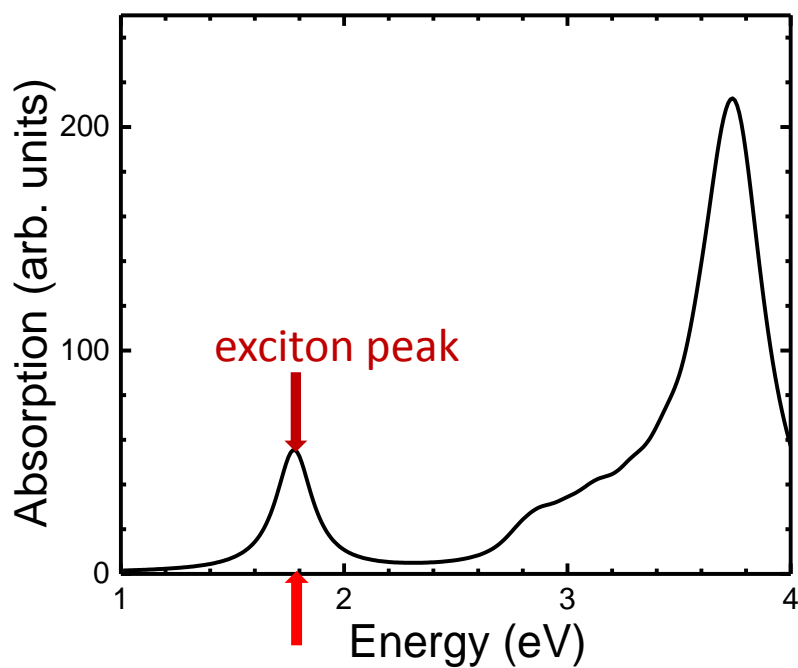


Figure 57 Absorption Spectrum of monolayer MoS₂.

The absorption spectrum was calculated using Equation (93). The absorption spectra shows two prominent features that correspond to the exciton transition from the valence band to the conduction band. Absorption spectrum demonstrates strong excitonic peak (binding energy $\sim 1\text{eV}^{86}$). In general, the system is optically active in the visible range. It is important to note that we have corrected DFT band gap to 2.8eV to get the absorption spectrum as presented above. Figure 58 shows the emission spectrum of monolayer MoS_2 . The PL peak for $\lambda=0.12$ coincides very well with the experimental value of 1.9eV . The exciton emission was also included into the spectrum, which gives results that are in very good agreement with the experimental data. It is evident from the PL spectrum the peak position depends on the electron-phonon coupling as the peak moves to higher energy as the value of λ increases and as expected the line width also increases with the value of λ .

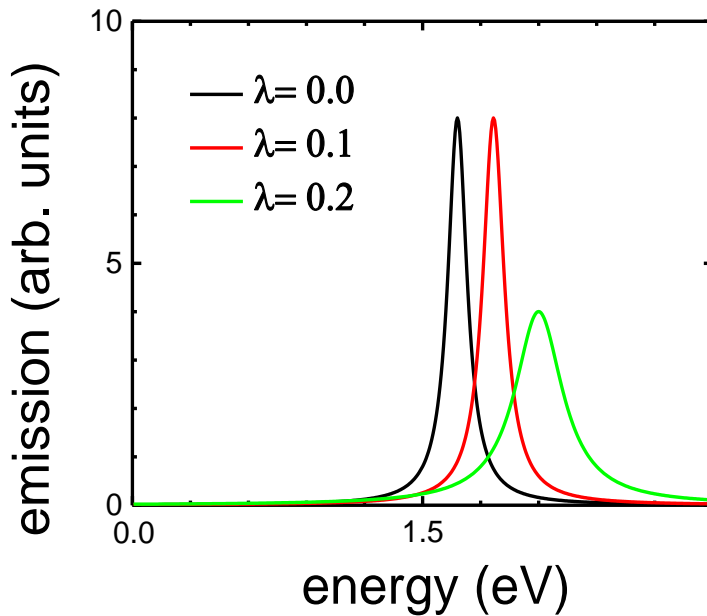


Figure 58 The photoluminescence spectrum of monolayer MoS_2 for different values of λ

To understand the behavior of system under ultrafast excitations we study the time dependence of the electronic temperature of doped MoS₂ calculated by (Allen model⁹⁵):

$$\frac{dT_e}{dt} = I(t) + \gamma_T(T_L - T_e), \quad (148)$$

where the rate is

$$\gamma_T = \frac{3\hbar\lambda\langle\omega_{ph}^2\rangle}{\pi k_B T_e}. \quad (149)$$

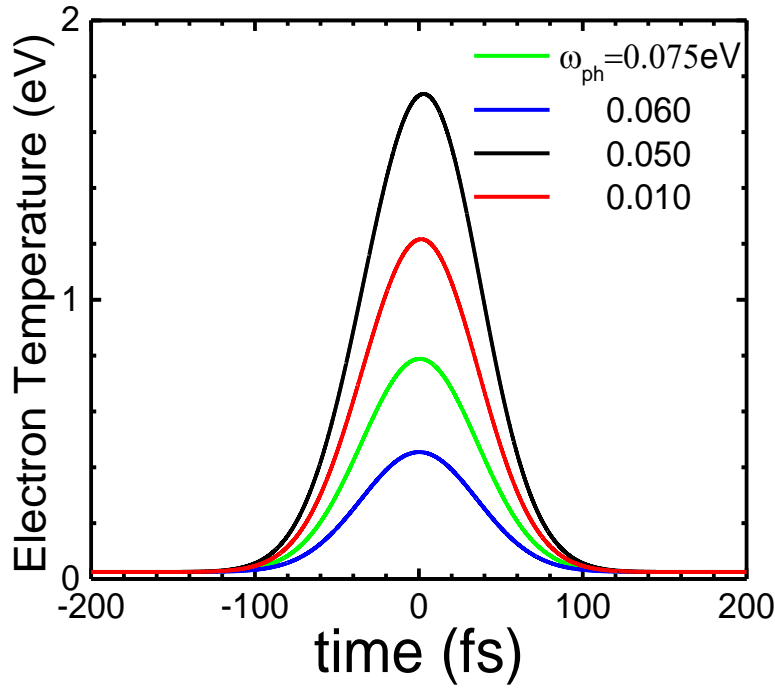


Figure 59 Time dependence of electron temperature in doped MoS₂.

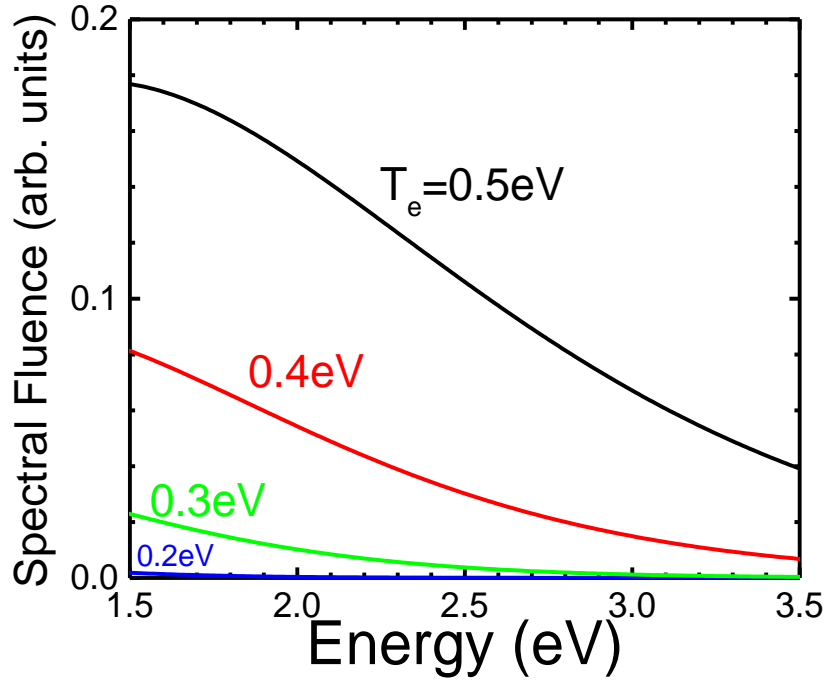


Figure 60 The Spectral fluence in doped MoS₂.

Figure 59 shows the result of the time dependence of electron temperature. Our calculations suggest that thermal relaxation of 100 fs-pulse excited MoS₂ electron system happens also on the fs scale. The corresponding fluence is shown in Figure 60. Spectral fluence is the total radiant energy emitted in all directions per unit area per photon energy. It is calculated using Planck-type formula

$$F(\omega, T) \sim \frac{\tau_{em} \varepsilon(\omega) \omega^3}{\left[e^{\frac{\omega}{T}} - 1 \right]}, \quad (150)$$

where the emission time τ_{em} is the time for which the laser pulse is applied was set to ~100fs, emissivity $\varepsilon \sim 0.1$ and $\omega = 0.05$ eV. It is clear from the Figure that in doped system

one can expect a high spectral fluence of visible light emission at high effective emission temperatures of the excited system in the femto-second timescale.

4.3 Conclusions

To summarize, we have calculated the optical response pure and doped monolayer MoS₂, including the ultrafast response. It was found that absorption spectrum demonstrates exciton peak in the visible range with binding energy $\sim 1\text{eV}$. Position of the emission peak of clean system is very sensitive to the value of e-ph coupling and also lies in the visible range. Calculations of the self-energy and spectral functions of the doped systems suggest that one can expect excitations with 10-100fs lifetime, which makes the system interesting to ultrafast applications. The position of the spectral peaks can be manipulated by doping in the visible range frequencies. The doped system demonstrates ultrafast (fs) relaxation of electronic subsystem when excited by fs pulses and a high ultrafast spectral fluence of visible light emission. These features might be also used in modern optical devices.

CHAPTER 5 MAGNETIC PROPERTIES OF NANOPARTICLES

5.1 AFM-FM Transition in Bulk Fe-Rh

There has been recent interest in bimetallic nanoalloys when non-magnetic metals or even insulators are embedded in magnetic 3d clusters (e.g. Fe, Co, Cr and Ni). The combination of 3d metals with large magnetic moment and 4d metals (e.g. Rh) with strong spin orbit coupling may be an effective way of obtaining a high magnetic moment and anisotropy which is required in high density magnetic recording. Fe-Rh systems are of special interest due to unusual AFM-FM transition in the bulk case. In 1938 Fallot discovered that ordered FeRh system undergoes a transition from AFM to FM²². This happens at about 370 K. Equiatomic Fe-Pt might be expected to show the same magnetic behavior but it remains FM at all temperature. At room temperature CsCl type structured alloy has zero net magnetic moment ; the Fe spins are antiferromagnetically ordered with $\pm 3.3 \mu_B$ while Rh spins donot exhibit any ordering. Upon heating beyond the critical temperature of about 340K , FeRh undergoes an isotropic lattice expansion and Fe as well as Rh spins are aligned ferromagnetically with Fe magnetic moment as $3 \mu_B$ and Rh as $1 \mu_B$. When the temperature is raised above the Curie temperature 740K the system undergoes second phase transition into a paramagnetic phase. Although the AFM –FM transition has been known for decades and numerous experimental and theoretical works has been devoted to this system^{23, 96-99}, the physical mechanism of this transition remains a matter of debate. While some studies suggest that electron gas entropy to be the driving force for this transition¹⁰⁰ while other suggest that non collinear

magnetic excitations and strong Fe-Rh hybridization could also be the reason for transition¹⁰¹. Gu et. al. suggest that the transition is caused by different magnon excitations of FM and AFM states⁹⁸ and Cooke¹⁰² et.al. show the role of magnetic fluctuations in AFM to FM transitions.

Starting with the bulk FeRh (50%-50%), we first try to reproduce the result obtained in all previous calculations i.e. to look at AFM-FM transition in the bulk. For that we have applied DFT studies using Quantum Espresso code and found that the system undergoes AFM-FM transition with increase of temperature, in agreement with experimental data. Experimental studies²² suggest that FeRh undergoes lattice expansion during the transition and this is the parameter that we have incorporated in our calculations. We changed the lattice parameter and found that system undergoes AFM-FM transition at 3.08Å.

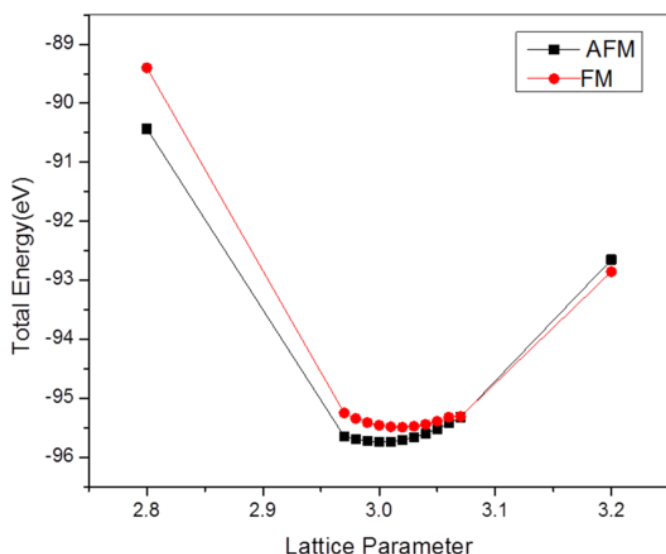


Figure 61. AFM –FM transition in bulk Fe-Rh. Transition takes place at $a=3.08\text{\AA}$

In this work our goal is to see if the basis of this transition may be found by examining FeRh nanoparticles. Particularly since for nanosystems it is easy to change the chemical composition which could possibly shed light on the nature of bulk FM-AFM transition and also possibility to tune the magnetic properties of this type of material.

5.2 Magnetism in FeRh Nanoparticles

Although the potential advantages of alloying 3d elements with highly polarizable 4d or 5d elements are easy to understand, the problem involves a number of serious practical challenges. Different growth or synthesis conditions can lead to different chemical orders, which can be governed not just by energetic reasons but by kinetic processes as well. For instance, one may have to deal with segregated clusters having a 4d core

and a 3d outer shell or vice versa. Moreover, the interatomic distances are also expected to depend strongly on size and composition. Typical TM-cluster bond lengths are in fact 10–20% smaller than in the corresponding bulk crystals. Taking into account that itinerant 3d-electron magnetism is most sensitive to the local and chemical environments of the atoms,^{26,37–39} It is clear that controlling the distribution of the elements within the cluster is crucial for understanding magnetic nanoalloys. So, it is important to understand the chemical composition, geometry and the cluster size-dependence of the magnetic properties of the corresponding nanoclusters. FeRh has been studied extensively in bulk and thin film forms^{96, 98, 103}. However, there is also interest in FeRh nanoparticles arising from potential applications in magnetic recording or sensor technologies, as well as fundamental interest concerning the relationships between size reduction and tailoring of the magnetostructural transition character. There have been contradictory results on AFM-FM transition in FeRh nanoparticles while Yu Ko^{104, 105} et. al. and Jia¹⁰⁶ et. al. reported an AFM-FM transition in these nanoparticles, while Hillion¹⁰⁷ et.al reports absence of such transition in smaller cluster sizes.

5.2.1 Computational Details

We have applied DFT as implemented in QUANTUM ESPRESSO⁸⁷ code to calculate the magnetization and total energy of the clusters. The exchange and correlation energy was approximated by using both the spin-polarized generalized-gradient approximation (GGA) with PBE²⁷ functional. The structures are obtained from cutting the bulk FM as

well as AFM ground state structures and then relaxing them. Different concentrations are obtained by just replacing the Fe or Rh atoms from 50-50 FeRh bulk structure.

5.2.2 Results

We studied different compositions for 26-atom nanoparticles of FeRh, namely $\text{Fe}_2\text{Rh}_{24}$, $\text{Fe}_{10}\text{Rh}_{16}$, $\text{Fe}_{14}\text{Rh}_{12}$, $\text{Fe}_{24}\text{Rh}_2$ (Fig.62). Table1 shows the total energy and total magnetization of these clusters. It is very clear that for all clusters the FM state is the lower energy state. The total magnetization increases with the number of Fe atoms in the cluster. Fe atoms have more magnetization $\sim 3\mu_B$ and Rh atoms in FM structure have magnetic moment more than $1.2 \mu_B$ and less than $0.9 \mu_B$ in the AFM case. The magnetic moment increases from 20-30% as the atom moves from inside to surface. We have also analyzed the bondlength expansion and contractions and even in that case the FM state was lower in energy than the AFM state.

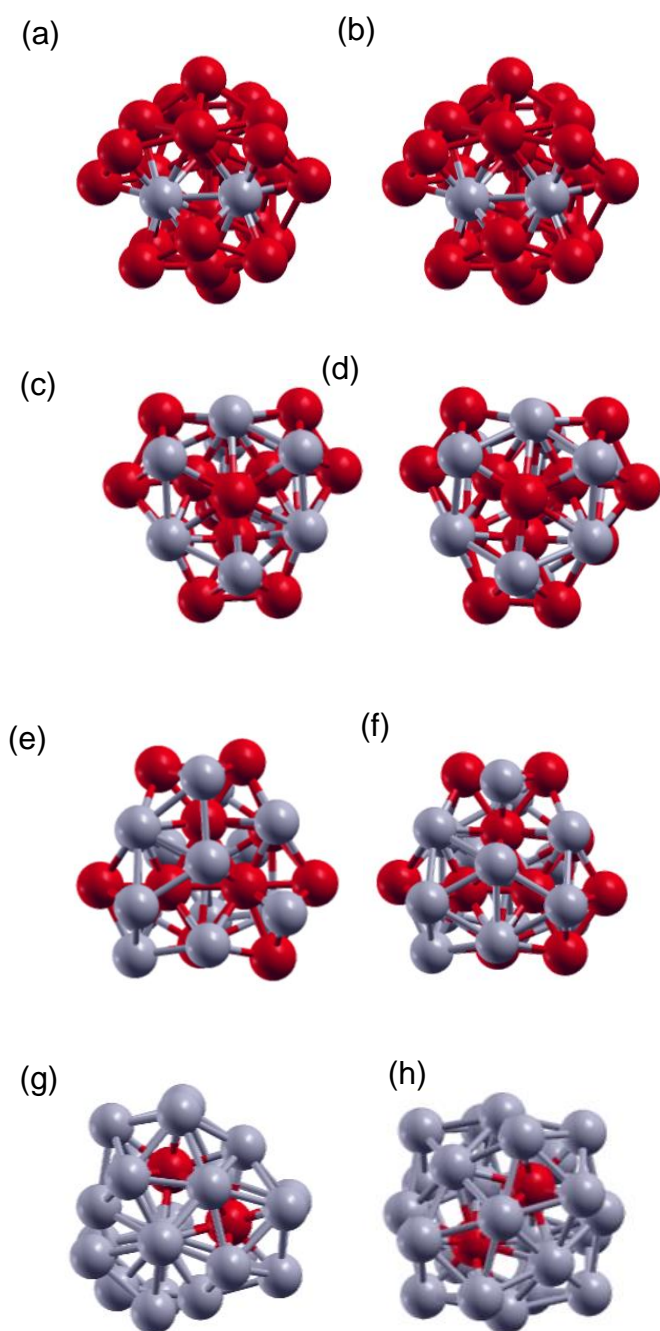


Figure 62. Optimized structures of $\text{Fe}_x\text{Rh}_{26-x}$: (a) FM $\text{Fe}_{24}\text{Rh}_2$, (b) AFM $\text{Fe}_{24}\text{Rh}_2$, (c) FM $\text{Fe}_{14}\text{Rh}_{12}$, (d) AFM $\text{Fe}_{14}\text{Rh}_{12}$, (e) FM $\text{Fe}_{10}\text{Rh}_{16}$, (f) AFM $\text{Fe}_{10}\text{Rh}_{16}$ (g) FM $\text{Fe}_2\text{Rh}_{24}$, (h) AFM $\text{Fe}_2\text{Rh}_{24}$

Table 7. Total Energy and total Magnetization of FM and AFM $\text{Fe}_x\text{Rh}_{26-x}$ nanoparticles.

Clusters	FM		AFM	
	Energy (eV)	Total Magnetization (μ_B/cell)	Energy (eV)	Total Magnetization (μ_B/cell)
Fe₂₄Rh₂	0	74.0	+4.02	2.0
Fe₁₄Rh₁₂	0	60.0	+1.75	0.0
Fe₁₀Rh₁₆	0	54.0	+1.44	6.0
Fe₂Rh₂₄	0	42.0	+0.12	0.0

The zero actually corresponds to the lowest energy value and the +sign shows that the AFM structures have this much energy more than the FM ones. The table clearly indicates that the FM structures are always lower in energy than AFM ones. Also the total magnetization of the cluster decreases with the number of Rh atoms as it should be as the magnetic moment of Rh atoms is less than Fe atoms. Another interesting thing to note is that the difference in energy between FM and AFM structure is also decreasing with increasing Rh atoms suggesting that Fe atoms are responsible for the stability of FM phase.

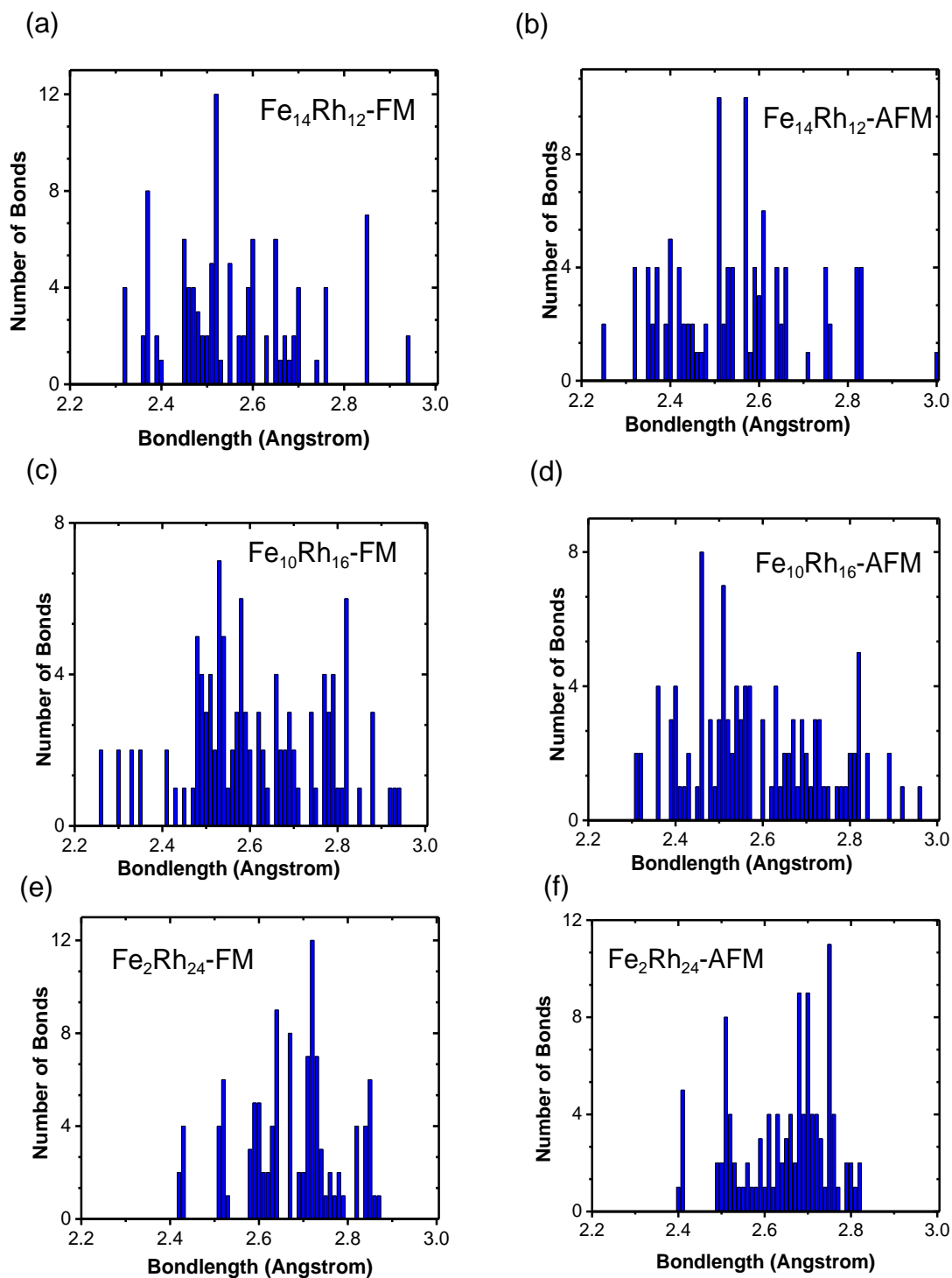


Figure 63 Bond length distribution of the structures shown above in Fig.62.

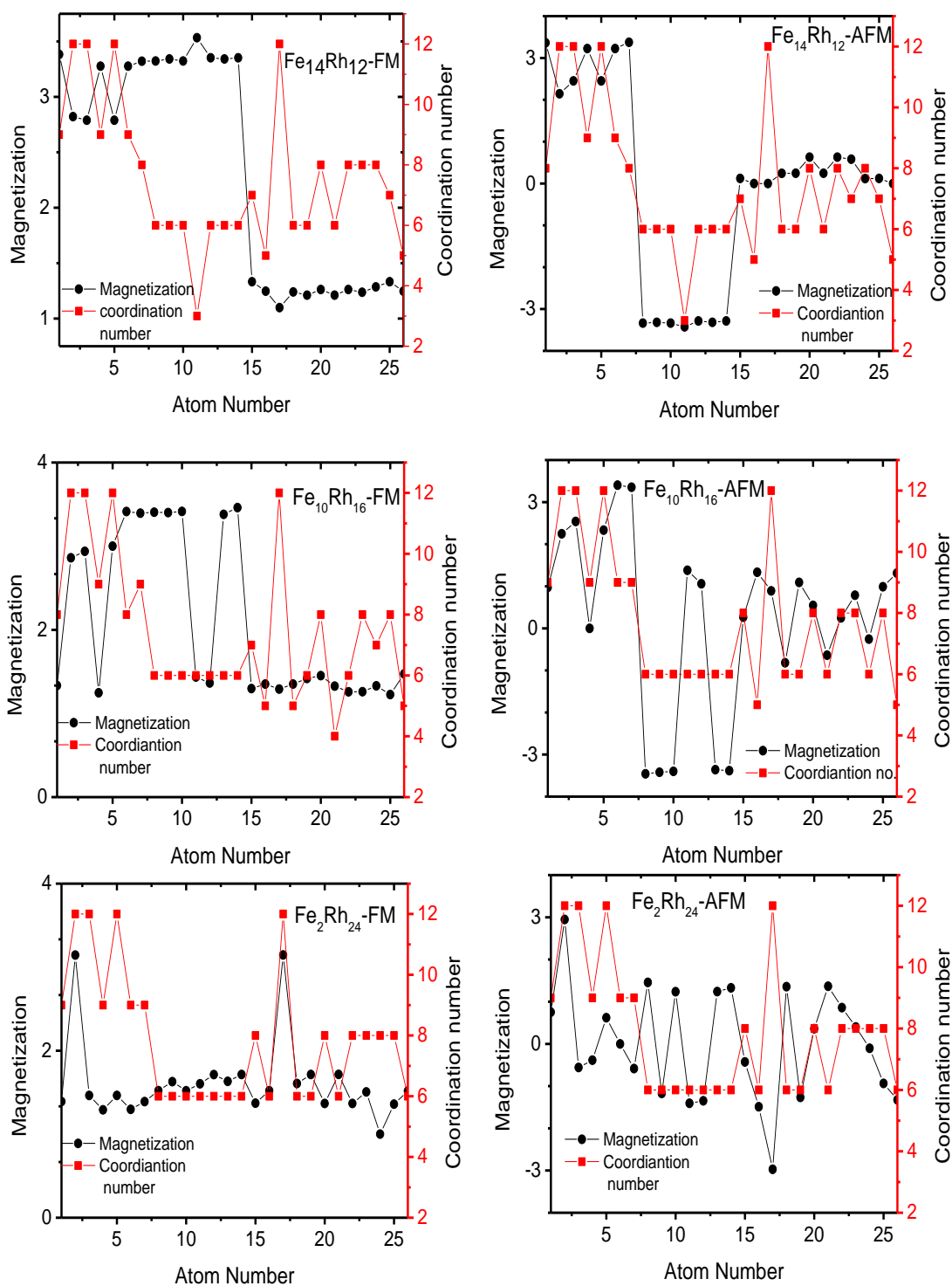


Figure 64. Magnetization/atom and coordination number for the clusters in fig.62.

We analyzed the bondlength distribution and coordination number in these clusters. Fig. 63 shows the bond length distribution in the clusters. For both Fe and Rh atoms, the bond lengths are distributed in the range 2.2 to 3.0 Å. In general, Fe-Rh bonds are shorter than Rh-Rh bonds and the bondlength distribution remains almost same for FM and AFM cases. Figure 64 shows the magnetization per atom and the coordination number of the atoms in the cluster. We find that more coordinated the Fe atom is the smaller is its magnetic moment. However, this condition does not necessarily hold for the Rh atoms as can be seen from figure 65 where an example of Fe₁₀Rh₁₆ FM case is shown. Fe atom no.9 and 13 with coordination number 6 is located outside the cluster and has relatively more moment (3.40 and 3.38 μB) than Fe atom no. 2 and 3 which lies inside the cluster and have coordination number 10 and magnetic moment 2.86 and 2.93 μB respectively. But for Rh atom, Rh21 is least coordinated (coordination number 3) and is surrounded by 3 Fe atoms but still its moment (1.32μB) is less than Rh26 (1.47μB) whose coordination number is more and is bonded just by Rh atoms. This can be explained by looking at the Partial Density of States (PDOS) for these atoms. Fig. 66 shows the PDOS of d orbital Fe atom no.2 and 13 which indicate that m4 moves to the occupied level for atom number 13 thereby giving more magnetization. However for Rh atoms the PDOS for the inner and surface atoms (1 and 22) does not differ much and hence the magnetization also does not differ.

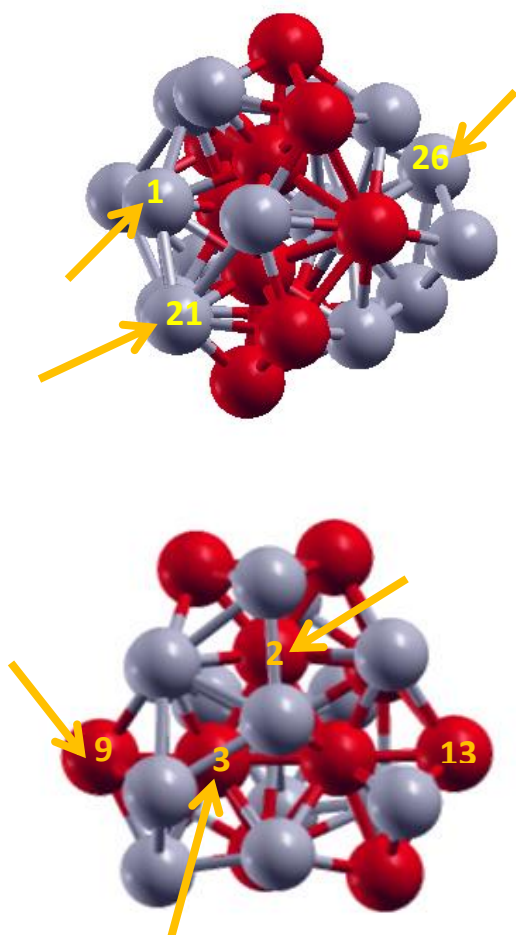


Figure 65 FM Fe₁₀Rh₁₆ (two figures are just different angles to show Fe and Rh atoms clearly)

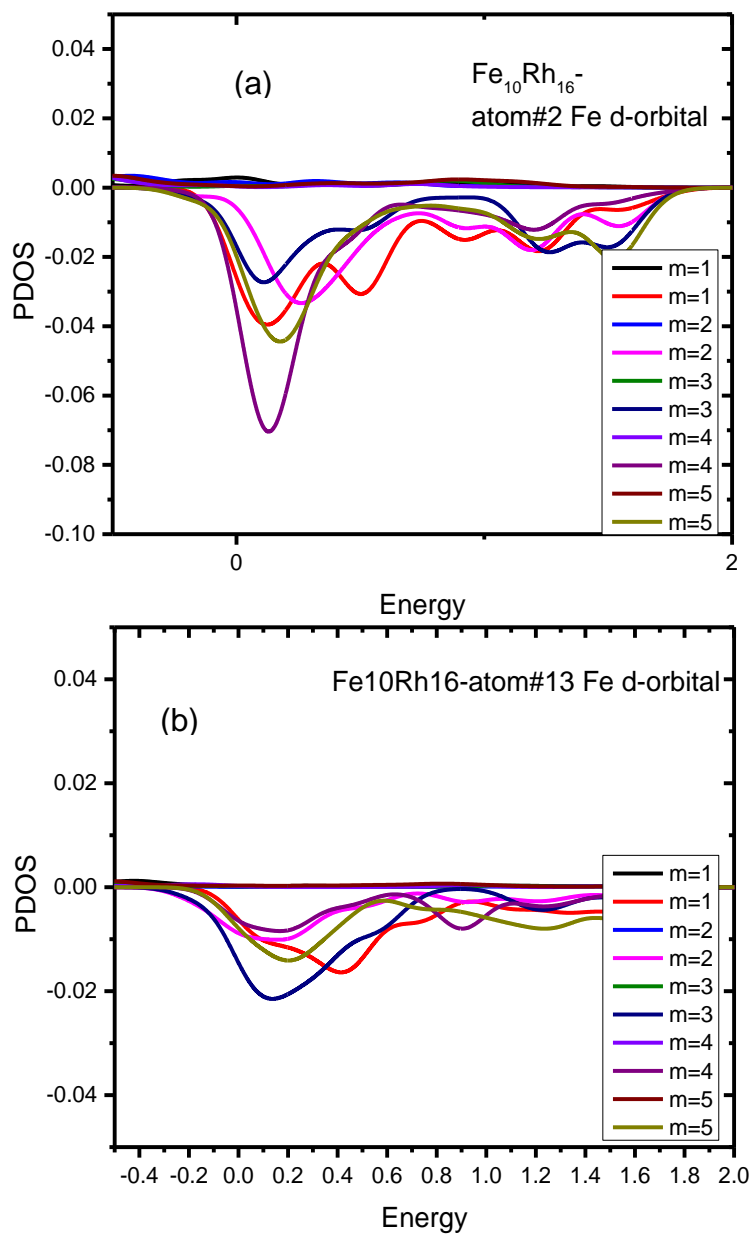


Figure 66 Partial DOS of d-orbital of Fe atoms shown in Fig.65 (a) atom number 2 (b) atom number 13

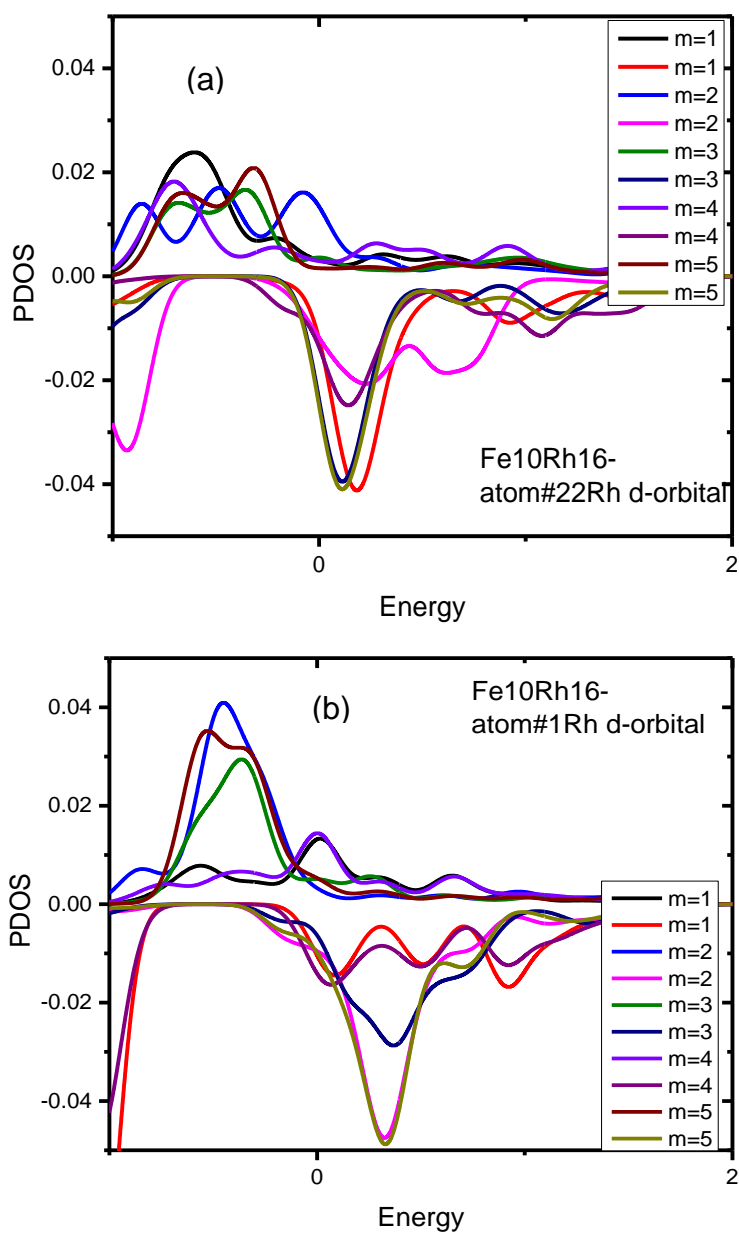


Figure 67 Partial DOS of d-orbital of Rh atoms shown in Fig.65 (a) atom number 22 (b) atom number 1

5.2.3 Conclusions

We found that FeRh nanoparticles behave very differently from their bulk counterparts and do not show AFM state as their ground state. We have analyzed various compositions and all of them are ferromagnetic. The magnetization per atom decreases with increasing number of Rh atoms, though not dramatically. Energy difference between the AFM and FM states becomes very small when cluster is close to pure Rh which means FM is mostly due to Fe states. The average bondlength increases with number of Rh atoms. There is correlation between the magnetization per atom and the position of Fe atoms (surface and bulk), i.e. coordination number. On the other hand this is not the case for Rh, which probably has magnetic moment due to stronger orbital localization. Thus manipulation of FM can be done by changing the number and the position of Fe atoms. These results also suggests that the FM-AFM transition in bulk might be caused by the Stoner mechanism, characteristic for extended solids, while in the finite clusters the magnetism is governed by Heisenberg exchange mechanism, which favors ferromagnetism in our case. Stoner mechanism is related to ferromagnetism, arising from the shift between the spin-down and spin up bands. The Stoner criterion describes the energy balance of the ferromagnetic order. The energy of the system can increase as a result of the (spin related) asymmetry of the dispersion relation and can decrease as a result of the Weiss field. The comparison of these energies gives the ferromagnetic order in the system. It is thus a many-body (band) effect. The Heisenberg mechanism, on the other hand is a local (inter site) spin interaction effect. By changing the distance between atoms and their environment the

coupling constant J can be changed from positive to negative, making the system ferromagnetic or antiferromagnetic ($H_{heis} = -2J_{ab}S_aS_b$). We have expanded the lattice constant of the cluster and found the FM state to be still the ground state i.e. the sign of J did not change implying there is no AFM-FM transition. On the other hand, we know that in the bulk the transition happens, which means that it is probably not due to the Heisenberg J change, but rather due to Stoner mechanism. We also found a nontrivial dependence of the magnetic properties on the chemical composition of the clusters, including rather strong magnetization of the Rh atoms.

CHAPTER 6 SUMMARY

In summary, I have studied optical and magnetic properties of several different types of nanostructures: chains, nanoparticles and atomic-thin monolayer, and found that these properties can be tuned by varying the system parameters, most notably the composition and size. Collective excitations were observed not only in noble metal-, but also in TM metal chains. In the case of TM-doped Au chains we found additional local modes. Similar behavior was observed in arrays of chains in which in addition to this effect the interaction between local and collective plasmons of the chains give rise to new peaks and broad spectra. It was shown that by increasing the number of chains in the array it is possible to tune the spectrum into visible range, a very important feature from the point of view of practical applications. In addition to plasmons, we studied a possibility of excitons and exciton-plasmon interaction effects in chain systems. It was shown that this interaction may lead to collective coupled modes, as well as to energy transfer between different excitations, especially pronounceable for the local plasmon modes. We also studied the optical properties of monolayer MoS₂, and the main result we found is a possibility of the ultrafast (fs) emission in this system under laser excitations. Finally, the magnetic properties of FeRh nanoparticles were analyzed. We found no indication of the AFM-FM transition, contrary to the bulk. It was shown that the magnetic properties of the system are very sensitive to chemical composition.

APPENDIX: ORBITAL DENSITY IN DOUBLE CHAINS

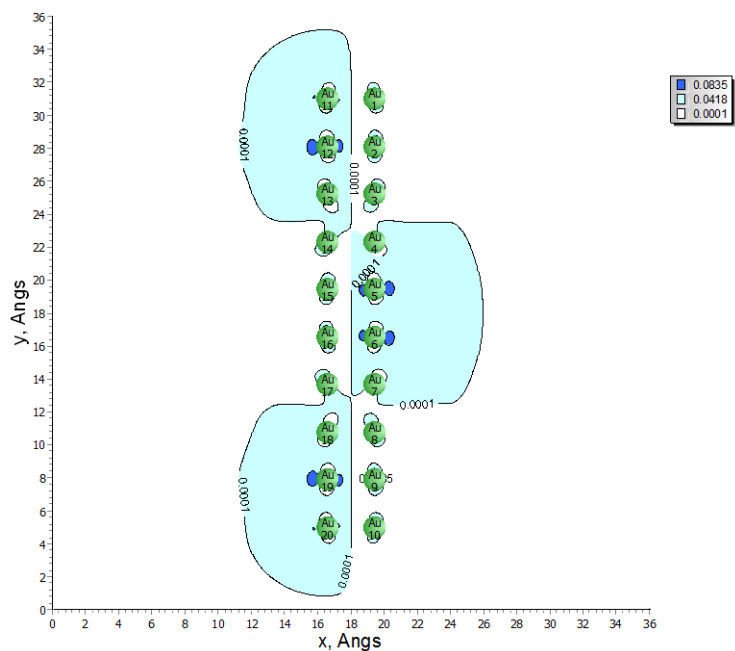


Figure 68 Highest Occupied Molecular Orbital (HOMO) of square $\text{Au}_{10}\text{Au}_{10}$ chain.

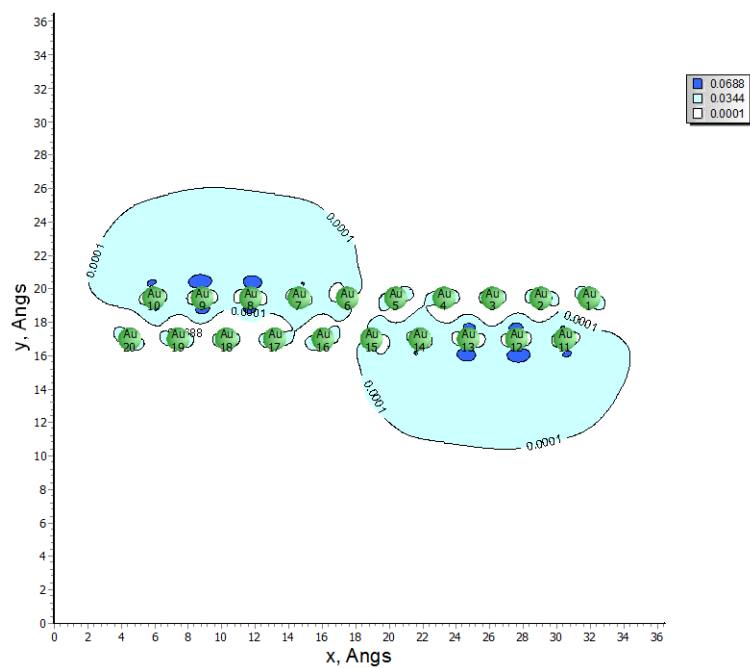


Figure 69 Highest Occupied Molecular Orbital (HOMO) of zig-zag $\text{Au}_{10}\text{Au}_{10}$ chain

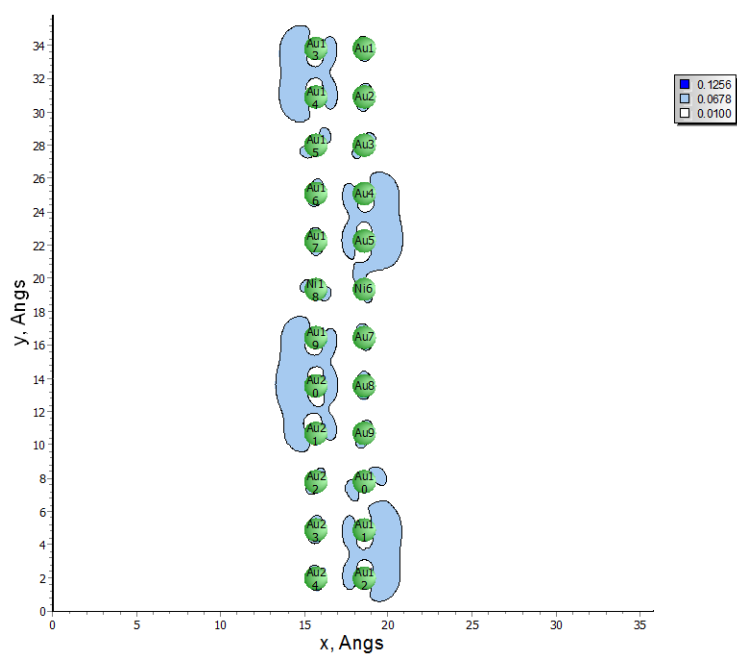
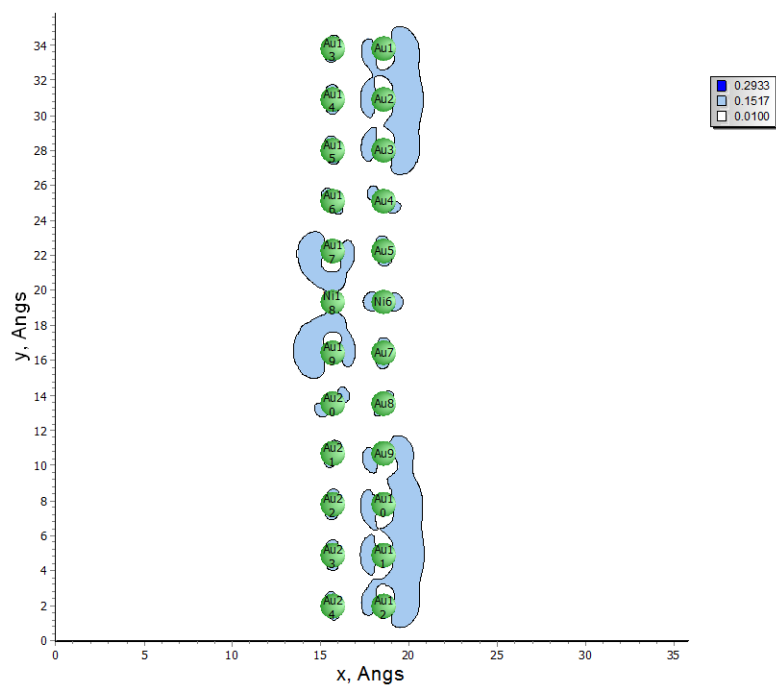


Figure 70 (a)HOMO and (b) LUMO of $\text{Au}_{26}\text{Ni}_2$ chains with 2 Ni atoms in the middle of each 14 atom chain.

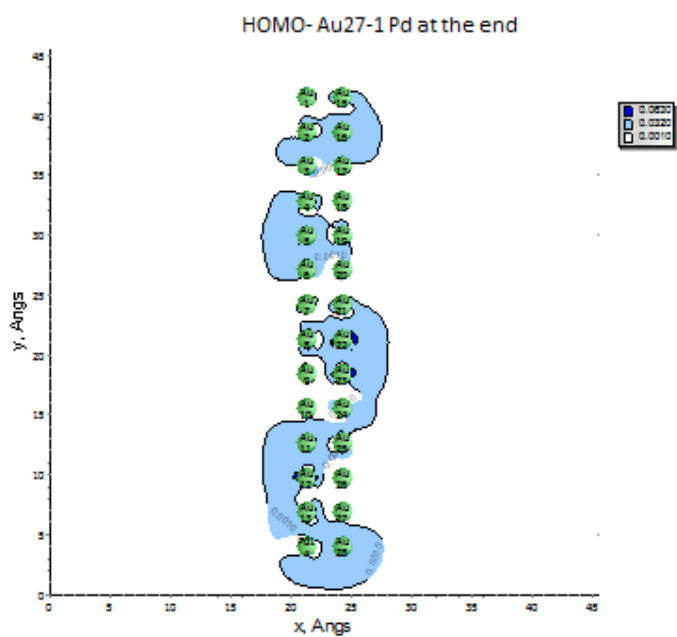
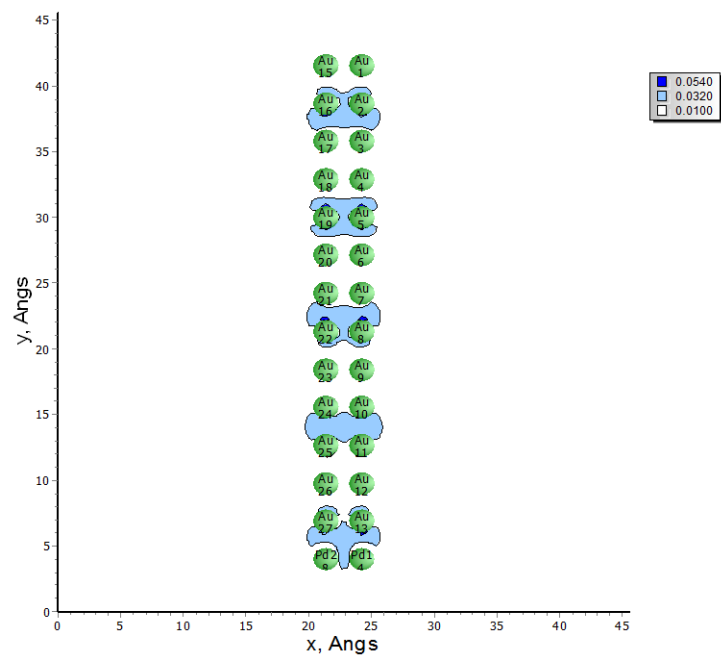


Figure 71 HOMO of (a) $\text{Au}_{26}\text{Pd}_2$ (2 Pd atoms at the end) (b) $\text{Au}_{26}\text{Pd}_1$ (1 Pd atom at the end).

The molecular orbitals for the coupled chains are shown below. Fig. 72 shows various transitions taking place in these chains. Darker lines indicate more oscillator strength.

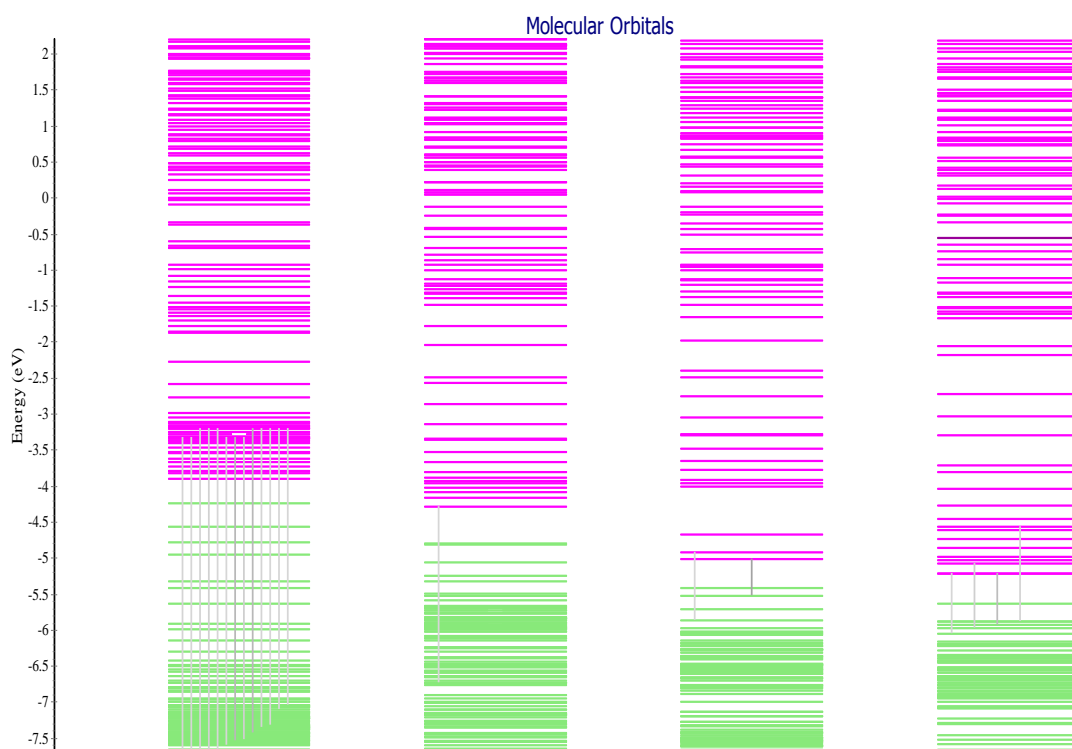


Figure 72 Molecular orbitals for the mixed chains (from left to right) Au-Fe , Au-Ni, Au-Pd, Au-Pt.

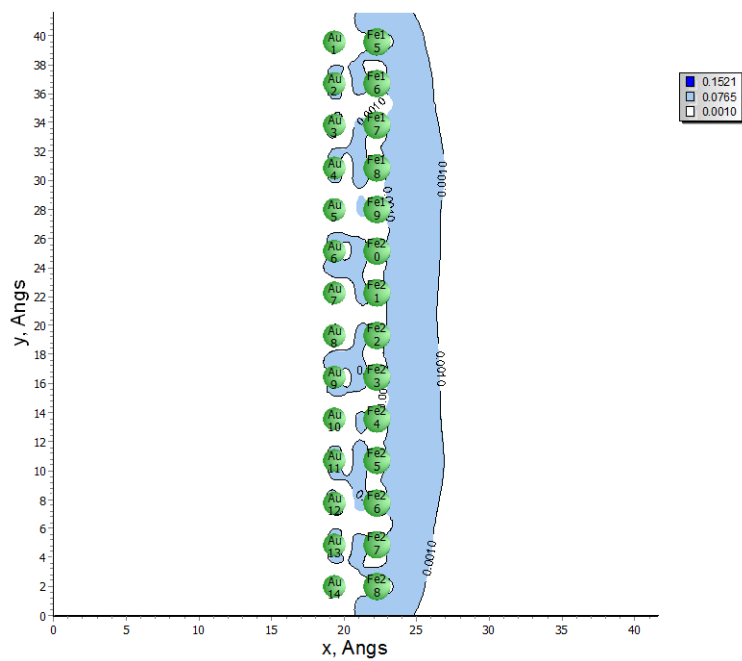
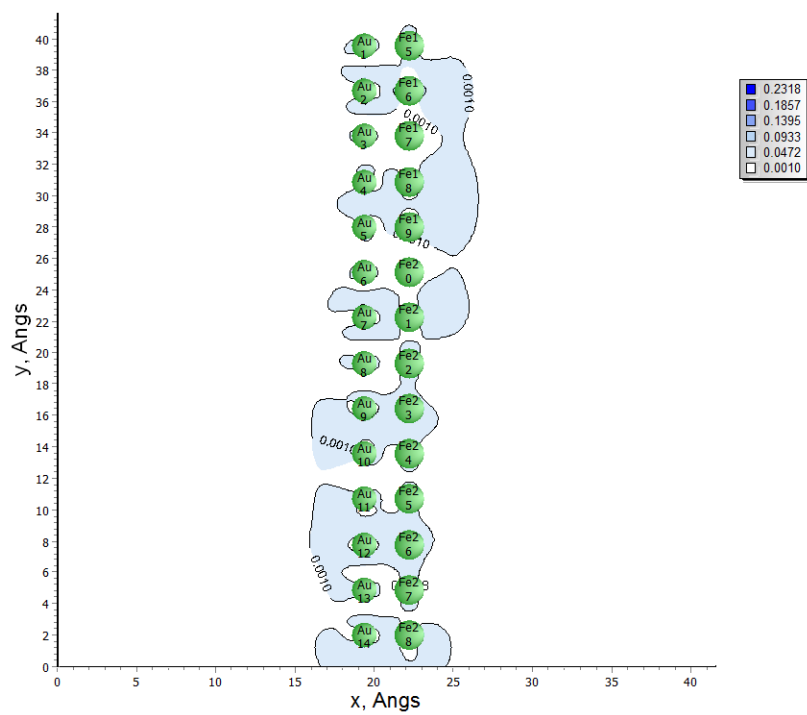


Figure 73 (a)HOMO and (b) LUMO of $\text{Au}_{14}\text{Fe}_{14}$ chains.

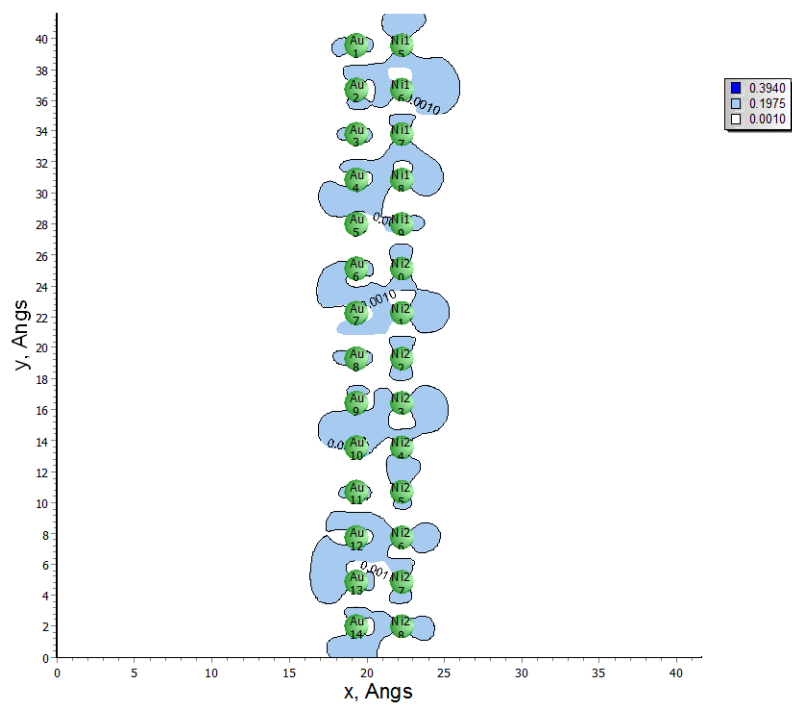
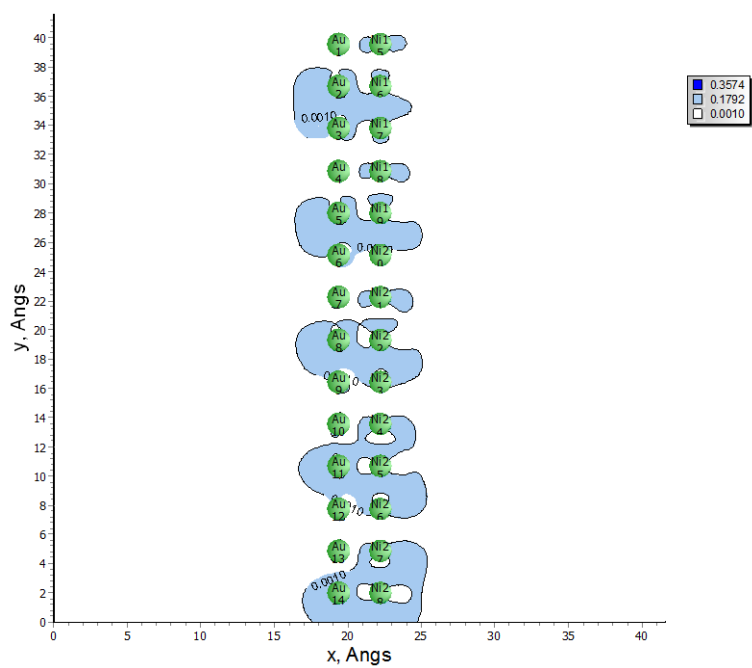


Figure 74 (a)HOMO and (b) LUMO of $\text{Au}_{14}\text{Ni}_{14}$ chains.

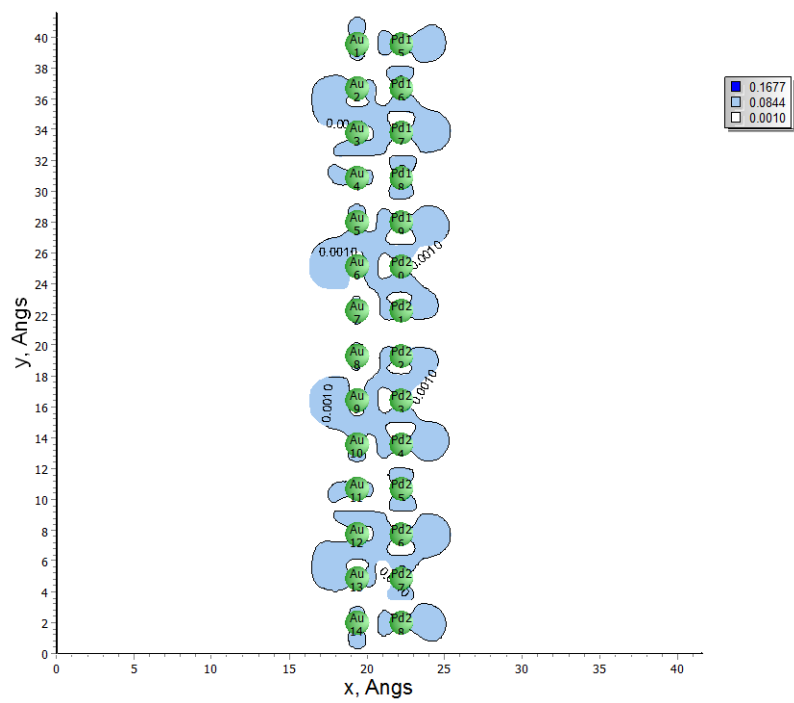
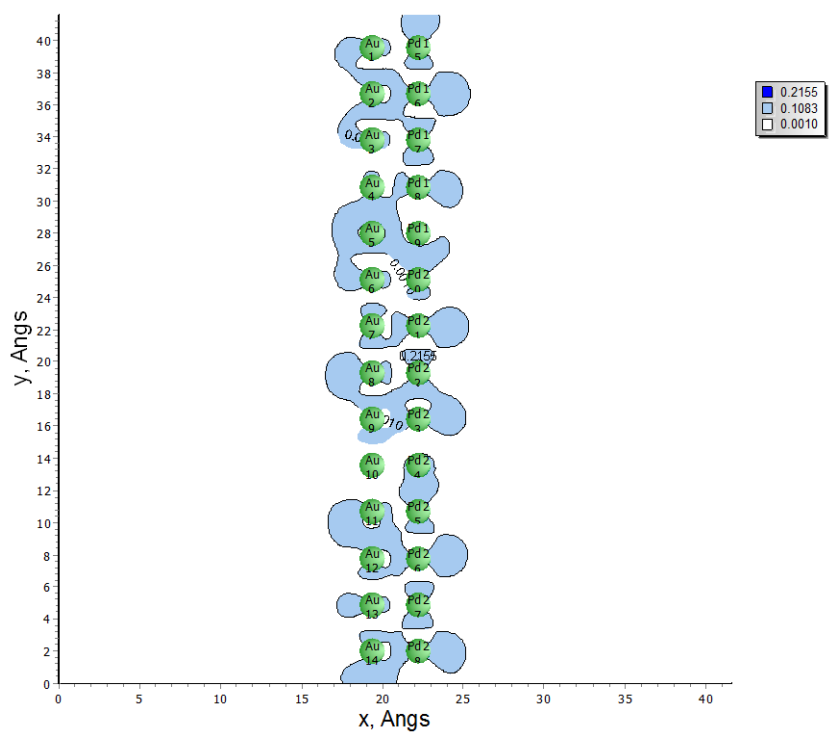


Figure 75 (a)HOMO and (b) LUMO of $\text{Au}_{14}\text{Pd}_{14}$ chains.

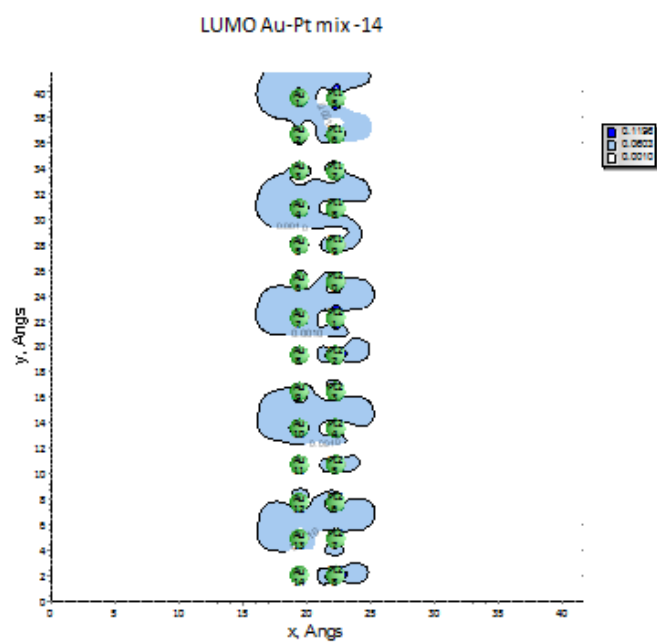
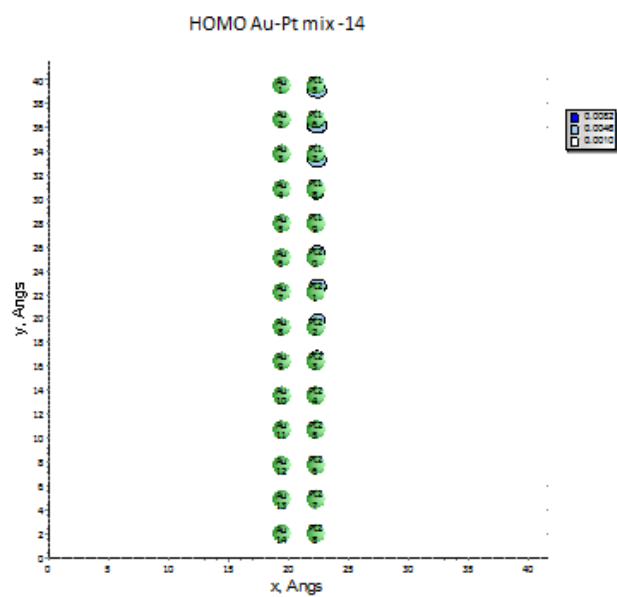


Figure 76 (a)HOMO and (b) LUMO of $\text{Au}_{14}\text{Pt}_{14}$ chains.

REFERENCES

- 1 A. T. Bell, Science **299**, 1688 (2003).
- 2 B. J. L. L.N. Ng, M.N. Zervas, J.S. Wilkinson, Optics Communications **208**, 117 (2002).
- 3 E. Ozbay, Science **311**, 189 (2006).
- 4 R. Elghanian, Science **277**, 1078 (1997).
- 5 S. E. Lee and L. P. Lee, Current opinion in biotechnology **21**, 489 (2010).
- 6 L. Xiao, B. Tollberg, X. Hu, and L. Wang, J Chem Phys **124**, 114309 (2006).
- 7 J. Z. Zhang and C. Noguez, Plasmonics **3**, 127 (2008).
- 8 N. Stokes, M. B. Cortie, T. J. Davis, and A. M. McDonagh, Plasmonics **7**, 235 (2011).
- 9 M. B. Cortie and A. M. McDonagh, Chemical reviews **111**, 3713 (2011).
- 10 A. H. a. U. Kreibig, Eur. Phys. J. AP **10**, 193 (2000).
- 11 E. Prodan and P. Nordlander, J Chem Phys **120**, 5444 (2004).
- 12 L. R. Hirsch, A. M. Gobin, A. R. Lowery, F. Tam, R. A. Drezek, N. J. Halas, and J. L. West, Annals of biomedical engineering **34**, 15 (2006).
- 13 C. O. P. Nordlander, E. Prodan, K. Li and M. I. Stockman, Nano letters **4**, 899 (2004).
- 14 Q.-H. W. K.-H. Su, and X. Zhang, J. J. Mock, D. R. Smith, and S. Schultz, Nano letters **3**, 1087 (2003).
- 15 S. Maier, P. Kik, and H. Atwater, Physical Review B **67** (2003).
- 16 J. W. H. Mark L. Brongersma, and Harry A. Atwater, PHYSICAL REVIEW B **62** (2000).
- 17 D. Solis, Jr., B. Willingham, S. L. Nauert, L. S. Slaughter, J. Olson, P. Swanglap, A. Paul, W. S. Chang, and S. Link, Nano letters **12**, 1349 (2012).
- 18 A. M. a. A. Chattopadhyay, J. Phys. Chem. C **112**, 11265 (2008).
- 19 K. Li, M. I. Stockman, and D. J. Bergman, Physical Review Letters **91** (2003).
- 20 T. M. W. N. Nilius, W. Ho, SCIENCE **297**, 1853 (2002).
- 21 K. F. M. Chun Hung Lui, Jie Shan and Tony F. Heinz, Phys. Rev. Lett. **105** (2010).
- 22 M. Fallot, Ann. Phys. (Paris) **10** (1938).
- 23 O. N. Mryasov, Phase Transitions **78**, 197 (2005).
- 24 M. C. T. Payne, M. P.; Allan, D. C.; Arias, T. A.; Joannopoulos, J. D., Reviews of Modern Physics **64**, 1045 (1992).
- 25 P. H. a. W. Kohn, Phys. Rev. **136**, 864 (1964).
- 26 W. K. a. L. J. Sham, Phys. Rev. **140**, A1133 (1965).
- 27 K. B. J. P. Perdew, and M. Ernzerhof. , Phys. Rev. Lett. **77**, 3865 (1996).
- 28 J. A. C. J.P. Perdew, S.H. Vosko, K.A. Jackson, M.R. Pederson, D.J. Singh, and C. Fiolhais, Phys. Rev. B **46**, 6671 (1992).
- 29 P. J. P., *Electronic Structure of Solids* (Berlin: Academic,, Berlin: Academic,, 1991).

30 J. P. Perdew and W. Yue, Physical Review B **33**, 8800 (1986).
 31 A. D. Becke, The Journal of Chemical Physics **98**, 5648 (1993).
 32 L. W. S. H. Vosko, and M. Nusair, Can. J. Phys. **58**, 1200 (1980).
 33 W. Y. C. Lee, and R. G. Parr, Phys. Rev. B **7**, 785 (1988).
 34 A. K. Volodymyr Turkowski, Neha Nayyar and Talat S. Rahman, J. Chem. Phys.
136 (2012).
 35 A. K. Volodymyr Turkowski, Neha Nayyar and Talat S Rahman, J. Phys.:
 Condens. Matter **22** (2010).
 36 W. M. a. D. Vollhardt, Phys. Rev. Lett. **62**, 1066 (1989).
 37 E. R. a. E. K. U. Gross, Phys. Rev. Lett. **52**, 997 (1984).
 38 M. E. Casida, *"Time-Dependent Density Functional Response Theory of
 Molecular Systems:Theory, Computational Methods, and Functionals"* (Elsevier,
 Amsterdam, 1996).
 39 G.Mie, Annalen der Physik **25**, 377 (1908).
 40 K. A. S. Kummel, P.-G. Reinhard, Applied Physics B: Lasers and Optics **73**, 293
 (2001).
 41 x000Fc, S. mmel, K. Andrae, and P. G. Reinhard, Applied Physics B: Lasers and
 Optics **73**, 293 (2001).
 42 J. Yan, Z. Yuan, and S. Gao, Physical Review Letters **98** (2007).
 43 F. E. Stephan Bernadotte, and Christoph R. Jacob, J. Phys. Chem. C **117**, 1863
 (2013).
 44 J. Yan and S. Gao, Physical Review B **78** (2008).
 45 E. B. G. a. C. M. Aikens, Nanoscale **4**, 4190 (2012).
 46 K. Y. Lian, P. Salek, M. Jin, and D. Ding, J Chem Phys **130**, 174701 (2009).
 47 D.-D. Liu and H. Zhang, Chinese Physics B **20**, 097105 (2011).
 48 C. A. a. N. M.B, Phys. Rev. B **72**, 045416 (2005).
 49 S. Y. Tadaaki Nagao, Takeshi Inaoka, and Toshio Sakurai, Phys. Rev. Lett. **97**
 (2006).
 50 I. Barke, F. Zheng, S. Bockenhauer, K. Sell, V. Oeynhausen, K. Meiwes-Broer,
 S. Erwin, and F. Himpsel, Physical Review B **79** (2009).
 51 J. Wang, M. Li, and E. Altman, Physical Review B **70** (2004).
 52 K.-H. S. Q.-H. Wei, S. Durant, and X. Zhang, Nano letters **4**, 1067 (2004).
 53 N. Nilius, T. M. Wallis, and W. Ho, Applied Physics A **80**, 951 (2005).
 54 F. M. J. a. T. G. W. a. S. H. B., GAUSSIAN 03, revision D.01, (Gaussian, Inc.,
 Wallingford, CT, 2004). (2003).
 55 P. J. Hay and W. R. Wadt, The Journal of Chemical Physics **82**, 299 (1985).
 56 E. C. M. Gaudry, M. Pellarin, J. Lermé, L. Arnaud, J. R. Huntzinger, J. L. Vialle,
 M. Broyer, J. L. Rousset, M. Treilleux, and P. Mélinon, Phys. Rev. B **67** (2003).
 57 Y. Y. a. H.-j. X. Reng-lai Wu, arXiv:1401.0252 [cond-mat.mes-hall].
 58 R. A. Muniz, H. P. Dahal, A. V. Balatsky, and S. Haas, Physical Review B **82**
 (2010).
 59 P. Song, P. Nordlander, and S. Gao, J Chem Phys **134**, 074701 (2011).
 60 T. Yasuike, K. Nobusada, and M. Hayashi, Physical Review A **83** (2011).

61 H.-F. Yin and H. Zhang, International Journal of Quantum Chemistry **112**, 2816
(2012).

62 H. Ma, F. Gao, and W. Liang, The Journal of Physical Chemistry C **116**, 1755
(2012).

63 H.-F. Yin and H. Zhang, Physica B: Condensed Matter **407**, 416 (2012).

64 B. J. Wang, Y. Xu, and S. H. Ke, J Chem Phys **137**, 054101 (2012).

65 N. Nayyar, V. Turkowski, and T. S. Rahman, Physical Review Letters **109** (2012).

66 J. Freericks, V. Turkowski, and V. Zlatić, Physical Review B **71** (2005).

67 A. Govorov, J. Lee, and N. Kotov, Physical Review B **76** (2007).

68 S. M. Sadeghi and R. G. West, Journal of physics. Condensed matter : an
Institute of Physics journal **23**, 425302 (2011).

69 K. H. Drexhage, North-Holland: Amsterdam, The Netherlands,, 1974).

70 P. L. Hernández-Martínez, 2010.

71 E. Cohen-Hoshen, G. W. Bryant, I. Pinkas, J. Sperling, and I. Bar-Joseph, Nano
letters **12**, 4260 (2012).

72 M. Achremann, J. Phys. Chem. lett. **1** (2010).

73 J.-Y. Yan, Physical Review B **86** (2012).

74 V. Turkowski, A. Leonardo, and C. Ullrich, Physical Review B **79** (2009).

75 S.-H. W. a. Z. W. Marc Dvorak, Phys. Rev. Lett. **110** (2013).

76 A. R. B. Radisavljevic, J. Brivio, V. Giacometti and A. Kis., Nature Nanotech. **6**
(2011).

77 A. N. D. Lembke and A. Kis, 10070 (2012), ACS Nano **6** (2012).

78 K.-Z. K. Wang QH, Kis A, Coleman JN, Strano MS., Nat Nanotechnol. **11**, 699
(2012).

79 H. S. S. Manish Chhowalla, Goki Eda, Lain-Jong Li, Kian Ping Loh and Hua
Zhang, Nature Chemistry **5**, 263 (2013).

80 H. S. M. Lee, S. W.; Chang, Y. G.; Park, M. K.; Nam, T.; Kim, H.; Kim, J. H.; Ryu,
S.; Im, S., Nano letters **12**, 3695 (2012).

81 X. Q. Ji Feng, Cheng-Wei Huang and Ju Li, Nature Photonics **6**, 865 (2012).

82 C. L. Kin Fai Mak, James Hone, Jie Shan, and Tony F. Heinz, Phys. Rev. Lett.
105 (2010).

83 L. S. Andrea Splendiani, Yuanbo Zhang, Tianshu Li, Jonghwan Kim, Chi-Yung
Chim, Giulia Galli, and Feng Wang, Nano Lett. **10**, 1271 (2010).

84 O. O. Nils Scheuschner, Anne-Marie Kaulitz, Roland Gillen, Marika Schleberger,
and Janina Maultzsch, arXiv:1311.5824

85 K. H. Kin Fai Mak, Changgu Lee, Gwan Hyoung Lee, James Hone, Tony F.
Heinz & Jie Shan, Nature materials **12**, 207 (2013).

86 V. T. Alfredo Ramirez-Torres, and Talat S. Rahman, arxiv:1402.4041.

87 P. G. e. al., J. Phys.: Condens. Matter **21** (2009).

88 A. C. F. G. Savini, F. Giustino Phys. Rev. lett. **105** (2010).

89 R. S. Th. Böker, A. Müller, C. Janowitz, R. Manzke, D. Voß, P. Krüger, A. Mazur,
and J. Pollmann, phys. Rev. B **64** (2001).

90 H. G. S. N. Wakabayashi, and R. M. Nicklow, Phys. Rev. B **12** (1975).

91 S. T. J. Kang, J. Zhou, J.B. Li, and J.Q. Wu, Applied Physics Letters **102** (2013).
 92 F. H. d. J. D.Y. Qiu, and S.G. Louie, Phys. Rev. Lett. **111** (2013).
 93 A. J. C. Zhang, C.-L. Hsu, L.-J. Li, and C.-K. Shih, arXiv preprint arXiv:1401.5100
 (2014).
 94 J. P. C. Zhou Li Physica B: Condensed Matter **421**, 97 (2013).
 95 P. B. Allen, Phys. Rev. Lett. **59** (1987).
 96 V. Moruzzi and P. Marcus, Physical Review B **46**, 2864 (1992).
 97 M. Gruner, E. Hoffmann, and P. Entel, Physical Review B **67** (2003).
 98 R. Gu and V. Antropov, Physical Review B **72** (2005).
 99 Y. M. Kazuki Ohtake , Kohki Takahashi , Reisho Onodera , Shojiro Kimura
 ,Kazuo Watanabe , and Keiichi Koyama, IEEE TRANSACTIONS ON
 MAGNETICS **50**, 1001404 (2014).
 100 A. J. H. P. Tu, J. S. Kouvel and J. B. Comly, J. Appl. Phys. **40** (1969).
 101 L. M. S. a. P. Mavropoulos, Phys. Rev. B **83** (2011).
 102 F. H. David W. Cooke, C. Baldasseroni, C. Bordel, S. Moyerman and E. E.
 Fullerton, Phys. Rev. Lett. **109** (2012).
 103 J. H. Ganping Ju, Bastiaan Bergman, Rene´ J.M. van deVeerdonk, Oleg N.
 Mryasov, Jai-Young Kim, and D. W. Xiaowei Wu, and Bert Koopmans, Phys.
 Rev. Lett. **93** (2004).
 104 H. Y. Y. Ko, T. Suzuki, N. T. Nam, N. N. Phuoc, J. Cao, and Y. Hirotsu, Journal
 of Magnetism and Magnetic Materials **320**, 3120 (2008).
 105 H. Y. Y. Ko, T. Suzuki, N. N. Phuoc, and J. Cao, Journal of Applied Physics **103**,
 07D508 (2008).
 106 Z. Jia, J. W. Harrell, and R. D. K. Misra, Applied Physics Letters **93**, 022504
 (2008).
 107 A. Hillion, et al., Physical Review Letters **110** (2013).